Chapter 4
Scattering from Surfaces and Thin Films

As in many branches of modern physics, scattering experiments are an important source of information in surface and thin film research. The scattering process on a surface is therefore a central topic among the various interactions of a solid. Like in bulk solid-state physics, elastic scattering can tell us something about the symmetry and the geometric arrangement of atoms near the surface, whereas inelastic scattering processes, where energy quanta are transferred to or from the topmost atomic layers of a solid, yield information about possible excitations of a surface or interface, both electronic and vibronic ones. In principle, all kinds of particles, X-rays, electrons, atoms, molecules, ions, neutrons, etc. can be used as probes. The only prerequisite in surface and interface physics is the required surface sensitivity. The geometry and possible excitations of about 10^{15} surface atoms per cm^2 must be studied against the background of about 10^{23} atoms present in a bulk volume of one cm^3. In surface and interface physics the appropriate geometry for a scattering experiment is thus the reflection geometry. Furthermore, only particles that do not penetrate too deeply into the solid can be used. Neutron scattering, although it is applied in some studies, is not a very convenient technique because of the "weak" interaction with solid material. The same is true to some extent for X-ray scattering. X-rays generally penetrate the whole crystal and the information carried by them about surface atoms is negligible. If used in surface analysis, X-ray scattering requires a special geometry and experimental arrangement. In this sense ideal probes for the surface are atoms, ions, molecules and low-energy electrons [4.1]. Atoms and molecules with low energy interact only with the outermost atoms of a solid, and low-energy electrons generally penetrate only a few Ångstroms into the material. The mean-free path in the solid is, of course, dependent on the energy of the electrons, as may be inferred from Fig. 4.1. In particular, for low-energy electrons, the "strong" interaction with matter – i.e. with the valence electrons of the solid – leads to considerable problems in the theoretical description; in contrast to X-ray and neutron scattering multiple-scattering events must be taken into account, and thus the simple analogy to an optical diffraction experiment breaks down. In quantum-mechanical language, the Born approximation is not sufficient. A detailed treatment using the so-called *dynamic theory* (Sect. 4.4) takes into account all these effects by considering the boundary problem of matching all possible electron waves outside and inside the solid in the correct way.

H. Lüth, *Solid Surfaces, Interfaces and Thin Films*, 5th ed., Graduate Texts in Physics,
DOI 10.1007/978-3-642-13592-7_4,

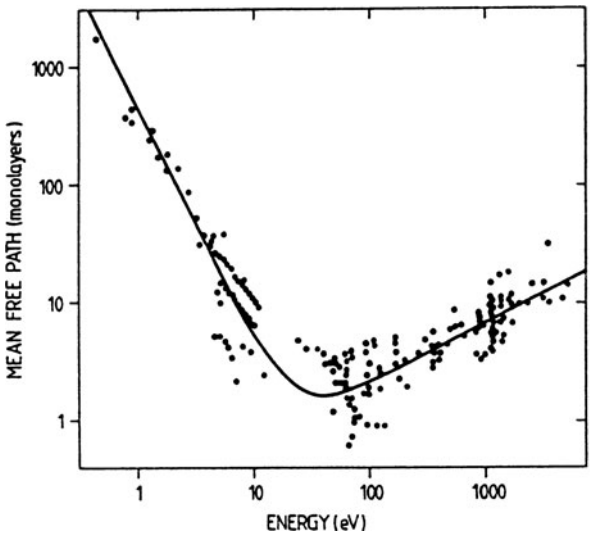

Fig. 4.1 Mean free path of electrons in solids as a function of their energy; a compilation of a variety of experimental data [4.2]. The quasi-universal dependence for a large number of different materials is due to the fact that the major interaction mechanism between the electrons and the solid is the excitation of plasmon waves whose energy is determined by the electron density in the solid

Nevertheless, a simple treatment of the surface scattering process within the framework of single-scattering events, i.e. along the lines of the Born approximation, yields insights into the important features of scattering at surfaces. This approach is called the *kinematic theory*; it is applicable to all kinds of particle-surface scattering, elastic and inelastic, but cannot describe the details of the intensity distribution in low-energy electron scattering.

4.1 Kinematic Theory of Surface Scattering

We shall refer in the following to electron scattering, although other kinds of wave-like projectiles such as atoms, molecules, etc. can also be described in the same manner. The interaction of the particle with the solid – in particular with its surface – is described by a potential

$$V(\boldsymbol{r}, t) = \sum_{\boldsymbol{n}} v[\boldsymbol{r} - \boldsymbol{\rho}_{\boldsymbol{n}}(t)], \tag{4.1}$$

where $\boldsymbol{n}$ (= triple m, n, p) labels the atoms in a primitive lattice, and v is the interaction potential with a single near-surface atom (substrate or adsorbate) at the instantaneous position $\boldsymbol{\rho}_{\boldsymbol{n}}(t) \cdot \boldsymbol{\rho}_{\boldsymbol{n}}(t)$ contains the time-independent equilibrium position $\boldsymbol{r}_{\boldsymbol{n}}$ and the displacement $\boldsymbol{s}_{\boldsymbol{n}}(t)$ from equilibrium: $\boldsymbol{\rho}_{\boldsymbol{n}}(t) = \boldsymbol{r}_{\boldsymbol{n}} + \boldsymbol{s}_{\boldsymbol{n}}(t)$. Monoenergetic particles with energy E are incident with a wave vector $\boldsymbol{k}(E = \hbar^2 k^2/2m)$

and are scattered into a state $\boldsymbol{k}'$. According to time-dependent quantum-mechanical perturbation theory, the scattering probability per unit time from $\boldsymbol{k}$ into $\boldsymbol{k}'$ is

$$W_{\boldsymbol{k}\boldsymbol{k}'} = \lim_{\tau\to\infty} \frac{1}{\tau} |c_{\boldsymbol{k}\boldsymbol{k}'}(\tau)|^2 \tag{4.2}$$

with the transition amplitude

$$c_{\boldsymbol{k}\boldsymbol{k}'}(\tau) = \frac{-\mathrm{i}}{\hbar} \int \mathrm{d}\boldsymbol{r} \int_0^\tau \mathrm{d}t \psi_\mathrm{s}^*(\boldsymbol{r}, t) V(\boldsymbol{r}) \psi_\mathrm{i}(\boldsymbol{r}, t). \tag{4.3}$$

For the incident and the scattered waves, ψ_i and ψ_s, we assume a plane wave character, i.e.,

$$\psi_\mathrm{i}(\boldsymbol{r}, t) = V^{-1/2} \mathrm{e}^{\mathrm{i}(\boldsymbol{k}\cdot\boldsymbol{r} - Et/\hbar)}, \tag{4.4a}$$

$$\psi_\mathrm{s}(\boldsymbol{r}, t) = V^{-1/2} \mathrm{e}^{\mathrm{i}(\boldsymbol{k}'\cdot\boldsymbol{r} - E't/\hbar)}. \tag{4.4b}$$

The probability amplitude for scattering within a time τ is therefore

$$c_{\boldsymbol{k}\boldsymbol{k}'}(\tau) = \frac{-\mathrm{i}}{\hbar} \sum_{\boldsymbol{n}} \int_0^\tau \mathrm{e}^{\mathrm{i}(E'-E)t/\hbar} \int \mathrm{e}^{\mathrm{i}(\boldsymbol{k}-\boldsymbol{k}')\cdot\boldsymbol{r}} v[\boldsymbol{r} - \boldsymbol{\rho}_{\boldsymbol{n}}(t)] \mathrm{d}\boldsymbol{r} \mathrm{d}t. \tag{4.5}$$

The vector $\boldsymbol{r} - \boldsymbol{\rho}_{\boldsymbol{n}}(t) = \boldsymbol{\xi}$ describes a position of a moving atom, whose nucleus is at the instantaneous position $\boldsymbol{\rho}_{\boldsymbol{n}}(t)$, i.e., with $\mathrm{d}\boldsymbol{r} = \mathrm{d}\boldsymbol{\xi}$,

$$c_{\boldsymbol{k}\boldsymbol{k}'}(\tau) = \frac{-\mathrm{i}}{\hbar} \sum_{\boldsymbol{n}} \int_0^\tau \mathrm{d}t\, \mathrm{e}^{\mathrm{i}(E'-E)t/\hbar} \mathrm{e}^{\mathrm{i}(\boldsymbol{k}-\boldsymbol{k}')\cdot\boldsymbol{\rho}_{\boldsymbol{n}}(t)} \int \mathrm{d}\boldsymbol{\xi}\, v(\boldsymbol{\xi}) \mathrm{e}^{-\mathrm{i}(\boldsymbol{k}-\boldsymbol{k}')\cdot\boldsymbol{\xi}}. \tag{4.6}$$

The last time-independent term is an atomic scattering factor. It describes the detailed scattering mechanism at the single atom. With the scattering vector

$$\boldsymbol{K} = \boldsymbol{k}' - \boldsymbol{k} \tag{4.7}$$

it becomes

$$f(\boldsymbol{K}) = \int \mathrm{d}\boldsymbol{\xi}\, v(\boldsymbol{\xi}) \mathrm{e}^{-\mathrm{i}\boldsymbol{K}\cdot\boldsymbol{\xi}}. \tag{4.8}$$

The instantaneous position of an atom near the surface can be described as

$$\boldsymbol{\rho}_{\boldsymbol{n}}(t) = \boldsymbol{r}_{\boldsymbol{n}} + \boldsymbol{s}_{\boldsymbol{n}}(t) = \boldsymbol{r}_{\boldsymbol{n}\parallel} + z_p \hat{\boldsymbol{e}}_\perp + \boldsymbol{s}_{\boldsymbol{n}}(t). \tag{4.9a}$$

The splitting into two components parallel ($\parallel$) and perpendicular ($\perp$) to the surface [$\boldsymbol{n} = (\boldsymbol{n}\parallel, p)$], with $\boldsymbol{n}\parallel$ as a vector parallel to the surface, is convenient because of

the translational symmetry parallel to the surface which allows a Fourier representation:

$$\boldsymbol{\rho}_{\boldsymbol{n}}(t) = \boldsymbol{r}_{\boldsymbol{n}\parallel} + z_p\hat{\boldsymbol{e}}_\perp + \sum_{\boldsymbol{q}_\parallel} \hat{\boldsymbol{s}}(\boldsymbol{q}_\parallel, z_p) \exp\left[\pm \mathrm{i}\boldsymbol{q}_\parallel \cdot \boldsymbol{r}_{\boldsymbol{n}\parallel} \pm \mathrm{i}\omega(\boldsymbol{q}_\parallel)t\right]. \tag{4.9b}$$

In this representation the displacement from equilibrium $\boldsymbol{s}_{\boldsymbol{n}}(t)$ is described by a harmonic wave with frequency $\omega(\boldsymbol{q}_\parallel)$ and wave vector $\boldsymbol{q}_\parallel$ parallel to the surface. The most general excitation would be a superposition of modes with different $\omega(\boldsymbol{q}_\parallel)$ From (4.6) it follows that

$$c_{\boldsymbol{k}\boldsymbol{k}'}(\tau) = \frac{-\mathrm{i}}{\hbar} f(\boldsymbol{K}) \sum_{\boldsymbol{n}_\parallel, p} \int_0^\tau \mathrm{d}t\, \mathrm{e}^{\mathrm{i}(E'-E)t/\hbar} \times \exp\left\{-\mathrm{i}\boldsymbol{K} \cdot \left[\boldsymbol{r}_{\boldsymbol{n}\parallel} + z_p\hat{\boldsymbol{e}}_\perp + \sum_{\boldsymbol{q}_\parallel} \hat{\boldsymbol{s}}(\boldsymbol{q}_\parallel, z_p) \exp(\pm \mathrm{i}\boldsymbol{q}_\parallel \cdot \boldsymbol{r}_{\boldsymbol{n}\parallel} \pm \mathrm{i}\omega(\boldsymbol{q}_\parallel)t)\right]\right\}. \tag{4.10}$$

Because the displacements from equilibrium are small, the exponential function can be expanded:

$$\exp\left\{-\mathrm{i}\boldsymbol{K} \cdot \left[\sum_{\boldsymbol{q}_\parallel} \hat{\boldsymbol{s}}(\boldsymbol{q}_\parallel, z_p)\mathrm{e}^{\pm \mathrm{i}\cdots}\right]\right\} \simeq 1 - \mathrm{i}\boldsymbol{K} \cdot \left[\sum_{\boldsymbol{q}_\parallel} \hat{\boldsymbol{s}}(\boldsymbol{q}_\parallel, z_p) \exp[\pm \mathrm{i}(\boldsymbol{q}_\parallel \cdot \boldsymbol{r}_{\boldsymbol{n}\parallel} + \omega t)]\right] + \ldots . \tag{4.11}$$

Taking into account only the first two terms in the expansion, one arrives via (4.10) at a sum of two different (elastic and inelastic) contributions to the probability amplitude:

$$c_{\boldsymbol{k}\boldsymbol{k}'}(\tau) = \frac{-\mathrm{i}}{\hbar} f(\boldsymbol{K}) \sum_{\boldsymbol{n}_\parallel, p} \int_0^\tau \mathrm{d}t \exp[\mathrm{i}(E' - E)t/\hbar] \exp[-\mathrm{i}\boldsymbol{K} \cdot (\boldsymbol{r}_{\boldsymbol{n}\parallel} + z_p\hat{\boldsymbol{e}}_\perp)] \times \left\{1 - \mathrm{i}\sum_{\boldsymbol{q}_\parallel} \boldsymbol{K} \cdot \hat{\boldsymbol{s}}(\boldsymbol{q}_\parallel, z_p) \exp[\pm \mathrm{i}(\boldsymbol{q}_\parallel \cdot \boldsymbol{r}_{\boldsymbol{n}\parallel} \pm \omega t)]\right\}. \tag{4.12}$$

The first "elastic" term does not contain the vibrational amplitudes $\hat{\boldsymbol{s}}$. In the calculation of the elastic scattering probability $W_{\boldsymbol{k}\boldsymbol{k}'}$ according to (4.2), the time limit $\tau \to \infty$ yields a delta function $\delta(E' - E)$; the summation over the two-dimensional

(2D) set $\boldsymbol{n}_\parallel = (m, n)$ runs over the whole surface to infinity; it contains terms of the form

$$\sum_{m,n} \mathrm{e}^{-\mathrm{i}\boldsymbol{K}\cdot(m\boldsymbol{a}+n\boldsymbol{b})} = \sum_{m,n} \left(\mathrm{e}^{-\mathrm{i}\boldsymbol{K}\cdot\boldsymbol{a}}\right)^m \left(\mathrm{e}^{-\mathrm{i}\boldsymbol{K}\cdot\boldsymbol{b}}\right)^n \tag{4.13}$$

where $\boldsymbol{a}$ and $\boldsymbol{b}$ are the basis vectors of the 2D unit mesh within the surface. As in the case of a three-dimensional (3D) lattice sum, an evaluation via a geometrical series gives, in the limit $m, n \to \infty$, a nonvanishing contribution only for

$$\boldsymbol{K}\cdot\boldsymbol{a} = 2\pi h, \quad \boldsymbol{K}\cdot\boldsymbol{b} = 2\pi k; \quad h, k \text{ integer}. \tag{4.14a}$$

With $\boldsymbol{K} = \boldsymbol{K}_\parallel + K_\perp \hat{\boldsymbol{e}}_\perp$, (4.14a) is fulfilled when

$$\boldsymbol{K}_\parallel = \boldsymbol{k}'_\parallel - \boldsymbol{k}_\parallel = \boldsymbol{G}_\parallel. \tag{4.14b}$$

The conditions (4.14) are the 2D analogs of the three Laue equations for the bulk scattering of X-rays. The third Laue equation is missing, since the third summation index p in (4.12) does not run from $-\infty$ to $+\infty$ because of the boundary at the solid surface ($z = 0$).

For the *elastic scattering probability* and with N being the number of surface atoms, one finally obtains

$$W^{(\mathrm{el})}_{\boldsymbol{k}'\boldsymbol{k}} = \frac{2\pi}{\hbar} N \left| f(\boldsymbol{K}) \sum_p \exp(\mathrm{i}K_\perp z_p) \right|^2 \delta(E' - E)\delta_{\boldsymbol{K}_\parallel,\boldsymbol{G}_\parallel}, \tag{4.15}$$

where the Kronecker delta $\delta_{\boldsymbol{K}_\parallel,\boldsymbol{G}_\parallel}$ expresses the condition (4.14b). With c as the periodic repeat distance perpendicular to the surface, i.e. $z_p = pc$, a summation of p up to infinity would yield the third Laue condition. The sum over p, however, extends only over those atomic layers below the surface which lie within the finite penetration depth of the incident particles. For low-energy atom and molecular scattering, p is restricted to the topmost atomic layer; for slow electrons it might extend over a few of atomic layers, whereby the exact number depends on the primary energy. Further consequences of (4.14 and 4.15) are considered in Chap. 5.

For the second term in (4.12), the *inelastic scattering amplitude*, one obtains

$$c^{\mathrm{inel}}_{\boldsymbol{k}\boldsymbol{k}'}(\tau) = \frac{-\mathrm{i}}{\hbar} f(\boldsymbol{K}) \sum_{\boldsymbol{n}_\parallel,p} \int_0^\tau \mathrm{d}t \exp[\mathrm{i}(E' - E)t/\hbar] \exp[-\mathrm{i}\boldsymbol{K}\cdot(\boldsymbol{r}_{\boldsymbol{n}_\parallel} + z_p\hat{\boldsymbol{e}}_\perp)]$$

$$\times (-\mathrm{i}) \sum_{\boldsymbol{q}_\parallel} \boldsymbol{K}\cdot\hat{\boldsymbol{s}}(\boldsymbol{q}_\parallel, z_p) \exp[\pm\mathrm{i}(\boldsymbol{q}_\parallel\cdot\boldsymbol{r}_{\boldsymbol{n}_\parallel} + \omega t)]$$

$$= -\hbar^{-1} f(\boldsymbol{K}) \sum_{\boldsymbol{n}_\parallel, p, \boldsymbol{q}_\parallel} \boldsymbol{K} \cdot \hat{\boldsymbol{s}}(\boldsymbol{q}_\parallel, z_p) \exp\left[-\mathrm{i}(\boldsymbol{K}_\parallel \mp \boldsymbol{q}_\parallel) \cdot \boldsymbol{r}_{\boldsymbol{n}_\parallel}\right]$$

$$\times \exp(-\mathrm{i}K_\perp z_p) \int_0^\tau \exp[\mathrm{i}(E' - E \pm \hbar\omega)t/\hbar]\mathrm{d}t. \tag{4.16}$$

Similar arguments to those in (4.13–4.15) yield the *inelastic scattering probability*

$$W_{\boldsymbol{k}\boldsymbol{k}'}^{\text{inel}} = \frac{2\pi}{\hbar} N \sum_{\boldsymbol{q}_\parallel} \delta(E' - E \pm \hbar\omega(\boldsymbol{q}_\parallel)) \delta_{\boldsymbol{K}_\parallel \pm \boldsymbol{q}_\parallel, \boldsymbol{G}_\parallel}$$

$$\times \left| f(\boldsymbol{K}) \sum_p \boldsymbol{K} \cdot \hat{\boldsymbol{s}}(\boldsymbol{q}_\parallel, z_p) \exp(-\mathrm{i}K_\perp z_p) \right|^2 \tag{4.17}$$

where N is the number of surface atoms. The delta function and the Kronecker symbol ensure energy conservation

$$E' = E \mp \hbar\omega(\boldsymbol{q}_\parallel), \tag{4.18a}$$

and the conservation of the wave-vector component parallel to the surface ($\boldsymbol{K}_\parallel = \boldsymbol{k}'_\parallel - \boldsymbol{k}_\parallel$)

$$\boldsymbol{k}'_\parallel = \boldsymbol{k}_\parallel \pm \boldsymbol{q}_\parallel + \boldsymbol{G}_\parallel, \tag{4.18b}$$

i.e. in all inelastic surface scattering processes the energy lost (or gained) in scattering must be found as the quantum energy $\hbar\omega(\boldsymbol{q}_\parallel)$ of an excited surface mode (e.g., vibrational). An extension of the present formalism can be made to include electronic excitations of the surface. Equation (4.18b) is a straightforward consequence of the 2D translational symmetry within the surface. Perpendicular to the surface the translational symmetry is broken and thus only the parallel component of the particle wave vector is conserved. The change in the wave vector $\boldsymbol{k}_\parallel$, upon scattering is given (to within an undetermined 2D reciprocal lattice vector $\boldsymbol{G}_\parallel$) by the wave vector $\boldsymbol{q}_\parallel$ of the excited surface mode.

The second factor in (4.17) is also of importance since it yields a selection rule for surface scattering, which helps to identify the symmetry of an excited vibrational (or electronic) surface excitation: the inelastic scattering probability vanishes if $\boldsymbol{K}$ is perpendicular to $\hat{\boldsymbol{s}}(\boldsymbol{q}_\parallel, z_p)$. $\hat{\boldsymbol{s}}$ are the Fourier components of the atomic vibration and therefore have the direction of the atomic displacement (or the electronic dipole moment). In an inelastic-scattering experiment one sees only those excitations for which the atomic displacement has a component parallel to the scattering vector $\boldsymbol{K} = \boldsymbol{k}' - \boldsymbol{k}$. This is illustrated in Fig. 4.2 for the vibration of an adsorbed atom. For scattering in the specular direction only modes with vibrational direction normal to the surface are detectable. Vibrations parallel to the surface can only be studied if one observes scattering with off-specular geometry. In calculating $\boldsymbol{K} = \boldsymbol{k}' - \boldsymbol{k}$ one

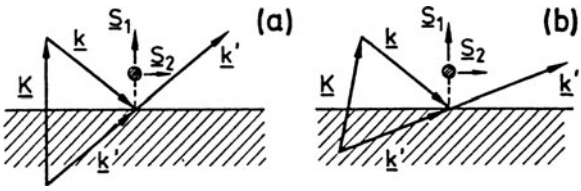

Fig. 4.2 Surface scattering on an adsorbed atom (full circle) with detection in specular (**a**) and in off-specular geometry (**b**). The energy loss $\hbar\omega$ is assumed to be small in comparison with the primary energy E, i.e. $|\boldsymbol{k}'| \simeq |\boldsymbol{k}|$. In (**a**) the scattering vector $\boldsymbol{K}$ is perpendicular to the surface, the s_2 bending vibration of the adsorbed atom is therefore not detectable, only the stretch vibration s_1 normal to the surface. In (**b**) $\boldsymbol{K}$ has components parallel and normal to the surface, thus both vibrations s_1 and s_2 can be studied

has, of course, to take into account that due to the inelastic process $|k'|$ is different from $|k|$ and that therefore, even for specular detection, there is a small component of $\boldsymbol{K}$ parallel to the surface. The size of this component depends on the ratio $\hbar\omega/E$.

4.2 The Kinematic Theory of Low-Energy Electron Diffraction

In almost every surface-physics laboratory Low-Energy Electron Diffraction (LEED) is used as the standard technique to check the crystallographic quality of a surface, prepared either as a clean surface, or in connection with ordered adsorbate overlayers [4.3]. In this experiment a beam of electrons with a primary energy between 50 and 300 eV is incident on the surface and the elastically backscattered electrons give rise to diffraction (or Bragg) spots that are imaged on a phosphorous screen (Panel VIII: Chap. 4).

To understand the essential features of such an experiment, kinematic theory is sufficient. The condition for the occurrence of an "elastic" Bragg spot is given by (4.14), i.e., the scattering vector component parallel to the surface ($\boldsymbol{K}_\parallel = \boldsymbol{k}'_\parallel - \boldsymbol{k}_\parallel$) must equal a vector of the 2D surface reciprocal lattice $\boldsymbol{G}_\parallel$. This condition is valid for the limiting case where only the topmost atomic layer is involved in scattering. For the component $\boldsymbol{K}_\perp$ perpendicular to the surface, no such condition applies. In order to extend the well-known Ewald construction to our 2D problem we must therefore relax the restriction of the third Laue equation (perpendicular to the surface). This is done by attributing to every 2D reciprocal lattice point (h, k) a rod normal to the surface (Fig. 4.3). In the 3D problem we have discrete reciprocal lattice points in the third dimension rather than rods, and these are the source of the third Laue condition for constructing the scattered beams.

In the 2D case, the possible elastically scattered beams ($\boldsymbol{k}'$) can be obtained by the following construction. According to the experimental geometry (orientation of primary beam with respect to surface) the wave vector $\boldsymbol{k}$ of the primary beam is positioned with its end at the (0, 0) reciprocal lattice point and a sphere is constructed around its starting point. As is seen from Fig. 4.3, the condition $\boldsymbol{K}_\parallel = \boldsymbol{G}_\parallel$ is fulfilled for every point at which the sphere crosses a "reciprocal-lattice rod". In

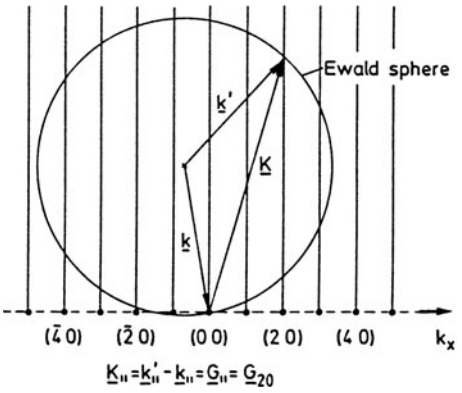

Fig. 4.3 Ewald construction for elastic scattering on a 2D surface lattice. The corresponding 2D reciprocal lattice points (hk) are plotted on a cut along k_x. The scattering condition (4.14) for the plotted beams is fulfilled for the reciprocal lattice point $(hk) = (20)$; but a number of other reflexes are also observed $(\bar{4}0)$, $(\bar{3}0)$. . .(30), $(\overline{22})$, . . .(11). . .

contrast to the 3D scattering problem in bulk solid-state physics, the occurrence of a Bragg reflection is not a singular event. No special methods like the Debye-Scherrer, or Laue techniques, etc., need to be applied to obtain a diffraction pattern. The loss of the third Laue condition in our 2D problem ensures a LEED pattern for every scattering geometry and electron energy.

These considerations are exact only in the limit of scattering from a true 2D network of atoms. In a real LEED experiment, however, the primary electrons penetrate several atomic layers into the solid. The deeper they penetrate, the more scattering events in the z-direction perpendicular to the surface contribute to the LEED pattern. In (4.15) the summation index p must run over more and more atomic layers with increasing penetration depth, and the third Laue condition becomes more and more important. This leads to a modulation of the intensities of the Bragg reflections in comparison with the case of pure 2D scattering. In the Ewald construction (Fig. 4.3) one can allow for this situation qualitatively by giving the rods periodically more or less intensity. In the extreme case of 3D scattering, where the three Laue conditions are exactly valid, the thicker regions of the rods become points of the 3D reciprocal lattice. An Ewald construction for the intermediate situation where the periodicity perpendicular to the surface enters the problem to a certain extent is shown in Fig. 4.4. When the Ewald sphere crosses a "thicker" region of the rods, the corresponding Bragg spot has strong intensity whereas less pronounced regions of the rods give rise to weaker spots. Another important consequence is the following: if we change the primary energy of the incoming electrons the magnitude of k, i.e., the radius of the Ewald sphere, changes. As k is varied, the Ewald sphere passes successively through stronger and weaker regions of the rods, and the intensity of a particular Bragg spot varies periodically. Experimentally, this provides evidence for the limited validity of the third Laue condition (perpendicular to the surface). The effect can be checked by measuring the intensity of a particular Bragg reflex (hk) in dependence on primary energy of the incident electrons. The result of this type of measurement is known in the literature as an I-V curve (I: intensity, V: accelerating voltage of the electrons).

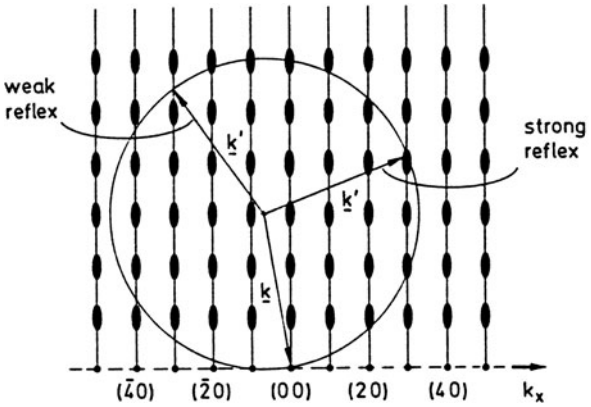

Fig. 4.4 Ewald construction for elastic scattering on a quasi-2D surface lattice, as in Fig. 4.3, but now not only scattering from the topmost lattice plane, but also from a few underlying planes, is taken into account. The "thicker" regions of the rods arise from the third Laue condition, which cannot be completely neglected. Correspondingly the (30) reflex has high intensity, whereas the $(\bar{3}0)$ spot appears weak

As is seen from Fig. 4.5, there is indeed some structure found in the I-V curves measured on Ni(100) which seems to be similar to that expected from the application of the third Laue condition [4.4]. But the maxima of the observed peaks are generally shifted to lower primary energies and there are additional structures which cannot be explained in terms of the simple picture developed so far. The shift to lower energies is easily explained by the fact that inside the crystal the electrons have a wavelength different from that in the vacuum due to the mean inner potential in the crystal. The potential difference is related to the work function of the material. The shift can therefore be used to get some information about this "inner" potential. The explanation of the additional features in the I-V curves is

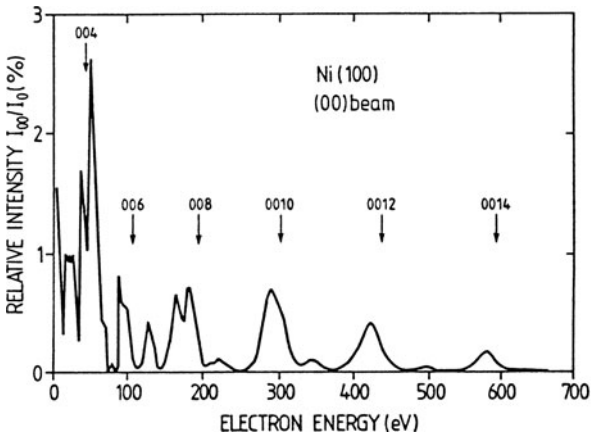

Fig. 4.5 Intensity versus voltage (I-V) curve for the (00) beam from a clean Ni(100) surface. The diffracted intensity I_{00} is referred to the intensity of the primary beam I_0 [4.4]

more involved. It requires a more thorough description of the scattering process of low-energy electrons, going beyond the approximation of kinematic theory. Due to the "strong" interaction of electrons with matter, multiple scattering processes must be taken into account. This is done in the "dynamic" theory of electron scattering to be discussed in Sect. 4.4.

4.3 What Can We Learn from Inspection of a LEED Pattern?

As is clear from the discussion in the previous section, a detailed understanding of the intensity of a LEED pattern involves the complex problem of describing multiple scattering processes within the topmost atomic layers of a crystal. The evaluation of the geometric positions of surface atoms from the LEED pattern – a so-called *structure analysis* – requires detailed interpretation of the intensities (as for X-ray scattering in bulk solid-state physics). This problem is therefore beyond the applicability of kinematic theory; it will be treated in the next section. Nonetheless, simple inspection of a LEED pattern and measurement of the geometrical spot positions can yield a great deal of useful information about a surface.

At the beginning of an experiment on a crystalline surface the first step, after looking with AES for possible contamination, consists in checking the crystallographic quality of the surface by LEED. The LEED pattern must exhibit sharp spots with high contrast and low background intensity. Random defects or crystallographic imperfections will broaden the spots and increase the background intensity due to scattering from these statistically distributed centers. One has to keep in mind, however, that the information obtained about the surface always originates from an area with a diameter smaller than the coherence width of the electron beam, i.e. for conventional LEED systems smaller than ≈ 100 Å (Panel VIII: Chap. 4).

In the simplest case, the LEED pattern of the clean surface exhibits a (1×1) structure which reflects a surface 2D symmetry equal to that of the bulk. Figure 4.6 shows the (1×1) LEED pattern obtained for a clean nonpolar ZnO$(10\bar{1}0)$ surface which was prepared in UHV by cleavage along the hexagonal *c*-axis of the wurtzite lattice. The rectangular symmetry of this particular surface is revealed and the spot separations, on conversion from reciprocal space to real space (Sect. 3.3), give the dimensions of the 2D unit mesh. It should be emphasized that the observed (1×1) pattern does not mean that the atomic geometry is equal to that of the "truncated" bulk. Atomic positions within the 2D unit mesh might be changed and also a perpendicular relaxation towards or away from the surface is possible. Essentially the same (1×1) LEED pattern as in Fig. 4.6 is also found on GaAs(110) surfaces cleaved in UHV (Sect. 3.2).

More complex LEED patterns are obtained when a reconstruction with *superstructure* is found. In Fig. 4.7 the well-known (2×1) reconstruction of Si(111) is displayed. This type of reconstruction is always found when a Si(111) or Ge(111) surface is prepared by cleavage in UHV at room temperature. The (111) lattice plane of these diamond-type elemental semiconductors has a sixfold symmetry which

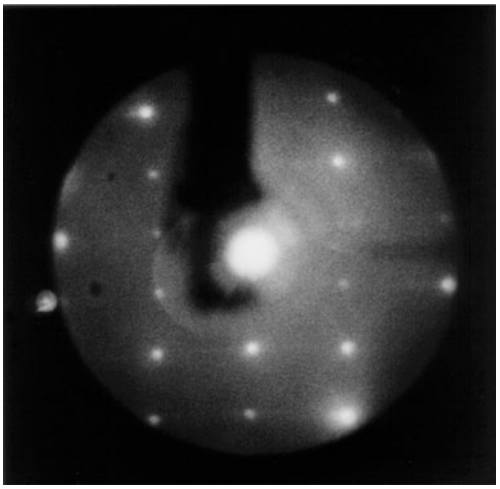

Fig. 4.6 LEED pattern of a clean cleaved nonpolar ZnO($10\bar{1}0$) surface. Primary voltage $U_0 = 140\,\mathrm{V}$

would also be found in the LEED pattern if the surface were to have the same symmetry as the truncated bulk. The LEED spots in Fig. 4.7c, however, indicate that in one direction the periodicity in real space has doubled (Fig. 4.7a). This causes half-order spots between the main Bragg spots thus giving a rectangular surface lattice in reciprocal space (LEED pattern) (Fig. 4.7b). A further complication arises since there are three possible orientations of the (2×1) unit mesh. During cleavage the double periodicity can show up in three symmetrically equivalent directions and all three may exist in different domains. If several of these domains are hit by the primary beam, the LEED pattern will consist of a superposition of patterns rotated against each other. This situation is shown in the LEED pattern of Fig. 4.7d. The nature of the (2×1) reconstruction, i.e. the detailed atomic positions on this surface, is discussed in Sect. 3.2.

Superstructures with non-integer Bragg spots can also arise from adsorbed atoms or molecules that are positioned at certain symmetry sites of the substrate surface. In Fig. 4.8 such an adsorbate superstructure is shown for the example of chemisorbed oxygen atoms on Cu(110) [4.5]. At low coverage atomic O causes half-order LEED spots in one direction of the rectangular network of (110) substrate spots. The adsorbed O atoms therefore occupy sites that are separated by twice the period of the Cu surface. Information from other experimental techniques is necessary to determine the exact adsorption sites. Care must be taken in attributing a superstructure that appears after adsorption to the adsorbate itself. An adsorbate-induced reconstruction of the substrate surface can also occur.

In some cases, the geometry of a LEED pattern can also give information about crystallographic defects on a surface. The simplest situation is a regular array of *atomic steps* on the surface. Cleaved semiconductor surfaces and poorly oriented metal surfaces often show such step arrays. Their presence can be deduced from splitting of the LEED spots. A regular step array with a definite step height d and a constant number N of atoms on the terraces between the steps means for the

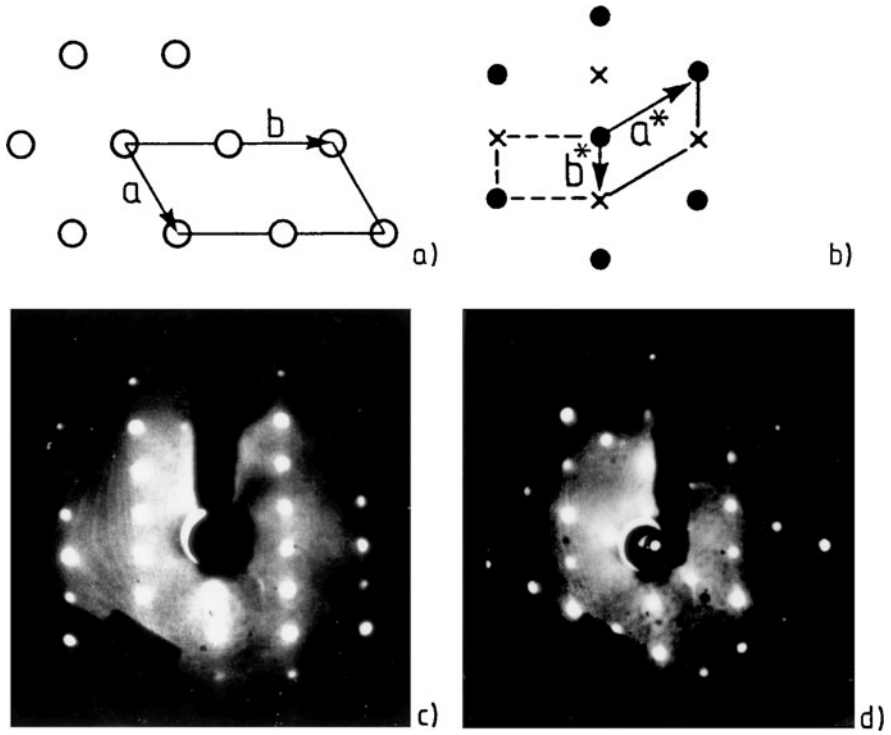

Fig. 4.7a–d (2×1) LEED pattern of a clean cleaved Si(111) surface. (**a**) (2×1) unit mesh in real space; lattice points are indicated by circles. (**b**) reciprocal lattice points of the LEED pattern; the (2×1) half-order spots are indicated by crosses. (**c**) LEED pattern measured with a primary energy $E_0 = 80\,\text{eV}$ (single domain). (**d**) LEED pattern showing the superposition of two domains rotated by 60° to one another

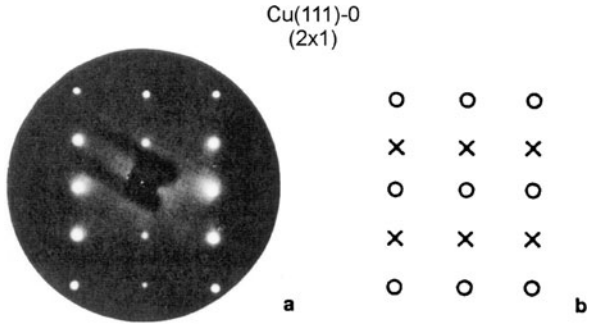

Fig. 4.8 a,b LEED pattern obtained after adsorption of atomic oxygen at low coverage on Cu(110). (**a**) (2×1) superstructure as seen on the phosphorus screen. (**b**) schematic of the (2×1) pattern with substrate spots as circles and half order spots as crosses [4.5]

surface symmetry that the lattice periodicity (lattice constant a) is superimposed on a second periodicity with repeat distance Na (Fig. 4.9). In the Ewald construction (Fig. 4.4a) second reciprocal lattice with rod spacing $Q = 2\pi/\mathrm{Na}$ has to be taken into account along with that of the surface (reciprocal lattice vector $\boldsymbol{G}_{\parallel}$). The two arrays of rods are inclined with respect to one another by the angle α between the stepped surface and the exposed lattice plane (Fig. 4.9). According to the general principle of the Ewald construction, Bragg spots appear whenever the reciprocal lattice rods intersect the Ewald sphere. In the present case of two superimposed rod arrays this condition must be fulfilled by both rod systems simultaneously. Two situations can be distinguished. The primary wave vector $\boldsymbol{k}$ has a length such that the scattered wave vector $\boldsymbol{k}'(|k'| = |k|)$ reaches a point A, where the two rod systems intersect one another on the surface of the Ewald sphere (not shown in Fig. 4.9). Then one single Bragg spot is observed in the LEED pattern. A second situation can occur for a larger primary wavevector $\boldsymbol{k}$ (this Ewald sphere is shown in Fig. 4.9) where the Ewald sphere crosses a rod of the normal reciprocal lattice (point B) but the rods of the step periodicity exhibit crossing points that do not quite coincide with this. Because of the finite number of atoms on the terraces the LEED spots are not ideally sharp and this configuration leads to two separate intensity maxima; the LEED spot is split into two components with an angular separation $\delta\varphi$.

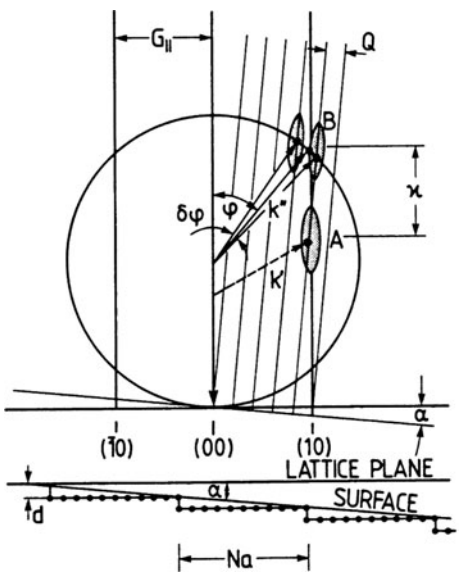

Fig. 4.9 Ewald construction for a surface with a regular step array. The steps with a height d and a terrace width aN (a is the lattice constant) cause an inclination angle α between the macroscopic surface and the main lattice plane. Corresponding to the lattice distance a, the reciprocal lattice vector is $\boldsymbol{G}_{\parallel}$. The step array is described by a superimposed inclined reciprocal lattice of periodicity $Q = 2\pi/Na$. The primary electrons are described by the wavevector $\boldsymbol{k}$ (two different primary energies with two different lengths of $\boldsymbol{k}$ are considered) and two different scattered beams ($\boldsymbol{k}'$ and $\boldsymbol{k}''$) are plotted ($k = k'$ and $k = k''$)

This angle can be directly measured on the phosphorus screen and from Fig. 4.9 it follows that

$$\delta\varphi = \frac{Q}{k'' \cos\varphi} = \frac{Q}{k \cos\varphi} = \frac{\lambda}{Na \cos\varphi}. \tag{4.19}$$

The step width Na can thus be determined by finding a primary voltage (corresponding electron wavelength λ) at which a particular LEED spot at a scattering angle φ is split into two components. The angular splitting $\delta\varphi$ then determines Na according to (4.19).

According to Fig. 4.9, the step height d can be determined from the two primary energies E' and E'' at which the same LEED beam occurs as a single (point A) and as a double spot (point B), respectively. Or, equivalently, one can change the primary energy E stepwise and look for two subsequent positions at which the same spot $\boldsymbol{G}_\parallel = \boldsymbol{G}_{hk}$ occurs as a single or as a double spot. For such two subsequent energies Fig. 4.9 yields

$$2\nu\kappa = \sqrt{|\boldsymbol{k}|^2} + k''_\perp, \quad \text{with} \quad \nu = 1, 2, 3, \ldots, \tag{4.20a}$$

$$2\nu\kappa = \sqrt{\frac{2mE}{\hbar^2}} + \sqrt{\frac{2mE}{\hbar^2} - |\boldsymbol{G}_\parallel|^2} \tag{4.20b}$$

where $k''_\perp$ is the normal component of the scattered wave vector $\boldsymbol{k}''$. The inclination angle α can be expressed in real space:

$$\frac{Q}{2\kappa} = \frac{2\pi}{2\kappa Na} = \sin\alpha \simeq \tan\alpha = \frac{d}{Na}, \tag{4.21}$$

$$2\kappa = 2\pi/d. \tag{4.22}$$

With (4.20b) one obtains

$$\nu\frac{2\pi}{d} = \sqrt{\frac{2mE}{\hbar^2}} + \sqrt{\frac{2mE}{\hbar^2} - |\boldsymbol{G}_\parallel|^2}, \quad \text{with} \quad \nu = 1, 2, 3, \ldots . \tag{4.23}$$

From two different primary-energy readings E_ν at which double or single spots are observed (4.23) allows the determination of the step height d. For the (00) LEED spot with $\boldsymbol{G}_\parallel = \boldsymbol{0}$ one has the simple relation

$$E_\nu(0,0) = \frac{\hbar^2}{2m}\left(\frac{\pi}{d}\nu\right)^2, \quad \text{with} \quad \nu = 1, 2, 3, \ldots . \tag{4.24}$$

Another kind of defect is also easily seen from the LEED pattern: *Facetting* is the formation of new crystal planes, which are inclined to the original surface. The effect is often observed even on clean surfaces after annealing. The cause is the tendency of a crystal to lower its surface free energy by the formation of new lower-energy planes with different crystallographic orientations. These facets give rise to a secondary LEED pattern with spot separations different from that of the normal surface. The reciprocal lattice rods of these facets are strongly inclined with respect to those of the normal surface. The (00) spot originating from the facets will therefore be found far away from the normal (00) beam. For normal incidence of the primary beam the (00) spot of the original surface is located in the center of the diffraction screen. With increasing electron energy all other spots move continuously towards the (00) spot, whose position remains fixed. By the same argument the spots originating from the facets will move towards a certain position far out from the center of the screen. A similar consideration to that of Fig. 4.9 based on the Ewald construction allows the determination of the angle of inclination of the facets.

4.4 Dynamic LEED Theory, and Structure Analysis

As is seen in Fig. 4.5, there are so-called *secondary Bragg peaks* in the reflected intensity versus energy (I-V) curves of a LEED spot. These structures cannot be explained by simple kinematic theory, i.e., by taking into account only single-scattering events and a limited validity of the third Laue condition. The reason is that multiple-scattering processes are taking place in the solid as a result of the large atomic scattering cross section for low-energy electrons. The multiply-scattered electrons also contribute to the LEED spots (Fig. 4.10). In addition, strong inelastic-scattering processes are responsible for the fact that the electrons detected in a LEED experiment originate only from the first few atomic layers close to the surface. These complications require a more thorough theory which is usually called

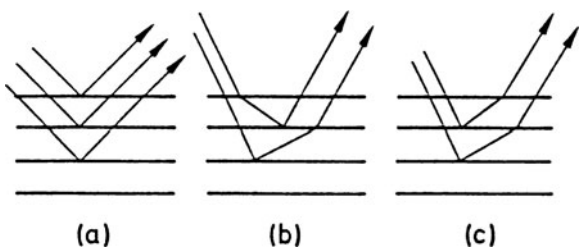

Fig. 4.10a–c Schematic representation of single and multiple scattering processes in LEED. (**a**) single-scattering events at the "lattice planes" cause a regular Bragg reflection. (**b**) Double-scattering events with forward- and subsequent back-scattering contribute to the (00) Bragg spot. (**c**) Double-scattering event with back-scattering and subsequent forward-scattering

dynamic theory [4.6]. The word *dynamic* implies that the complete dynamics of the electrons, and not merely the simple lattice geometry, is included.

Two approaches may be used. The straightforward solution to the problem consists in solving the complete Schrödinger equation for a perfect semi-infinite 3D lattice, using Bloch waves which satisfy the boundary conditions at the surface. The exact solution for the diffraction by the semi-infinite solid is then obtained by matching these Bloch waves to the wave functions of the incident and the reflected electrons. In the alternative approach only the 2D periodicity of the surface net is assumed, and the field solution of the Schrödinger equation is built up from contributions of successive atomic layers.

4.4.1 Matching Formalism

The *matching formulation* for the wave functions will be considered first. A particle beam is incident on a surface of a solid. For charged electrons this surface represents a potential step. Due to the potential difference refraction occurs (Fig. 4.11). At the surface ($z = 0$) the beam diameter changes but the total current I remains unchanged, since particles do not accumulate at the interface, i.e.,

$$I = I', \ \boldsymbol{j} \cdot \boldsymbol{A} = \boldsymbol{j}' \cdot \boldsymbol{A}, \tag{4.25}$$

where $\boldsymbol{j}$ and $\boldsymbol{j}'$ are the particle current densities on the two sides of the interface, and $\boldsymbol{A}$ is the area on the interface which is hit by the beam (Fig. 4.11). From the expression for the current density

$$\boldsymbol{j} = \frac{\hbar}{2im}(\psi^* \nabla \psi - \psi \nabla \psi^*) \tag{4.26}$$

and from (4.25) we obtain the following matching conditions for the electronic wave functions ψ_0 and ψ_i outside and inside the crystal

$$\psi_0|_{z=0} = \psi_i|_{z=0}, \tag{4.27a}$$

$$\frac{\partial}{\partial n}\psi_0\bigg|_{z=0} = \frac{\partial}{\partial n}\psi_i\bigg|_{z=0}, \tag{4.27b}$$

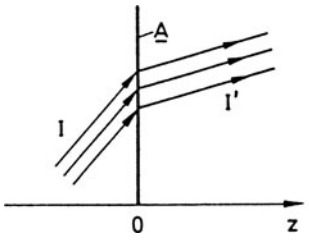

Fig. 4.11 A plane-wave electron beam hits an interface at $z = 0$ on an area A and is refracted due to a potential step. The total current I remains constant ($I = I'$)

where $\partial/\partial n$ is the derivative in the direction normal to the surface. With $E = \hbar^2 k^2/2m$ as the incident energy, the primary electrons are described by the wave function

$$\varphi_0 = \exp[\mathrm{i}\boldsymbol{k}_\parallel \cdot \boldsymbol{r}_\parallel + \mathrm{i}k_\perp z], \tag{4.28}$$

with

$$\boldsymbol{r}_\parallel = (x, y), \quad \boldsymbol{k} = (\boldsymbol{k}_\parallel, k_\perp) \text{ and } E = \frac{\hbar^2}{2m}(k_\parallel^2 + k_\perp^2).$$

The full wave function ψ_0 outside the crystal consists of this incoming wave and the diffracted waves. The surface scattering potential has 2D periodicity. Upon scattering, therefore $k_\parallel$ is conserved to within a 2D reciprocal lattice vector $\boldsymbol{G}_\parallel = \boldsymbol{G}_{hk} = h\boldsymbol{a}_1^* + k\boldsymbol{a}_2^*$ and the complete wavefunction outside becomes

$$\psi_0 = \varphi_0 + \sum_{hk} A_{hk} \exp[\mathrm{i}(\boldsymbol{k}_\parallel + \boldsymbol{G}_{hk}) \cdot \boldsymbol{r}_\parallel - \mathrm{i}k_{\perp,hk} z]. \tag{4.29}$$

A_{hk} describes the amplitudes of the scattered waves (h, k), and $k_{\perp,hk}$ are the wave-vector components normal to the surface, which are determined by energy conservation:

$$E = \frac{\hbar^2}{2m}(|\boldsymbol{k}_\parallel + \boldsymbol{G}_{hk})|^2 + k_{\perp,hk}^2). \tag{4.30}$$

Inside the solid the wavefunctions of the electrons are Bloch waves

$$\psi_i = u_{\boldsymbol{k}}(\boldsymbol{r}) \exp(\mathrm{i}\boldsymbol{k} \cdot \boldsymbol{r}) = \sum_{\boldsymbol{G}} c_{\boldsymbol{G}}(\boldsymbol{k}) \exp[\mathrm{i}(\boldsymbol{k} + \boldsymbol{G}) \cdot \boldsymbol{r}]; \tag{4.31}$$

$u_{\boldsymbol{k}}(\boldsymbol{r})$ has the periodicity of the 3D lattice and can therefore be represented as a Fourier series in 3D reciprocal space. $\boldsymbol{k}$ in (4.31) can also be split up into components $\boldsymbol{k}_\parallel$ and $k_\perp$ parallel and normal to the surface. The coefficients $c_{\boldsymbol{G}}(\boldsymbol{k})$ and the wave vectors $k_\perp$ are determined by the periodic potential and the energy. They are found by substituting the above expression (4.31) into the Schrödinger equation for the periodic crystal potential. The matching conditions (4.27) imply for the wave functions (4.29 and 4.31) outside and inside the crystal, that the parallel wave-vector components $\boldsymbol{k}_\parallel$ and the total energy E coincide outside and inside. The matching conditions (4.27) can lead to severe restrictions on the possible diffracted beams in comparison with pure kinematic theory. For a certain energy E, which is determined by the acceleration voltage V of the primary beam, the matching conditions can only be fulfilled if there exist electronic states inside the crystal at this energy. The electronic band structure with its allowed and forbidden bands is therefore of considerable importance for the intensity of a particular reflected beam (hk). If the energy E falls in a forbidden gap of the band structure, the wave functions

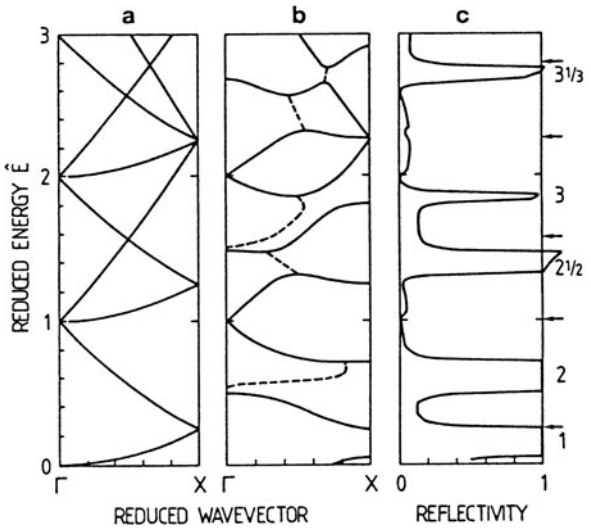

Fig. 4.12a–c The band structure and the reflectivity of a semi-infinite cubic array of s-wave scatterers with a (100) surface exposed. (**a**) Free-electron band structure along the symmetry direction $\Gamma - X$ of the Brillouin zone. (**b**) Calculated band structure along $\Gamma - X$. The periodic potential causes a splitting into allowed bands (full line) and "forbidden" bands of states with complex wave vector (dotted lines). (**c**) Reflectivity of electrons at normal incidence on the (100) surface; i.e. I-V curve for the (00) spot in a LEED experiment. The arrows denote the positions of maxima from kinematic theory (3rd Laue condition). The energy scale E is in atomic units times $(2\pi/\mathrm{d})^2$ [4.7]

outside can not be matched to a Bloch state inside, and a peak in the reflected LEED intensity results (Fig. 4.12). The model calculations in Fig. 4.12 [4.7] have been performed on a semi-infinite cubic array (primitive lattice) of s-wave scatterers. Such a potential has essentially the same properties as an array of δ-function potentials. Normal incidence on the (100) face of this model crystal is considered, i.e. the band structure along the $\Gamma - X$ symmetry line of the Brillouin zone is important. Figure 4.12 exhibits both the free-electron band structure (**a**) and the bands calculated under the assumption of s-wave scatterers. In Fig. 4.12c the calculated reflected intensity of a normally incident electron beam is displayed. Gaps in the band structure are related to maxima in the reflectivity, since here no Bloch states are available inside the crystal for matching to the outside wave field. On the other hand, the external electronic wave functions in these regions cannot abruptly end at the surface. A detailed calculation, however, shows that, for energies within the forbidden gaps, electronic states exist at the surface. Their wave functions decay exponentially into the interior of the crystal. These states are localized at the surface (Chap. 6); in contrast to the Bloch states with real wave vectors $\boldsymbol{k}$ in (4.31) they are characterized by a complex $\boldsymbol{k}$. The imaginary part $\mathrm{Im}k_\perp$ gives the decay length of the wave functions. These decaying states are used to match the outside wave field at energies where Bloch states are forbidden. The regions of high reflectivity shown in Fig. 4.12c thus correspond to the phenomenon of total reflection of electromagnetic

waves on a dielectric surface. The arrows in Fig. 4.12c depict the energetic positions expected for the maxima in the I-V curve on the basis of simple application of the third Laue condition (in the z-direction) in kinematic theory. When compared with an experimentally determined I-V curve (Fig. 4.5) the higher energy peaks of the calculated I-V curve are sharper and more intense. The reasons for this discrepancy might lie in the neglect of all inelastic scattering processes of electron-electron interactions.

4.4.2 Multiple-Scattering Formalism

In the second dynamic approach to understand the LEED intensity patterns, the scattered wave field is built up from scattering processes on different lattice planes below the surface. In this formalism, the first step is the calculation of the scattering amplitudes from a single atom. For different primary energies, scattering phases are calculated, usually for s, p and d scattering. Muffin-tin potentials are often used for this purpose. The next step involves the calculation of scattering processes within a single atomic layer, to give the so-called *intra-layer multiple scattering*.

The final solution is then obtained by considering scattering between different atomic planes, or the so-called *inter-layer multiple scattering*. How many layers have to be taken into account depends on the penetration depth of the primary electrons. For 1000 eV electrons, this depth is approximately 10 Å (Fig. 4.1); calculations based on 8 atomic layers yield an estimated accuracy of about 1%. The wave field between the different atomic layers is composed of sets of forward and backward travelling beams, e.g. forward scattering on the first layer contributes to the amplitude backscattered at the second layer, etc. This multiple scattering approach to the LEED problem gives essentially the same results as the matching formalism. This has been shown for several model calculations. In Fig. 4.13 the IV curves of the (00) and (10) beams are plotted for the same model crystal as above (semi-infinite cubic array of s-wave scatterers). The calculations are made both on the basis of the matching method and using the multiple scattering formalism [4.8]. Both approaches yield essentially the same features. It is worth mentioning that dynamic LEED theory has been extended to spin-dependent scattering [4.9]. In this case, instead of the Schrödinger equation, the relativistic Dirac equation is used to describe the dynamics of the electrons. The degree of spin polarization in the scattered electron beam is calculated as a function of primary energy and scattering angle.

4.4.3 Structure Analysis

The analysis of experimental data using the dynamic theory of elastic electron scattering is now established as one of the major tools in the determination of atomic surface structure. From simple inspection and measurement of the geometric

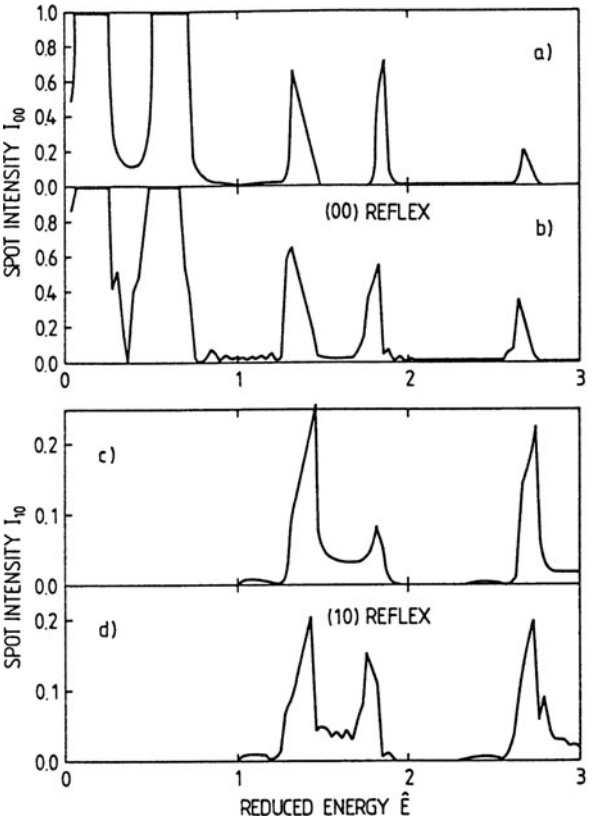

Fig. 4.13a–d Dynamic calculations of the *I-V* curves of the (00) and the (10) Bragg spots for a semi-infinite cubic array of *s*-wave scatterers. The primary electron beam is incident normal to the (100) face; (**a** and **c**) by means of the matching formalism; (**b** and **d**) by means of the multiple scattering formalism [4.7, 4.8]

separation of the LEED spots on the phosphorus screen, only the dimensions and the symmetry of the 2D surface lattice can be determined. In other words, the reciprocal lattice depicted in the diffraction pattern yields information only about distances and angles of the 2D unit mesh in real space (Sect. 4.3). As in bulk solid-state physics, the atomic configuration, i.e. the atomic coordinates within the unit cell, can only be obtained by measuring the intensity of the Bragg spots. For X-ray scattering from bulk solids, simple kinematic theory can be used to relate structural models to the experimentally observed Bragg-spot intensities. This is not the case for a LEED experiment in surface physics; here the much more complex dynamic approach has to be applied to relate a structural model, i.e., a proposed set of atomic coordinates in the topmost atomic layers to the observed LEED spot intensities. For this purpose the intensity of a number of LEED beams is measured as a function of primary energy (*I-V* curves). A set of possible atomic coordinates for the atoms in the topmost layers is used as input for a dynamic calculation of these *I-V* curves and the results are compared with the experimental data. Depending on the quality of the fit, the structural model may be modified and a new calculation made; this "trial and error" procedure (Fig. 4.14) is repeated until satisfactory agreement is obtained.

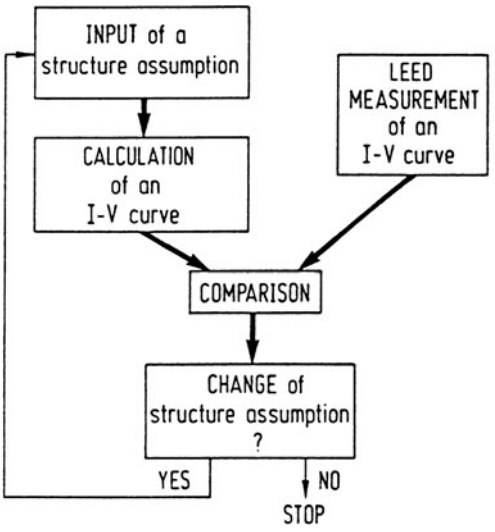

Fig. 4.14 Flow diagram for a LEED structure analysis by means of dynamic theory. The calculations require big computers and the analysis must be made for a number of different Bragg spots

One severe problem in establishing a definite model for the surface atomic structure lies in the procedure for comparing the calculated with the measured I-V curves. Simple inspection often leads to debate as to what is good and what is poor agreement. To prove a more objective assessment of the quality of a fit, so-called *reliability functions* have been introduced. For a thorough structural analysis, I-V curves for a considerable number of Bragg spots have to be measured and calculated.

4.5 Kinematics of an Inelastic Surface Scattering Experiment

In almost all inelastic scattering processes on crystalline surfaces – be it with slow electrons, atoms, ions, etc. – the energy and the wave vector parallel to the surface are conserved (4.18), i.e.

$$E' - E = \hbar\omega, \tag{4.32a}$$

$$\boldsymbol{k}'_{\parallel} - \boldsymbol{k}_{\parallel} = \boldsymbol{q}_{\parallel} + \boldsymbol{G}_{\parallel}. \tag{4.32b}$$

Equation (4.32b) is a direct consequence of the 2D translational symmetry of a perfect crystalline surface. $\boldsymbol{G}_{\parallel}$ is an arbitrary 2D reciprocal lattice vector. If the scattering process involves irregularly distributed centers on the surface, e.g. statistically adsorbed atoms or defects, then (4.32b) breaks down and only the energy conservation (4.32a) is valid. The energy $\hbar\omega$ and wave vector $\boldsymbol{q}_{\parallel}$ may be transferred to collective surface excitations like phonons, plasmons, magnons, etc. to single particles like electrons in the conduction band (intra-band scattering), or to electrons excited from an occupied electronic band into an empty one (inter-band scattering).

In all these cases, the characteristic excitation energy $\hbar\omega$ requires a definite $\boldsymbol{q}_\parallel$ transfer. On a periodic crystal surface collective excitations are described by a dispersion relation $\hbar\omega(\boldsymbol{q}_\parallel)$ and in scattering processes within or between electronic bands the band structure $E(\boldsymbol{k})$ fixes the $\boldsymbol{q}_\parallel$ transfer for a particular energy transfer $\hbar\omega$:

$$E'(\boldsymbol{k}'_\parallel) - E(\boldsymbol{k}_\parallel) = \hbar\omega(\boldsymbol{q}_\parallel). \tag{4.33}$$

The determination of such dispersion relations or surface band structures $E(\boldsymbol{k}_\parallel)$ is one of the major incentives for performing inelastic scattering on surfaces. In these experiments, therefore, the energy of the incident particles (E) and of the scattered particles (E') has to be determined by energy analysers (Panel II: Chap. 1). The wave vectors $\boldsymbol{k}$ and $\boldsymbol{k}'$ are determined by the energy and the scattering geometry. Applying energy and wave-vector conservation (4.32b) the experimental geometry uniquely relates the $\boldsymbol{q}_\parallel$ transfer to the energy transfer $\hbar\omega$. Figure 4.15 depicts the geometry of a surface scattering experiment. The incoming particles have the wave vector $\boldsymbol{k}$. Scattering in the specular direction with $|\boldsymbol{k}_\mathrm{s}| = |\boldsymbol{k}|$ represents the elastic process, whereas inelastic processes generally involve scattering out of the specular direction (described by the angles ψ and φ). The scattered wave vector $\boldsymbol{k}'$ then differs from the specular vector $\boldsymbol{k}_\mathrm{s}$ by the transfer vector $\boldsymbol{q}$, i.e. for the case $\boldsymbol{G}_\parallel = 0$,

$$\boldsymbol{k}' = \boldsymbol{k} - \begin{pmatrix} q_x \\ q_y \\ \Delta k_z \end{pmatrix}. \tag{4.34}$$

For the transfer vector $\boldsymbol{q} = (q_x, q_y, \Delta k_z)$ only the components q_x and q_y parallel to the surface are fixed by a conservation law, i.e. can be found in a corresponding surface excitation. Δk_z is determined from the energy and scattering geometry only

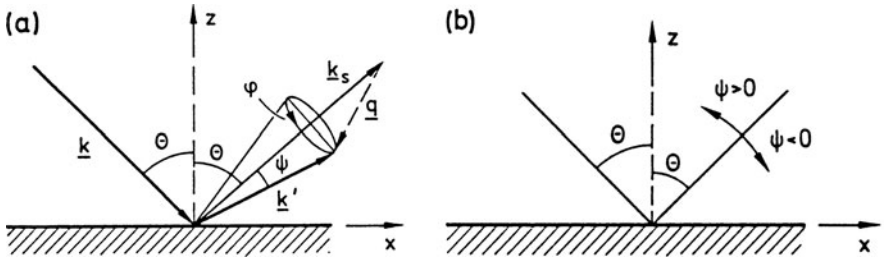

Fig. 4.15 (**a**) Geometry of an inelastic scattering experiment. The plane of incidence is the xz plane of the coordinate system (x axis parallel to surface). The primary beam is described by the wave vector $\boldsymbol{k}$ (angle of incidence θ). Elastically scattered particles escape with a wave vector $\boldsymbol{k}_\mathrm{s}$ (specular direction). Inelastically scattered particles are found with a wavevector $\boldsymbol{k}'$. The wave vector change is $\boldsymbol{q}$. The zero of the angle φ is in the plane of incidence. (**b**) Special case of "planar scattering" where the detection direction is in the plane of incidence ($\varphi = 0$). ψ is measured from the specular direction

and is in no way related to any excitation. The excitations can have any wave-vector component normal to the surface. Energy conservation (4.33) is expressed as

$$\frac{\hbar^2 k'^2}{2m} = \frac{\hbar^2 k^2}{2m} - \hbar\omega, \tag{4.35a}$$

$$k' = k(1 - \hbar\omega/E)^{1/2}. \tag{4.35b}$$

The geometric relation between $\boldsymbol{k}'$ and $\boldsymbol{k}$ in Fig. 4.15 is most readily derived in a coordinate system whose z-axis is along the specular direction, i.e., a system which is rotated by the angle θ with respect to the z-axis depicted in Fig. 4.15. In this rotated system, the specular wave vector $\boldsymbol{k}_\mathrm{s}$ and the inelastically scattered wave vector $\boldsymbol{k}'$ have the simple representations

$$\boldsymbol{k}_\mathrm{s} = k \begin{pmatrix} 0 \\ 0 \\ 1 \end{pmatrix} \quad \text{and} \quad \boldsymbol{k}' = k' \begin{pmatrix} -\sin\psi\cos\varphi \\ \sin\psi\sin\varphi \\ \cos\psi \end{pmatrix}. \tag{4.36}$$

Their representation in the coordinate system of Fig. 4.15 with the z-axis normal to the surface, is obtained by a rotation around the y-axis (parallel to surface) by means of the rotation matrix

$$\boldsymbol{R} = \begin{pmatrix} \cos\theta & 0 & \sin\theta \\ 0 & 1 & 0 \\ -\sin\theta & 0 & \cos\theta \end{pmatrix}. \tag{4.37}$$

We thus obtain for the specular and for the inelastically scattered beam:

$$\boldsymbol{k}_\mathrm{s} = k \begin{pmatrix} \sin\theta \\ 0 \\ \cos\theta \end{pmatrix}. \tag{4.38}$$

$$\boldsymbol{k}' = k' \begin{pmatrix} -\sin\psi\cos\varphi\cos\theta + \cos\psi\sin\theta \\ \sin\psi\sin\varphi \\ \sin\psi\cos\varphi\sin\theta + \cos\psi\cos\theta \end{pmatrix}. \tag{4.39}$$

Combining (4.34, 4.38, 4.39) with the energy conservation (4.35b) one arrives at

$$\boldsymbol{k} - \boldsymbol{k}' = \boldsymbol{q} = \begin{pmatrix} q_x \\ q_y \\ \Delta k_z \end{pmatrix}$$

$$= k \left[\begin{pmatrix} \sin\theta \\ 0 \\ -\cos\theta \end{pmatrix} - \sqrt{1 - \frac{\hbar\omega}{E}} \begin{pmatrix} \cos\psi\sin\theta - \sin\psi\cos\varphi\cos\theta \\ \sin\psi\sin\varphi \\ \sin\psi\cos\varphi\sin\theta + \cos\psi\cos\theta \end{pmatrix} \right]. \tag{4.40}$$

In an inelastic scattering experiment now the orientation of the primary beam relative to the surface determines the angle of incidence θ, and the position of the entrance aperture to the energy analyser is described by the angles ψ and φ with respect to the specular direction (Fig. 4.15a). An observed energy transfer $\hbar\omega$ (loss or gain) at a particular primary energy E then corresponds to a certain wave-vector transfer $\boldsymbol{q}$ via (4.40). The component $\boldsymbol{q}_\parallel = (q_x, q_y)$ parallel to the surface is conserved in the scattering process, i.e., it can be found as the wave vector of a particular surface excitation. The component Δk_z is determined by energy conservation, but it has no meaning for the surface excitations.

Equation (4.40) simplifies considerably for the special case of planar scattering where the scattered beam is detected in the plane of incidence (parallel to x-axis in Fig. 4.15). The wave-vector transfer parallel to the surface $q_\parallel = q_x$, is then given by ($\varphi = 0, \pi$):

$$q_\parallel = k[\sin\theta + \sqrt{1 - \hbar\omega/E}(\sin\psi\cos\theta - \cos\psi\sin\theta)]. \tag{4.41}$$

For a typical, inelastic-scattering experiment with low-energy electrons (HREELS, Panel IX: Chap. 4) the dependence of the energy loss $\hbar\omega$ on the wave-vector transfer $q_\parallel$ according to (4.41) is plotted in Fig. 4.16. For detection in the specular direction ($\psi = 0$) the curves originating at the zero point are calculated for different

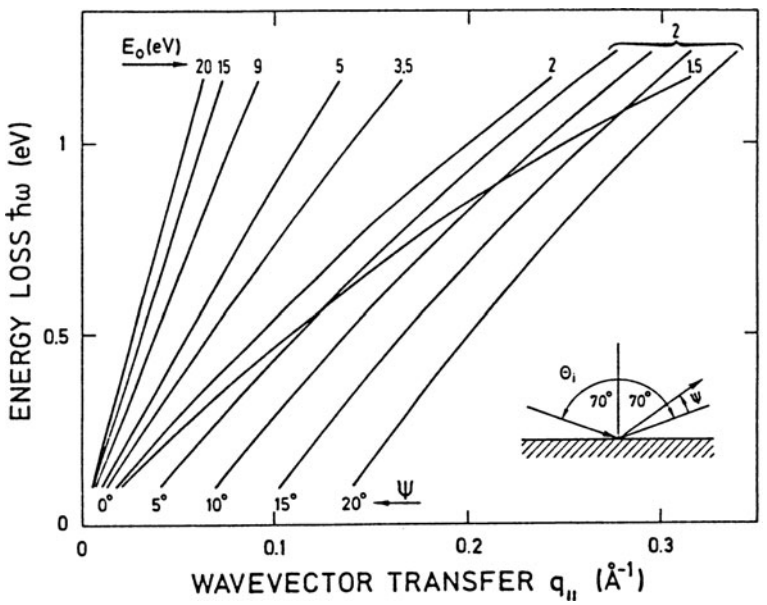

Fig. 4.16 Energy transfer (loss) $\hbar\omega$ as a function of the corresponding wavevector transfer $q_\parallel$ for inelastic scattering of low energy electrons. For the specular detection ($\psi = 0$) the curves for different primary energies $E = 1.5, 2, \ldots 20$ eV all pass through the origin. The curves for off-specular detection with $\psi = 5°, 10°, 15°, 20°$ are for a fixed primary energy of $E = 2$ eV

primary energies E ranging between 1.5 and 20 eV. For a fixed primary energy of 2 eV, curves are shown for detection directions deviating from the specular direction by the angles $\psi = 2°, 10°, 15°, 20°$. As is clearly seen from (4.41) and from Fig. 4.16, the wavevector transfer $q_\parallel$ in an inelastic scattering experiment can be varied by changing the ratio $\hbar\omega/E$ or by changing the detection angle ψ (off-specular detection). Figure 4.16 displays the situation for a typical HREELS experiment, but similar curves with loss energies and $q_\parallel$ values on a different scale are obtained for the scattering of atoms or ions. For He atoms scattered inelastically from a crystalline surface with loss or gain energies in the 10 meV range, $q_\parallel$ transfers in the 1 $Å^{-1}$ range can easily be obtained (Panel X: Chap. 5).

A particularly simple situation occurs for specular detection ($\psi = 0$) and primary energies E that are large in comparison to the observed loss energies ($\hbar\omega/E \ll 1$). In this case (4.41) simplifies to

$$q_\parallel \simeq k \sin\theta(\hbar\omega/2E). \tag{4.42}$$

This case of small $\hbar\omega/2E$ and specular detection is important when low-energy electrons are scattered on a dynamic long-range potential. Such a potential, if expanded into a Fourier series, gives only components at small $q_\parallel$ values. Therefore the inelastically scattered intensity is peaked around $q_\parallel \simeq 0$, i.e. around the specularly reflected beam (Sect. 4.6).

4.6 Dielectric Theory of Inelastic Electron Scattering

Among the variety of particles that can be used for surface scattering experiments, low-energy electrons play a rather important role. There are several reasons for this: slow electrons can be produced by a simple electron gun and like all charged particles can easily be dispersed by electrostatic energy analysers and detected by a channeltron or another kind of electron multiplier. On the theoretical side, a rather simple mathematical approach is possible for inelastic scattering in long-range potentials. For electrons an example of such long-range scattering potentials are oscillating dipole fields on a surface. These dipole fields may originate from collective excitations such as surface lattice vibrations (phonons) and surface plasmons (Chap. 5) or from dynamic dipole moments of vibrating adsorbed molecules and atoms. Scattering cross sections can, of course, be calculated by using the dipole fields as scattering potentials within the formalism of Sect. 4.1.

It must be emphasized, however, that apart from this type of scattering by long-range dipole fields there exist other – from the theoretical standpoint more complex – scattering mechanisms for slow electrons [4.10]. Interaction with the local atomic potential of a surface atom must be described in a more localized picture since the scattering potential extends only over atomic dimensions. An expansion of such a short-range scattering potential as a Fourier series in wave vectors $\boldsymbol{q}_\parallel$ includes rather large $\boldsymbol{q}_\parallel$ values and thus leads to scattering at large angles from the specular direction (Fig. 4.15a). This type of scattering is often called *impact scattering*. A possible mechanism involves the virtual excitation of an electronic state of a

surface atom (in the substrate or the adsorbate); the inelastically scattered electron briefly occupies an excited state of this atom and escapes with an energy differing from the primary energy by a vibrational quantum (phonon, plasmon or adsorbate vibration).

From these qualitative arguments about the spatial range of the scattering potential and the resulting wave-vector transfers, it is evident that impact scattering and scattering in long-range dipole fields can be distinguished experimentally by the angular distribution of the inelastically scattered electrons around the specular reflection direction. Strong peaking of the scattered intensity in this direction clearly indicates scattering in long-range dipole fields. Care has to be taken in the interpretation of data when *Umklapp processes* ($\boldsymbol{G}_{\parallel} \neq 0$) are involved.

We will see in the following that these qualitative arguments follow quite naturally from the simple theoretical approach to scattering in long-range dipole fields, the so-called *dielectric theory*.

4.6.1 Bulk Scattering

The dielectric approach was first applied by Fermi [4.11], and Hubbard and Fröhlich [4.12] to inelastic scattering of high-energy electrons (several keV range) which penetrate thin solid films. Because of the long-range nature of the scattering potential a quasi-continuum theory is used, in which the dielectric properties of the solid are described by its complex dielectric function $\epsilon(\omega) = \epsilon_1 + \mathrm{i}\epsilon_2$. We first consider briefly the bulk scattering process, where an electron penetrates a solid and loses part of its energy inside the bulk. This energy transfer is ascribed to the shielding of the Coulomb field of the moving electron due to the surrounding dielectric medium. The total energy transfer W is thus given by the change in the energy density of the Coulomb field inside the solid. Since in the present model calculation the bulk solid, which is penetrated by the electron, is assumed to be extended into infinity, the energy loss per unit time, i.e., the energy transfer rate is calculated as the finite quantity

$$\dot{W} = \mathrm{Re}\left\{\int \mathrm{d}\boldsymbol{r}\boldsymbol{\mathcal{E}} \cdot \dot{\boldsymbol{D}}\right\}. \tag{4.43}$$

If the complex representations of the $\mathcal{E}$ and $\boldsymbol{D}$ fields are used, only the real part of the integral describes an energy loss.

The fields are expanded in Fourier series

$$\boldsymbol{\mathcal{E}}(\boldsymbol{r}, t) = \int \mathrm{d}\omega \mathrm{d}\boldsymbol{q}\hat{\boldsymbol{\mathcal{E}}}(\omega, \boldsymbol{q})\mathrm{e}^{-\mathrm{i}(\omega t + \boldsymbol{q}\cdot\boldsymbol{r})} \tag{4.44}$$

and similarly for $\boldsymbol{D}(\boldsymbol{r}, t)$, whose Fourier components $\hat{\boldsymbol{D}}(\omega, \boldsymbol{q})$ are related to $\hat{\mathcal{E}}(\omega, \boldsymbol{q})$ via

$$\hat{\boldsymbol{D}}(\omega, \boldsymbol{q}) = \epsilon_0\epsilon(\omega, \boldsymbol{q})\hat{\boldsymbol{\mathcal{E}}}(\omega, \boldsymbol{q}). \tag{4.45}$$

For the calculation of (4.43) it is convenient to substitute ω by $-\omega'$ in $\hat{\boldsymbol{D}}(\omega, \boldsymbol{q})$:

$$\dot{W} = \mathrm{Re}\left\{\int \mathrm{d}\boldsymbol{r}\mathrm{d}\omega'\mathrm{d}\omega\mathrm{d}\boldsymbol{q}'\mathrm{d}\boldsymbol{q}\frac{\mathrm{i}\omega'}{\epsilon_0\epsilon(\omega,\boldsymbol{q})}\hat{\boldsymbol{D}}(\omega,\boldsymbol{q})\cdot\hat{\boldsymbol{D}}(-\omega',\boldsymbol{q}')\mathrm{e}^{\mathrm{i}(\omega'-\omega)t}\mathrm{e}^{-\mathrm{i}(\boldsymbol{q}+\boldsymbol{q}')\cdot\boldsymbol{r}}\right\}. \tag{4.46}$$

With the representation for the δ-function

$$\int \mathrm{d}\boldsymbol{r}\mathrm{e}^{-\mathrm{i}(\boldsymbol{q}+\boldsymbol{q}')\cdot\boldsymbol{r}} = (2\pi)^3\delta(\boldsymbol{q}+\boldsymbol{q}') \tag{4.47}$$

one obtains

$$\dot{W} = (2\pi)^3\mathrm{Re}\left\{\int \mathrm{d}\omega'\mathrm{d}\omega\mathrm{d}\boldsymbol{q}\frac{\mathrm{i}\omega'}{\epsilon_0\epsilon(\omega,\boldsymbol{q})}\hat{\boldsymbol{D}}(\omega,\boldsymbol{q})\cdot\hat{\boldsymbol{D}}(-\omega',-\boldsymbol{q})\mathrm{e}^{\mathrm{i}(\omega'-\omega)t}\right\}. \tag{4.48}$$

Since the $\boldsymbol{D}$ field is directly related to the moving point charge e through $\mathrm{div}\boldsymbol{D} = e\delta(\boldsymbol{r}-\boldsymbol{v}t)$, the Fourier components $\hat{\boldsymbol{D}}(\omega,\boldsymbol{q})$ include the time and spatial structures of the field of the moving electron. From

$$\boldsymbol{D} = -\frac{e}{4\pi}\nabla\frac{1}{|\boldsymbol{r}-\boldsymbol{v}t|} = \frac{e}{4\pi|\boldsymbol{r}-\boldsymbol{v}t|^3}(\boldsymbol{r}-\boldsymbol{v}t) \tag{4.49}$$

the Fourier transform is calculated by using the relations

$$\frac{e^{-\alpha r}}{r} = \int f(\boldsymbol{q})\mathrm{e}^{\mathrm{i}\boldsymbol{q}\cdot\boldsymbol{r}}\mathrm{d}\boldsymbol{q}, \tag{4.50a}$$

$$f(\boldsymbol{q}) = (2\pi)^{-3}\int\frac{e^{-\alpha r}}{r}\mathrm{e}^{-\mathrm{i}\boldsymbol{q}\cdot\boldsymbol{r}}\mathrm{d}\boldsymbol{r}. \tag{4.50b}$$

With $\alpha = 0$ and by use of the representation $\mathrm{d}\boldsymbol{r} = \mathrm{d}\varphi\mathrm{d}\theta\sin\theta r^2\mathrm{d}r$ in spherical coordinates it follows

$$\frac{1}{r} = (2\pi)^{-3}\int\mathrm{d}\boldsymbol{q}\left(\frac{4\pi}{q^2}\right)\mathrm{e}^{\mathrm{i}\boldsymbol{q}\cdot\boldsymbol{r}} \tag{4.51}$$

and

$$\boldsymbol{D}(\boldsymbol{r},t) = e(2\pi)^{-3}\int\mathrm{d}\boldsymbol{q}q^{-2}\boldsymbol{q}\mathrm{e}^{-\mathrm{i}\boldsymbol{q}\cdot(\boldsymbol{r}-\boldsymbol{v}t)}, \tag{4.52}$$

respectively. Using the identity

$$\mathrm{e}^{\mathrm{i}\boldsymbol{q}\cdot\boldsymbol{v}t} = \int\mathrm{d}\omega\mathrm{e}^{-\mathrm{i}\omega t}\delta(\omega-\boldsymbol{q}\cdot\boldsymbol{v}) \tag{4.53}$$

one finally obtains

$$\hat{\boldsymbol{D}}(\omega, \boldsymbol{q}) = \frac{e}{(2\pi)^3}\boldsymbol{q}\frac{1}{q^2}\delta(\omega + \boldsymbol{q}\cdot\boldsymbol{v}). \tag{4.54}$$

With $\delta(x) = \delta(-x)$ the following expression follows for the energy-loss rate (4.43)

$$\dot{W} = \frac{e^2}{\epsilon_0(2\pi)^3} \times \mathrm{Re}\left\{\int \mathrm{d}\omega'\mathrm{d}\omega \frac{\mathrm{i}\omega'}{q^2\epsilon(\omega,\boldsymbol{q})}\delta(\omega' + \boldsymbol{q}\cdot\boldsymbol{v})\delta(\omega + \boldsymbol{q}\cdot\boldsymbol{v})\mathrm{e}^{\mathrm{i}(\omega'-\omega)t}\mathrm{d}\boldsymbol{q}\right\}. \tag{4.55a}$$

For a particular $\boldsymbol{q}$ it follows $\omega' = \omega$ and the time dependence in (4.55a) disappears:

$$\dot{W} = \frac{e^2}{\epsilon_0(2\pi)^3}\int \mathrm{d}\omega\mathrm{d}\boldsymbol{q}\frac{\omega}{q^2}\mathrm{Im}\left\{\frac{-1}{\epsilon(\omega,\boldsymbol{q})}\right\}\delta(\omega + \boldsymbol{q}\cdot\boldsymbol{v}). \tag{4.55b}$$

We decompose the wave-vector transfer $\boldsymbol{q}$ into the components $\boldsymbol{q}_\parallel$ and $\boldsymbol{q}_\perp$ parallel and perpendicular to the electron velocity (cylindrical coordinates around the electron trajectory) and find by means of

$$\boldsymbol{q}\cdot\boldsymbol{v} = q_\parallel v,\quad q^2 = q_\parallel^2 + q_\perp^2,\quad \mathrm{d}\boldsymbol{q} = q_\parallel \mathrm{d}\varphi\mathrm{d}q_\parallel\mathrm{d}q_\perp \tag{4.56}$$

from the δ-function in (4.55b), that maximum energy transfer takes place for

$$v = \left|\frac{\omega}{q_\parallel}\right|. \tag{4.57}$$

An energy loss thus results when harmonic excitations of the solid have a phase velocity $\omega/q_\parallel$ which equals the electron velocity; i.e., in order to take over energy from the moving electron, the solid excitation must propagate in phase with the electron.

Using (4.56) and the relation $\delta(\omega + q_\parallel v) = v^{-1}\delta(\omega/v + q_\parallel)$ one obtains for the energy-loss rate (4.55b)

$$\dot{W} = \frac{e^2}{(2\pi)^3\epsilon_0 v}\int \mathrm{d}\omega\mathrm{d}q_\perp\mathrm{d}\varphi\omega\frac{q_\perp}{(\omega/v)^2 + q_\perp^2}\mathrm{Im}\left\{\frac{-1}{\epsilon(\omega,q)}\right\}. \tag{4.58}$$

For a circular analyser aperture the integration over φ yields 2π and the q dependence in $\epsilon(\omega,\boldsymbol{q})$ can be neglected since for higher electron velocities $q_\parallel$ is negligibly small. It thus follows with $q_\perp\mathrm{d}q_\perp = \mathrm{d}q_\perp^2/2$:

$$\dot{W} = \frac{e^2}{4\pi^2\epsilon_0 v}\int \omega\mathrm{d}\omega\mathrm{Im}\left\{\frac{-1}{\epsilon(\omega)}\right\}\int \frac{q_\perp\mathrm{d}q_\perp}{(\omega/v)^2 + q_\perp^2}$$

$$= \frac{e^2}{4\pi^2\epsilon_0 v}\left\{\ell n\left[\left(\frac{\omega}{v}\right)^2 + q_\perp^2\right]\right\}\Bigg|_0^{q_c} \int \omega \mathrm{d}\omega \mathrm{Im}\left\{\frac{-1}{\epsilon(\omega)}\right\}, \tag{4.59}$$

where the upper possible wave-vector transfer q_c can be at most the reciprocal lattice constant $1/a$ of the crystalline solid.

The total energy transfer rate (4.59) is composed of components with different angular frequencies ω. The solid can, however, offer only particular characteristic excitations with quantum energy $\hbar\omega$, to which energy can be transferred. The spectral response of the solid in an inelastic electron scattering experiment is thus described within the framework of dielectric theory by the so-called *bulk-loss function*

$$\mathrm{Im}\left\{\frac{-1}{\epsilon(\omega)}\right\} = \frac{\epsilon_2(\omega)}{\epsilon_1^2(\omega) + \epsilon_2^2(\omega)}. \tag{4.60}$$

Essential spectral structure in an electron energy loss spectrum therefore occurs when the nominator in (4.60), $\epsilon_2(\omega)$, i.e., essentially the optical absorption of the material exhibits peaks, e.g., due to electronic interband transitions. But the main spectral features arise from the condition $\epsilon_1(\omega) \simeq 0$ in regions, where $\epsilon_2(\omega)$ is small and monotonic. The condition $\mathrm{Re}\{\epsilon(\omega)\} \simeq 0$ determines, on the other hand, the frequencies ω of the longitudinal collective excitations of a solid as, e.g., the plasma waves of a free electron gas [4.13].

In electron energy loss experiments, where bulk scattering prevails, the essential spectral structure, therefore, is due to the excitation of the bulk plasmon, whose excitation energy is found, in accordance with bulk electron densities in the 10^{22} to $10^{23}\,\mathrm{cm}^{-3}$ range, between 5 and 20 eV (Figs. 4.23, IX.4 and IX.5).

4.6.2 Surface Scattering

In surface physics the primary energy ($E < 20\,\mathrm{eV}$) used in reflection scattering experiments is so small that the electrons penetrate only a few Ångstroms into the solid (Fig. 4.1). The time which they spend within the material is so short that bulk scattering according to (4.60) is a negligible process. Nevertheless, the long-range Coulomb field of the electrons penetrates into the solid as they approach the surface and on their way back after reflection (Fig. 4.17). Thus, while in the vicinity of the surface, they interact with the material via their Coulomb field. The shielding of the penetrating field gives rise to surface scattering processes [4.10, 4.14] which can be treated mathematically in a similar way to the above bulk scattering mechanism. For this purpose the electron trajectory $\boldsymbol{s}(t)$ is assumed to be essentially that of an elastically scattered electron (velocity $\boldsymbol{v}$). The time $t = 0$ is taken to be the moment of the reflection at the solid surface ($z = 0$). The position and velocity of the electron are described according to Fig. 4.17 by

$$\boldsymbol{s}(t) = \boldsymbol{v}t = \boldsymbol{v}_\parallel t + v_\perp t\hat{\boldsymbol{e}}_z, \tag{4.61a}$$

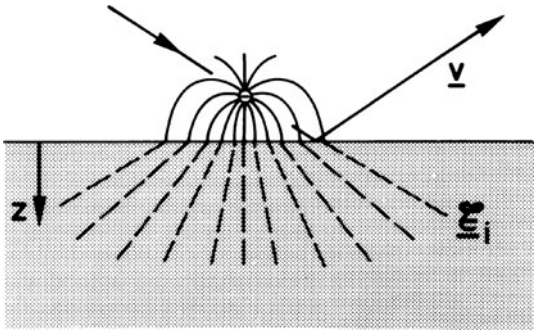

Fig. 4.17 Schematic plot of the inelastic dielectric scattering process of a low-energy electron (velocity $\boldsymbol{v}$) on a semi-infinite halfspace ($z > 0$). The energy transfer (energy loss) to the solid is due to shielding of the interior electric field $\mathcal{E}_\mathrm{i}$ of the electron outside the surface. Since the energy transfer (loss) is assumed to be small in comparison with the kinetic energy of the electron, the electron trajectory is quasi-elastic

and because of the small energy losses $\hbar\omega \ll E$

$$v_\perp(t < 0) = |v_\perp| \simeq -v_\perp(t > 0), \tag{4.61b}$$

where $\parallel$ and $\perp$ denote the components parallel and normal to the surface. $\hat{\boldsymbol{e}}_z$ is a unit vector in the z-direction. The $\boldsymbol{D}$ field of the moving electron far away from the surface is the same as it would be if the semi-infinite solid at $z > 0$ were not present (4.52). According to classical electrodynamics the external field of a point charge outside a semi-infinite dielectric medium can be described by an image charge inside the solid; the field $\mathcal{E}_\mathrm{i}$ in the interior of the medium, however, has radial symmetry as if no interface were present, but it is shielded by a factor $2/(\epsilon+1)$ with respect to the field $\mathcal{E}$ of the free electron. Thus, for the Fourier components $\hat{\mathcal{E}}_\mathrm{i}$ we have

$$\hat{\boldsymbol{\mathcal{E}}}_\mathrm{i}(\boldsymbol{q},\omega) = \frac{2}{\epsilon(\omega)+1}\hat{\boldsymbol{\mathcal{E}}}(\boldsymbol{q},\omega) = \frac{\hat{\boldsymbol{D}}_\mathrm{i}(\boldsymbol{q},\omega)}{\epsilon_0\epsilon(\omega)}. \tag{4.62}$$

For our present problem of surface scattering, the conventional 3D Fourier series (4.44) is not a convenient representation of the electric field, since in a surface scattering experiment only the wave-vector component $\boldsymbol{q}_\parallel$ parallel to the surface is conserved rather than $\boldsymbol{q}$ (4.18b). The scattering cross section we are seeking should therefore be expressed as $P(\hbar\omega, \boldsymbol{q}_\parallel)$, and an expansion of the fields $\mathcal{E}$, $\boldsymbol{D}$ and $\mathcal{E}_\mathrm{i}$, $\boldsymbol{D}_\mathrm{i}$ in surface waves $\exp(\mathrm{i}\boldsymbol{q}_\parallel \cdot \boldsymbol{r}_\parallel - q_\parallel|z|)$ would be more appropriate. This expansion is indeed possible since we can integrate the 3D Fourier series (4.51) of the Coulomb potential over a coordinate normal to the surface. With

$$\mathrm{d}\boldsymbol{q} = \mathrm{d}\boldsymbol{q}_\parallel \mathrm{d}q_\perp \text{ and } \boldsymbol{q}\cdot\boldsymbol{r} = \boldsymbol{q}_\parallel \cdot \boldsymbol{r}_\parallel + zq_\perp \tag{4.63}$$

we obtain from (4.51)

$$\frac{1}{r} = \frac{1}{2\pi^2}\int \mathrm{d}\boldsymbol{q}_\parallel \exp(\mathrm{i}\boldsymbol{q}_\parallel \cdot \boldsymbol{r}_\parallel)\int \mathrm{d}q_\perp \frac{\mathrm{e}^{\mathrm{i}q_\perp z}}{q_\parallel^2 + q_\perp^2}$$
$$= \frac{1}{2\pi}\int \mathrm{d}\boldsymbol{q}_\parallel \frac{1}{q_\parallel}\exp(\mathrm{i}\boldsymbol{q}_\parallel \cdot \boldsymbol{r}_\parallel - q_\parallel |z|), \tag{4.64}$$

i.e., a representation in terms of surface waves which have wave character along the surface and decay exponentially into the semi-infinite halfspace. Since the interior fields $\boldsymbol{D}_\mathrm{i}$ and $\mathcal{E}_\mathrm{i}$ are just derivatives of the $1/r$ potential (4.52) the following representations are possible

$$\boldsymbol{\mathcal{E}}_\mathrm{i}(\boldsymbol{r}, t) = \frac{1}{2\pi}\int \mathrm{d}\omega \mathrm{d}\boldsymbol{q}_\parallel \hat{\boldsymbol{\mathcal{E}}}_\mathrm{i}(\omega, \boldsymbol{q}_\parallel)\exp(-q_\parallel |z|)\exp[\mathrm{i}(\boldsymbol{q}_\parallel \cdot \boldsymbol{r}_\parallel - \omega t)] \tag{4.65a}$$

$$\dot{\boldsymbol{D}}_\mathrm{i}(\boldsymbol{r}, t) = \frac{1}{2\pi}\int \mathrm{d}\omega' \mathrm{d}\boldsymbol{q}'_\parallel (-\mathrm{i}\omega')\hat{\boldsymbol{D}}_\mathrm{i}(\omega', \boldsymbol{q}'_\parallel)\exp(-q'_\parallel |z|)\exp[\mathrm{i}(\boldsymbol{q}'_\parallel \cdot \boldsymbol{r}_\parallel - \omega' t)]. \tag{4.65b}$$

The electric field has to be a real quantity, thus we have

$$\hat{\boldsymbol{\mathcal{E}}}^*_\mathrm{i}(\omega, \boldsymbol{q}_\parallel) = \hat{\boldsymbol{\mathcal{E}}}_\mathrm{i}(-\omega, -\boldsymbol{q}_\parallel), \tag{4.66}$$

and the total energy transfer to the solid can be written in analogy to (4.43) as

$$W = \mathrm{Re}\left\{\int_{-\infty}^{+\infty}\mathrm{d}t \int_{z=0}^{\infty}\mathrm{d}\boldsymbol{r}\boldsymbol{\mathcal{E}}_\mathrm{i}(\boldsymbol{r}, t)\dot{\boldsymbol{D}}_\mathrm{i}(\boldsymbol{r}, t)\right\}. \tag{4.67}$$

In contrast to (4.43) the total energy transfer W rather than the rate $\dot{W}$ can be calculated since in surface scatering the scattering volume is finite and the time integral in (4.67) gives finite expressions. With the expansions (4.65) and the δ-function representation we obtain

$$W = 2\pi \mathrm{Re}\left\{\int_0^\infty \mathrm{d}z \int \mathrm{d}\omega \mathrm{d}\omega' \mathrm{d}\boldsymbol{q}_\parallel \mathrm{d}\boldsymbol{q}'_\parallel (-\mathrm{i}\omega')\exp(-zq_\parallel + zq'_\parallel)\right.$$
$$\left.\times\delta(\omega + \omega')\delta(\boldsymbol{q}_\parallel + \boldsymbol{q}'_\parallel)\hat{\boldsymbol{\mathcal{E}}}_\mathrm{i}(\omega, \boldsymbol{q})\hat{\boldsymbol{D}}_\mathrm{i}(\omega', \boldsymbol{q}')\right\}. \tag{4.68}$$

Relating this to the field $\hat{\boldsymbol{D}}$ of the free electron (without the solid) we get

$$W = 2\pi \mathrm{Re}\left\{\int \mathrm{d}\omega \mathrm{d}\boldsymbol{q}_\parallel \frac{\mathrm{i}\omega}{2q_\parallel}\frac{2}{(\epsilon(\omega)+1)}\frac{2\epsilon^*(\omega)}{(\epsilon^*(\omega)+1)}\frac{1}{\epsilon_0}|\hat{\boldsymbol{D}}(\omega, \boldsymbol{q}_\parallel)|^2\right\}, \tag{4.69}$$

and finally

$$W = \frac{4\pi}{\epsilon_0} \int \mathrm{d}\omega \mathrm{d}\boldsymbol{q}_\parallel \frac{\omega}{q_\parallel} |\hat{\boldsymbol{D}}(\omega, \boldsymbol{q}_\parallel)|^2 \mathrm{Im}\left\{\frac{-1}{\epsilon(\omega)+1}\right\}. \tag{4.70}$$

To calculate the expansion coefficients $\hat{\boldsymbol{D}}(\omega, \boldsymbol{q}_\parallel)$ of the field, we use (4.52) and the expansion of the Coulomb field in surface waves (4.64)

$$\begin{aligned}\boldsymbol{D}(\boldsymbol{r}, t) &= -\frac{e}{4\pi}\nabla\frac{1}{|\boldsymbol{r} - \boldsymbol{v}t|} \\ &= \frac{e}{8\pi^2}\int \mathrm{d}\boldsymbol{q}_\parallel(-\mathrm{i}\hat{\boldsymbol{e}}_\parallel, 1)\exp(\mathrm{i}\boldsymbol{q}_\parallel\cdot\boldsymbol{r}_\parallel - zq_\parallel)\exp(-\mathrm{i}\boldsymbol{q}_\parallel\cdot\boldsymbol{v}_\parallel t + q_\parallel v_\perp t).\end{aligned} \tag{4.71}$$

The last exponential function of the integrand is now Fourier-transformed with respect to time:

$$\exp(-\mathrm{i}\boldsymbol{q}_\parallel\cdot\boldsymbol{v}_\parallel t + q_\parallel v_\perp t) = \int_{-\infty}^{+\infty} \mathrm{d}\omega g(\omega)\mathrm{e}^{-\mathrm{i}\omega t} \tag{4.72}$$

to yield, with $|v_\perp| \simeq$ const and $|v_\parallel| \simeq$ const,

$$g(\omega) = \frac{1}{2\pi}\frac{2q_\parallel v_\perp}{(q_\parallel v_\perp)^2 + (\boldsymbol{q}_\parallel\cdot\boldsymbol{v}_\parallel - \omega)^2}. \tag{4.73}$$

Equation (4.73) inserted into (4.72) and finally into (4.71) gives $\hat{\boldsymbol{D}}(\omega, \boldsymbol{q}_\parallel)$, and the total energy transfer (4.70) follows as

$$\begin{aligned}W &= \frac{8\pi e^2}{(2\pi)^4\epsilon_0\hbar^2}\int \mathrm{d}(\hbar\omega)\mathrm{d}\boldsymbol{q}_\parallel\hbar\omega\frac{q_\parallel v_\perp^2}{[(q_\parallel v_\perp)^2 + (\boldsymbol{q}_\parallel\cdot\boldsymbol{v}_\parallel - \omega)^2]^2}\mathrm{Im}\left\{\frac{-1}{\epsilon(\omega)+1}\right\} \\ &= \int \mathrm{d}(\hbar\omega)\mathrm{d}\boldsymbol{q}_\parallel\hbar\omega P(\hbar\omega, \boldsymbol{q}_\parallel).\end{aligned} \tag{4.74}$$

The scattering probability $P(\hbar\omega, \boldsymbol{q}_\parallel)$ for the transfer of an energy quantum $\hbar\omega$, and a wave vector $\boldsymbol{q}_\parallel$ parallel to the surface is thus obtained as

$$P(\hbar\omega, \boldsymbol{q}_\parallel) = \frac{e^2}{2\pi^3\epsilon_0\hbar^2}\frac{q_\parallel v_\perp^2}{[(q_\parallel v_\perp)^2 + (\boldsymbol{q}_\parallel\cdot\boldsymbol{v}_\parallel - \omega)^2]^2}\mathrm{Im}\left\{\frac{-1}{\epsilon(\omega)+1}\right\}. \tag{4.75}$$

It is convenient to express the inelastic scattering cross section $P(\hbar\omega, \boldsymbol{q}_\parallel)$ or $\mathrm{d}^2S/\mathrm{d}(\hbar\omega)\mathrm{d}\boldsymbol{q}_\parallel$ as a differential cross section $\mathrm{d}^2S/\mathrm{d}(\hbar\omega)\mathrm{d}\Omega$ for scattering into a solid angle element $\mathrm{d}\Omega$. Measured spectra can then be calculated by integrating over the acceptance angle of the electron analyser Ω_{Apert}. For this purpose we use the relations (4.35–4.39) and Fig. 4.15 to express the element $\mathrm{d}\boldsymbol{q}_\parallel = \mathrm{d}q_{\parallel x}\mathrm{d}q_{\parallel y}$, in terms of a solid angle element $\mathrm{d}\Omega$:

$$\mathrm{d}\Omega = \sin\psi\mathrm{d}\psi\mathrm{d}\varphi. \tag{4.76}$$

Because of (4.32b) one has

$$\mathrm{d}\boldsymbol{k}'_{\parallel} = \mathrm{d}\boldsymbol{q}_{\parallel}, \tag{4.77}$$

and for small-angle scattering ($q_{\parallel} \ll k$) with $\psi \ll 1$ and $\varphi \simeq 0$, i.e. $\sin\varphi \simeq 0$ and $\cos\varphi \simeq 1$, one has

$$\mathrm{d}\boldsymbol{q}_{\parallel} = \mathrm{d}q_{\parallel x}\mathrm{d}q_{\parallel y} = k'^2 \cos\Theta \sin\psi \mathrm{d}\psi \mathrm{d}\varphi = k'^2 \cos\Theta \mathrm{d}\Omega. \tag{4.78}$$

For most experimental conditions the energy loss $\hbar\omega$ is small in comparison to the primary energy E, i.e.

$$\hbar\omega \ll E, \quad k'^2 \simeq k^2, \tag{4.79}$$

and because

$$E = \frac{\hbar^2 k^2}{2m} = \frac{1}{2} m v^2 = \frac{1}{2} \frac{m v_{\perp}^2}{\cos^2\Theta} \tag{4.80}$$

it follows that

$$k'^2 \cos\Theta \simeq \frac{m^2 v_{\perp}^2}{\hbar^2 \cos\Theta}. \tag{4.81}$$

From (4.79) one finally obtains

$$\mathrm{d}\boldsymbol{q}_{\parallel} = \frac{m^2 v_{\perp}^2}{\hbar^2 \cos\Theta} \mathrm{d}\Omega, \tag{4.82}$$

and for the differential scattering cross section [from (4.75)]:

$$\frac{\mathrm{d}^2 S}{\mathrm{d}(\hbar\omega)\mathrm{d}\Omega} = \frac{m^2 e^2 |R|^2}{2\pi^3 \epsilon_0 \hbar^4 \cos\Theta} \frac{v_{\perp}^4 q_{\parallel}}{[v_{\perp}^2 q_{\parallel}^2 + (\omega - \boldsymbol{v}_{\parallel} \cdot \boldsymbol{q}_{\parallel})^2]^2} \mathrm{Im}\left\{\frac{-1}{\epsilon(\omega) + 1}\right\} \tag{4.83}$$

The reflection coefficient R allows for the fact that not every primary electron is reflected from the surface. A high percentage penetrates into the solid and can be detected as a current. Apart from a Bose occupation factor $[n(\hbar\omega) + 1]$ for the excitation $\hbar\omega$ this formula (4.83) coincides with the expression derived by Mills [4.10] on the basis of a quantum mechanical treatment (Sect. 4.1), where scattering is described as originating from long-range charge density fluctuations. The scattering potential is evaluated in this calculation in terms of surface waves (4.65a) and the scattering process is described in the Born approximation.

Dielectric scattering of low-energy electrons according to (4.83) is characterized by two terms, the so-called surface loss function

$$\mathrm{Im}\left\{\frac{-1}{\epsilon(\omega)+1}\right\} = \frac{\epsilon_2(\omega)}{[\epsilon_1(\omega)+1]^2+\epsilon_2^2(\omega)}. \tag{4.84}$$

and a prefactor

$$\frac{v_\perp^4 q_\parallel}{[v_\perp^2 q_\parallel^2 + (\omega - \boldsymbol{v}_\parallel \cdot \boldsymbol{q}_\parallel)^2]^2} \tag{4.85}$$

which bears some resemblance to a resonance term.

The surface loss function (4.84) determines the essential spectral structures of a loss spectrum. Thus, as in the bulk scattering process, spectral structure is expected where $\epsilon_2(\omega) = \mathrm{Im}\{\epsilon(\omega)\}$ exhibits strong features. Since $\epsilon_2(\omega)$ also determines the optical absorption constant of a material, optical transitions of all kinds, e.g. interband excitations, excitons, phonons etc. can be observed in inelastic low-energy electron scattering. Additionally, prominent maxima in the scattering probability occur when the condition

$$\epsilon_1(\omega) \simeq -1 \tag{4.86}$$

is fulfilled in regions of small, monotonic $\epsilon_2(\omega)$. As will be shown in the next chapter, this condition (4.86) determines the frequencies of collective excitations such as surface phonons and plasmons (polaritons) of a semi-infinite dielectric halfspace. Such excitations may therefore be conveniently studied by inelastic scattering of low-energy electrons.

The resonance-type prefactor (4.85) in the scattering probability (4.83) can most readily be discussed for grazing incidence ($v_\perp \ll v_\parallel$). In this situation, strong peaks in the scattering cross section occur for

$$v_\parallel = \frac{\omega}{q_\parallel}, \tag{4.87a}$$

i.e. when the electron velocity parallel to the surface $v_\parallel$ equals the phase velocity $\omega/q_\parallel$ of the surface excitation (phonon, plasmon, etc.) that is responsible for the surface scattering process. Optimal coupling of the primary electron to the excited surface mode is obtained when the electron moves as a "surf-rider" on the phase of this surface excitation. We therefore call (4.85) the "surf-rider" term, and (4.87) the "surf-rider" condition for dielectric scattering. Using $E = \hbar^2 k^2/2m = mv^2/2$ we can express (4.87a) as

$$q_\parallel = k\frac{\hbar\omega}{2E}. \tag{4.87b}$$

For $\Theta \simeq 90°$ (grazing incidence), (4.87b) is identical to (4.42); the condition for maximum dielectric scattering cross section restricts the $q_\parallel$ transfer to values that are small in comparison with the Brillouin-zone diameter. For primary energies in the

10 eV range and losses below 100 meV, $q_\parallel$ is estimated according to (4.87) to be in the range of 10^{-2} Å^{-1}. According to Fig. 4.15a such small $q_\parallel$ transfers mean scattering into small angles around the specular direction. Dielectric scattering due to long-range charge density fluctuations can therefore be distinguished experimentally from other scattering processes by measuring the angular distribution of the scattered electrons. In the case of dielectric scattering, the distribution is sharply concentrated into a lobe of angular width about 1 to 2° around the specular direction. For conventional electron spectrometers the acceptance aperture is also in the range of 1 to 2° and therefore ideally meets the requirements for studying dielectric scattering.

Figure 4.18a illustrates the calculated, total dielectric scattering cross section [angular integration over (4.83)] versus aperture angle of the detecting spectrometer ψ_c; a circular aperture is assumed. The parameters $E = 5$ eV (primary energy),

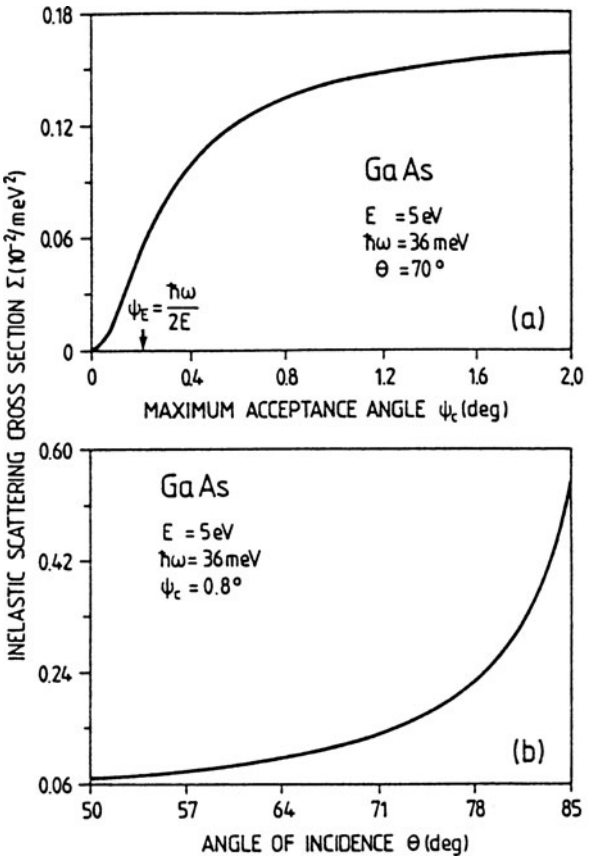

Fig. 4.18 (**a**) Total inelastic scattering cross section calculated according to dielectric theory (4.83) for scattering into an increasing angular aperture ψ_c (abscissa) around the specular direction. The parameters primary energy E, loss energy $\hbar\omega$ and angle of incidence Θ are chosen for the example of scattering from surface phonons on GaAs(110). (**b**) Total inelastic scattering cross section according to (4.83) as a function of angle of incidence. Specular detection is assumed, a primary energy of 5 eV and a loss energy of 36 meV. The integration is performed over a circular aperture (angle $\psi_c = 0.8°$) [4.15]

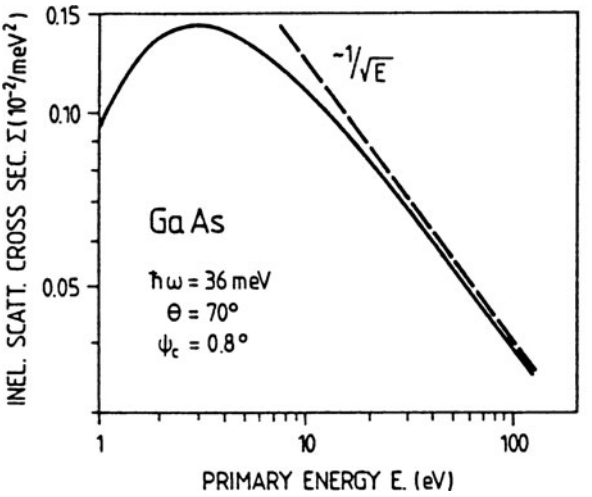

Fig. 4.19 Total inelastic scattering cross section (4.83) versus primary energy. The integration of (4.83) is performed over an aperture angle of $\psi_c = 0.8°$, the angle of incidence is $\Theta = 70°$, specular detection is considered and the loss energy is assumed to be $\hbar\omega = 36\,\text{meV}$ [4.15]

$\hbar\omega = 36\,\text{meV}$ (loss energy) and $\Theta = 70°$ are convenient for surface phonons in GaAs (Chap. 5). Figure 4.18a clearly reveals that the inelastically scattered electrons are mainly concentrated in an angle of $\psi_c \simeq 1°$. For the same scattering parameters, Fig. 4.18b displays the total scattering cross section into a circular aperture of $\psi_c = 0.8°$ versus angle of incidence Θ. The $(\cos\Theta)^{-1}$ dependence of (4.83) is clearly revealed. This $(\cos\Theta)^{-1}$ dependence stems from the time $\tau \sim (\cos\Theta)^{-1}E^{-1/2}$, during which the primary electron is moving in close proximity to the surface. The corresponding dependence of the scattering cross section on $E^{-1/2}$ is depicted in Fig. 4.19.

4.7 Dielectric Scattering on a Thin Surface Layer

The dielectric surface scattering mechanism considered so far is restricted to the interaction of electrons with a homogeneous semi-infinite halfspace. The scattering cross section (4.75, 4.83) given in Sect. 4.6 cannot therefore be used to describe inelastic scattering from quasi-2D excitations which are limited in space to a few Ångstroms below the surface. Physical examples of such excitations are transitions between electronic surface states (Chap. 6), excitations of a 2D electron gas in adsorbed metal layers or in tight accumulation layers of semiconductors (Chap. 7), surface lattice vibrations with a finite vibrational amplitude only in the topmost atomic layers, and vibrational excitations of adsorbed molecules or atoms. In principle, a quantum mechanical approach is appropriate for the description of scattering on these systems with atomic dimensions normal to the surface. In a rough approximation, however, the elementary excitations connected with such a thin surface layer are often described in a continuum model in terms of a surface dielectric function $\epsilon_s(\omega)$. This dielectric function is used to model the dielectric response of the topmost atomic layers (thickness d). The underlying bulk material is described by a bulk dielectric function $\epsilon_b(\omega)$ (Fig. 4.20). As an example one might consider a

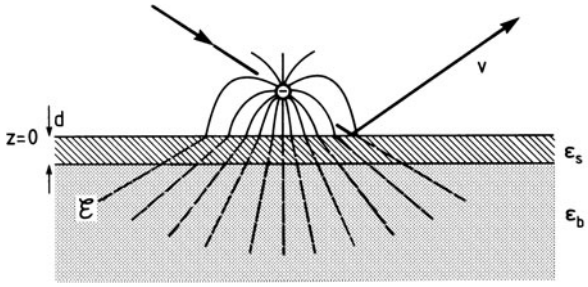

Fig. 4.20 Schematic plot of the inelastic dielectric scattering process of a lowenergy electron (velocity v) on a semi-infinite halfspace (dielectric function ϵ_b for the bulk) covered with a thin surface film (dielectric function ϵ_s). The interior electric field $\mathcal{E}_i$ of the electron outside the solid is assumed to be unchanged by the thin overlayer

thin coherent metal film with a thickness of several monolayers on a semiconductor. In this case $\epsilon_b(\omega)$ is the dielectric function of the semiconductor and $\epsilon_s(\omega)$, the dielectric function of the metal, contains as the essential part the Drude dielectric response of a free electron gas [4.16].

If we consider a spectral range of loss energies $\hbar\omega$, where substrate excitations can be neglected, the reflected electron can only transfer energy $\hbar\omega$ and wave vector $\boldsymbol{q}_\parallel$ to excitations within the surface layer. In the simplest approximation we assume the thickness of the surface layer to be so small ($q_\parallel d \ll 1$) that the field inside the bulk is not significantly perturbed by the surface layer. As in Fig. 4.17 the fields $\boldsymbol{\mathcal{E}}_b$ and $\boldsymbol{D}_b$ inside the bulk have axial symmetry around the normal through the primary electron (Fig. 4.20). At the bulk/surface-layer interface the correct boundary conditions must be fulfilled for the components parallel and normal to the surface:

$$\boldsymbol{\mathcal{E}}_b^\parallel = \boldsymbol{\mathcal{E}}_s^\parallel, \quad \boldsymbol{D}_b^\perp = \boldsymbol{D}_s^\perp. \tag{4.88}$$

Since energy is only transferred to the spatial region of the overlayer, only the "surface fields" $\boldsymbol{\mathcal{E}}_s(\boldsymbol{r}, t)$ and $\boldsymbol{D}_s(\boldsymbol{r}, t)$ within this layer have to be taken into account in determining the total energy transfer:

$$W = \mathrm{Re}\left\{\int_{-\infty}^{+\infty} \mathrm{d}t \int_{z=-d}^{0} \mathrm{d}\boldsymbol{r}\boldsymbol{\mathcal{E}}_s(\boldsymbol{r}, t)\dot{\boldsymbol{D}}_s(\boldsymbol{r}, t)\right\}. \tag{4.89}$$

Expansion of the fields in terms of surface waves (4.65), and a calculation as in (4.68) yield

$$\begin{aligned} W &= 2\pi\mathrm{Re}\left\{\int_{-d}^{z=0} \mathrm{d}z \int \mathrm{d}\omega\mathrm{d}\omega'\mathrm{d}\boldsymbol{q}_\parallel\mathrm{d}\boldsymbol{q}'_\parallel(-\mathrm{i}\omega')\hat{\mathcal{E}}_s(\omega, \boldsymbol{q}_\parallel)\hat{\boldsymbol{D}}_s(\omega', \boldsymbol{q}_\parallel)\right. \\ &\quad \left.\times\delta(\omega+\omega')\delta(\boldsymbol{q}_\parallel + \boldsymbol{q}'_\parallel)\exp[-(q_\parallel + q'_\parallel)z]\right\} \\ &= 2\pi\,\mathrm{d}\mathrm{Re}\left\{\int \mathrm{d}\omega\mathrm{d}\boldsymbol{q}_\parallel \mathrm{i}\omega\hat{\mathcal{E}}_s(\omega, \boldsymbol{q}_\parallel)\hat{\boldsymbol{D}}_s^*(\omega, \boldsymbol{q}_\parallel)\right\}. \end{aligned} \tag{4.90}$$

In order to fullfill the conditions (4.88) we decompose the fields into components normal and parallel to the surface, i.e.,

$$\hat{\boldsymbol{\mathcal{E}}}_\mathrm{s} = (\hat{\mathcal{E}}_\mathrm{s}^{\parallel}, \hat{\mathcal{E}}_\mathrm{s}^{\perp}), \quad \hat{\boldsymbol{D}}_\mathrm{s} = \epsilon_\mathrm{s}\epsilon_0(\hat{\mathcal{E}}_\mathrm{s}^{\parallel}, \hat{\mathcal{E}}_\mathrm{s}^{\perp}). \tag{4.91}$$

Equation (4.90) is then evaluated for each field component separately:

$$W = 2\pi \mathrm{d}\mathrm{Re}\left\{\int \mathrm{d}\omega \mathrm{d}\boldsymbol{q}_\parallel \mathrm{i}\omega \left(\hat{\boldsymbol{\mathcal{E}}}_\mathrm{s}^{\parallel}\hat{\boldsymbol{\mathcal{E}}}_\mathrm{s}^{\parallel^*}\epsilon_\mathrm{s}^*\epsilon_0 + \frac{1}{\epsilon_0\epsilon_\mathrm{s}}\hat{\boldsymbol{D}}_\mathrm{s}^{\perp}\hat{\boldsymbol{D}}_\mathrm{s}^{\perp^*}\right)\right\}. \tag{4.92}$$

Using the boundary conditions (4.88) one can relate this to the bulk fields

$$W = 2\pi \mathrm{d}\mathrm{Re}\left\{\int \mathrm{d}\omega \mathrm{d}\boldsymbol{d}_\parallel \omega \left(\epsilon_0 \mathrm{Im}\{\epsilon_\mathrm{s}|\hat{\boldsymbol{\mathcal{E}}}_\mathrm{b}^{\parallel}|^2\} + \frac{1}{\epsilon_0}\mathrm{Im}\{-\epsilon_\mathrm{s}^{-1}|\hat{\boldsymbol{D}}_\mathrm{b}^{\perp}|^2\}\right)\right\} \tag{4.93}$$

and finally insertion of the shielding factor (4.62) for a semi-infinite halfspace yields the energy transfer with respect to the "external" Coulomb field of the primary electron:

$$\begin{aligned} W = \frac{2\pi \mathrm{d}}{\epsilon_0}\mathrm{Re}\Bigg\{\int \mathrm{d}\omega \mathrm{d}\boldsymbol{q}_\parallel \omega \Bigg(&\frac{4}{|\epsilon_\mathrm{b}+1|^2}\mathrm{Im}\{\epsilon_\mathrm{s}|\hat{\boldsymbol{D}}^{\parallel}|^2\} \\ &+\frac{4|\epsilon_\mathrm{b}|^2}{|\epsilon_\mathrm{b}+1|^2}\mathrm{Im}\{-\epsilon_\mathrm{s}^{-1}|\hat{\boldsymbol{D}}^{\perp}|^2\}\Bigg)\Bigg\}. \end{aligned} \tag{4.94}$$

Using the "Fourier transforms" (4.71–4.73) one obtains

$$|\hat{\boldsymbol{D}}^{\parallel}|^2 = |\hat{\boldsymbol{D}}^{\perp}|^2 = \frac{e^2}{(2\pi)^4}\frac{q_\parallel^2 v_\perp^2}{[(q_\parallel v_\perp)^2 + (\boldsymbol{q}_\parallel \cdot \boldsymbol{v}_\parallel - \omega)^2]^2}. \tag{4.95}$$

With the definition (4.74) of the probability $P(\hbar\omega, \boldsymbol{q}_\parallel)$ for scattering from an excitation $(\hbar\omega, \boldsymbol{q}_\parallel)$ it follows that

$$\begin{aligned} P(\hbar\omega, \boldsymbol{q}_\parallel) = &\frac{e^2 \mathrm{d}}{2\pi^3\epsilon_0\hbar^2}\frac{q_\parallel^2 v_\perp^2}{[(q_\parallel v_\perp)^2 + (\boldsymbol{q}_\parallel \cdot \boldsymbol{v}_\parallel - \omega)^2]^2} \\ &\times\left(\frac{1}{|\epsilon_\mathrm{b}+1|^2}\mathrm{Im}\{\epsilon_\mathrm{s}\} + \frac{|\epsilon_\mathrm{b}|^2}{|\epsilon_\mathrm{b}+1|^2}\mathrm{Im}\{-1/\epsilon_\mathrm{s}\}\right). \end{aligned} \tag{4.96}$$

Referring this probability to the scattering into an element of solid angle, a result similar to (4.83) is obtained. As is expected qualitatively, the inelastic scattering cross section (4.96) for low-energy electrons in a thin dielectric slab on top of the bulk substrate is proportional to the thickness d of this slab. An important result is obtained by comparing the two additive terms in (4.49 and 4.96), respectively: the second term related to electric field components $\hat{\boldsymbol{D}}^{\perp}$ normal to the surface

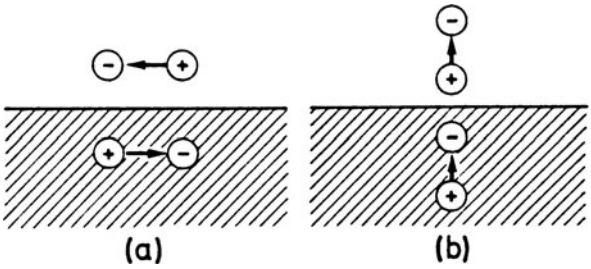

Fig. 4.21a,b Qualitative explanation of the orientation selection rule for dipole surface scattering: the image dipole within the substrate (shaded) partially compensates the effect of the adsorbed dipole for parallel orientation (**a**) but enhances the effect of dipoles with a normal orientation (**b**)

is a factor $|\epsilon_b|^2$ larger in magnitude than the first term. For metal substrates and even on semiconductor surfaces (Si, Ge, GaAs, etc.) where $|\epsilon_b|^2$ exceeds 100, the second term originating from field components normal to the surface dominates the loss spectrum. The main structure in the loss spectrum is therefore determined by $\mathrm{Im}\{-1/\epsilon_s\}$, the bulk loss function of the thin surface layer, and because of the field direction normal to the surface ($\hat{\boldsymbol{D}}^{\perp}$), only those dipoles within this layer that are oriented normal to the interface contribute to the spectrum. This is the so-called *orientation selection rule*. It states that in dielectric theory the excitations (vibrations of adsorbed molecules, electronic surface state transitions, etc.) that give rise to significant loss structures are those whose dynamic dipole moment is oriented normal to the surface. A qualitative argument for this selection rule can be derived from Fig. 4.21. Scattering by dynamic dipole moments on top of a metal or semiconductor substrate is considered. In addition to the dipole moments within the overlayer, image dipoles in the substrate itself contribute to the total scattering cross section. For a dipole orientation parallel to the surface (a), the image dipole has the reverse orientation and therefore partially compensates the effect of the overlayer dipole. For a dipole orientation normal to the surface the image dipole has the same direction (b) and enhances the overlayer effect. It should be emphasized that this orientation selection rule has been derived, and is only valid, within the framework of dielectric theory.

The present derivation of the scattering cross section (4.96) is an approximation valid in the limit $q_{\parallel}d \ll 1$. Equation (4.96) is valid for layer thicknesses d which are small in comparison to the inverse wave-vector transfer $q_{\parallel}$. The overlayer must not significantly perturb the Coulomb field inside the bulk substrate. A more general formula without any limitation on d has been derived by Ibach and Mills [4.10] by taking into account the correct boundary conditions both for the vacuum and for the overlayer–substrate interface. According to this derivation, the scattering cross section for surface scattering in an overlayer of thickness d is given by the formulae for the semi-infinite halfspace, (4.75, 4.83). But the surface loss function (4.84) has to be modified by an effective dielectric function $\tilde{\epsilon}(\omega)$, which contains both the dielectric function $\epsilon_b(\omega)$ of the bulk substrate and of the overlayer $\epsilon_s(\omega)$.

The surface loss function, which has to be inserted into (4.75) or (4.83) for the continuous overlayer model, is

$$\mathrm{Im}\left\{\frac{-1}{\tilde{\epsilon}(\boldsymbol{q}_\parallel,\omega)+1}\right\}, \tag{4.97}$$

with an effective dielectric function

$$\tilde{\epsilon}(\boldsymbol{q}_\parallel,\omega)=\epsilon_\mathrm{s}(\omega)\frac{1+\Delta(\omega)\exp(-2q_\parallel d)}{1-\Delta(\omega)\exp(-2q_\parallel d)}, \tag{4.98a}$$

where

$$\Delta(\omega)=\frac{\epsilon_\mathrm{b}(\omega)-\epsilon_\mathrm{s}(\omega)}{\epsilon_\mathrm{b}(\omega)+\epsilon_\mathrm{s}(\omega)}. \tag{4.98b}$$

Although both ϵ_b and ϵ_s are assumed to be independent of $q_\parallel$, the effective dielectric function $\tilde{\epsilon}(\boldsymbol{q}_\parallel,\omega)$ becomes a function of the wave-vector transfer $q_\parallel$; this is a natural consequence of the fact that the "information depth" of the scattering experiment is dependent on $q_\parallel(\propto 1/q_\parallel)$ and therefore the relation between $1/q_\parallel$) and the layer thickness d determines the relative contributions of ϵ_b and ϵ_s to the total scattering cross section. For the limiting case $d\to 0$, (4.98a) approaches the dielectric function ϵ_b of the semi-infinite halfspace without overlayer. For $d\to\infty$ the scattering cross section for a semi-infinite half space with dielectric function ϵ_s is obtained.

A further extension of this formalism to dielectric scattering from a multi-layer structure on top of a semi-infinite solid has been given by Lambin et al. [4.17]. The model system consists of n layers (numbered by i) each described by a complex dielectric function $\epsilon_i(\omega)$ and thickness d_i. The loss function (4.97) is then calculated by using an effective dielectric function

$$\tilde{\epsilon}(\boldsymbol{q},\omega)=a_1(\omega)-\cfrac{b_1^2(\omega)}{a_1(\omega)+a_2(\omega)-\cfrac{b_2^2(\omega)}{a_2(\omega)+a_3(\omega)-\cfrac{b_3^2(\omega)}{a_3(\omega)+a_4(\omega)-\ldots}}} \tag{4.98c}$$

instead of (4.98a).

The coefficients $a_i(\omega)$ and $b_i(\omega)$ introduce a wave-vector dependence through the relations

$$a_i(\omega)=\epsilon_i(\omega)/\tanh(q_\parallel \mathrm{d}_i),\quad b_i(\omega)=\epsilon_i(\omega)/\sinh(q_\parallel \mathrm{d}_i). \tag{4.98d}$$

For a fixed number of layers n on top of a semi-infinite substrate, the series (4.98c) is terminated by the condition $b_{n+1}=0$. This multilayer formalism can also be used to approximate any spatially varying dielectric property $[\epsilon(\omega,z)]$ near the surface.

4.8 Some Experimental Examples of Inelastic Scattering of Low-Energy Electrons at Surfaces

In a surface scattering experiment with low-energy electrons using the reflection geometry, it is nevertheless possible to detect bulk excitations. This is because the surface loss function (4.84) for a semi-infinite halfspace contains the imaginary part $\epsilon_2(\omega)$ of the bulk dielectric function in the numerator. An experimental example is illustrated in Fig. 4.22. The electron energy loss spectrum was recorded by means of a high-resolution spectrometer (Panels II, IX) with a primary energy of 21 eV on a clean InSb(110) surface, which had been prepared by cleavage in UHV. The broad loss structure with a threshold slightly below 200 meV is due to bulk interband transitions across the direct gap ($E_g = 180$ meV at 300 K) of InSb. The loss spectrum reflects the frequency dependence of the optical absorption constant of InSb [4.18].

Figure 4.23 displays a series of double-differentiated electron energy loss spectra, which have been measured by means of a Cylindrical Mirror Analyzer (CMA) on clean cleaved InSb(110) (a) after deposition of Sn on InSb(100) (b) and InSb(110) (c and d), and on a clean polycrystalline β-Sn foil (e) [4.20]. In these double-differentiated curves the negative second derivative of the loss spectrum is recorded, such that positive peak maxima correspond to peak maxima in the undifferentiated spectrum and thus indicate loss peak positions.

The relatively high primary energies of between 70 and 100 eV give rise to both bulk and surface scattering, even though the scattering geometry is that of a reflection experiment. However, the exact relative contributions of surface and bulk scattering are not known, i.e. it is not clear to what extent the peak positions are determined by the surface (4.84) or bulk (4.60) loss function. This uncertainty is usually of minor importance since the energy resolution in these spectra is not better than 800 meV because of lack of monochromaticity of the primary beam. The prominent peaks near 14 eV in all spectra are due to the excitation of the bulk plasmon, i.e. they arise from a singularity in $\mathrm{Im}\{-1/\epsilon\}$. Because of the similarity in the atomic

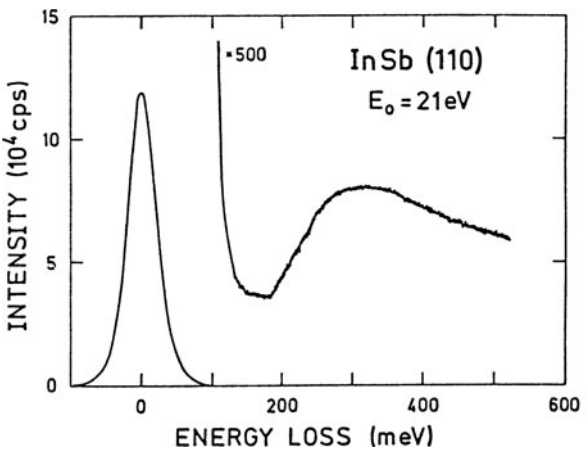

Fig. 4.22 Low-energy electron loss spectrum measured for specular reflection with a primary energy E_0 of 21 eV on a clean cleaved InSb(110) surface. Because of intensity requirements, the energy resolution is not sufficient to resolve surface phonon excitations. The loss feature with an onset near 180 meV is due to electron-hole pair excitations across the forbidden gap [4.18]

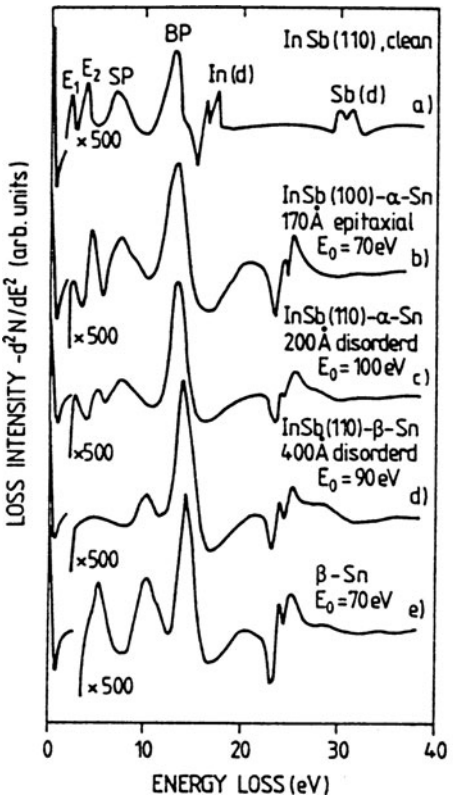

Fig. 4.23 Double differentiated electron energy loss spectra measured by means of a CMA (energy resolution $\approx$ 0.8 eV, primary energy E_0) on various InSb surfaces, clean and with Sn overlayers prepared in UHV. (a) loss spectrum of the clean cleaved InSb(110) surface; apart from the bulk (BP) and surface plasmon (SP) losses, two losses due to bulk electronic transitions (E_1, E_2) and the d core-level transitions (spin-orbit split) of In and Sb are seen. (b) Loss spectrum of an InSb(100) surface cleaned by ion bombardment and annealing, after deposition of a 170-Å thick Sn overlayer; deposition at 300 K leads to epitaxial growth of α-Sn. (c) Loss spectrum of UHV cleaved InSb(110) surface after deposition of a 200-Å thick Sn overlayer; deposition at 300 K leads to a disordered α-Sn film. (d) Loss spectrum of a UHV cleaved InSb(110) surface after deposition of a 400-Å thick Sn overlayer; deposition at 300 K causes the thick Sn overlayer to be in its metallic β-modification, at least in the topmost region. (e) Loss spectrum of a polycrystalline metallic β-Sn sample, cleaned by ion bombardment and annealing [4.19]

numbers of InSb and Sn, the bulk plasmon energies are almost identical, reflecting the very similar valence electron densities. On InSb(110) two double peaks occur near 17 and 30 eV. Comparison with core-level photoemission data allows one to interpret these structures in terms of excitations from the In and Sb d-core levels into the conduction band of the semiconductor. The doublet structure is due to spin-orbit splitting of the core levels. On the Sn-covered surfaces these structures are not observed due to shielding by the overlayer. Instead, the spin-orbit split Sn d-level excitation appears near 24 eV. The peaks near 7 eV in curves (a–c) and near

10 eV in (d) and (e) are due to the surface plasmon excitations on InSb(110), on the Sn overlayers and on polycrystalline bulk β-Sn, respectively. The two structures E_1 and E_2 below 5 eV loss energy must be interpreted in terms of bulk interband transitions, which are known from optical data for InSb and tetrahedrally bonded (semiconducting) α-Sn. The spectra in Fig. 4.23 are good examples of the application of EELS (Panel IX: Chap. 4) as a fingerprinting technique for identifying the nature of a thin overlayer. Comparison of curves (d) and (a) shows that thick layers of Sn deposited on InSb(110) at 300 K are in the metallic β-modification. The presence of the two interband transitions E_1 and E_2 is indicative of a tetrahedrally bonded semiconductor. Thus in curves (b) and (c) the Sn overlayer consists essentially of tetrahedrally bonded Sn atoms. On InSb(100) (curve b) additional LEED investigations reveal a crystalline epitaxial Sn layer, i.e., the α-modification of Sn, usually unstable at room temperature, could be epitaxially grown on the InSb(100) substrates. On cleaved InSb(110) the Sn overlayer did not give rise to a LEED diffraction pattern and therefore the Sn must be amorphous or polycrystalline.

Figure 4.24 exhibits electron energy loss spectra that have been measured by means of a hemispherical electron energy analyzer without monochromatization of the primary electron beam on a clean Cu(110) surface and after exposure (at 90 K) to nitrous oxide N_2O [4.20]. The energy resolution is $\approx$ 300 meV, which is sufficient to study relatively broad electronic excitations in the energy range of several electron volts. The two loss features on the clean surface near 4 and 7 eV arise from singularities of the bulk and/or surface loss functions $\mathrm{Im}\{-1/\epsilon\}$ and $\mathrm{Im}\{-1/(\epsilon+1)\}$. They are due to bulk and surface plasmon excitations of the free electron gas coupled to d-band transitions.

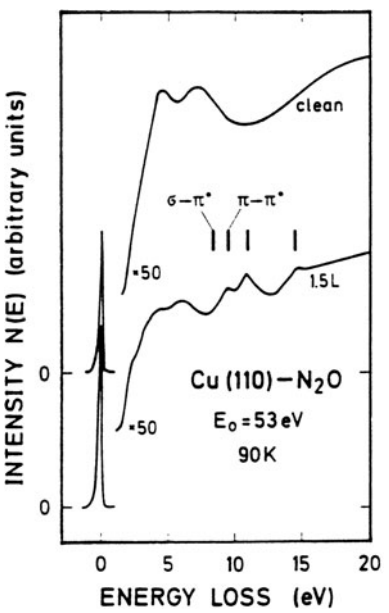

Fig. 4.24 Electron energy loss spectra measured by a hemispherical energy analyser with an "unmonochromatised" primary electron beam ($E_0 = 53$ eV, energy width ≈ 0.3 eV) on a clean Cu(110) surface and after exposure to 1.5 L of N_2O at 90 K. The electronic transitions of gaseous N_2O are marked for comparison by bars [4.20]

After adsorption of N_2O the substrate losses appear to have changed their intensity and position, and three new loss features characteristic of the adsorbed molecules emerge near 9.6, 11 and 14.5 eV. As is seen from the bars above the spectrum, these losses correspond exactly to three electronic excitations of gaseous N_2O. The low-energy loss at 8.5 eV for the gas phase is not seen in the adsorbate spectrum. Nevertheless, the loss pattern of the adsorbed N_2O strongly suggests that N_2O is adsorbed on Cu(110) at 90 K as an undissociated molecule. Since the present case obviously corresponds to surface scattering on a thin adsorbate overlayer, the orientation selection rule for dipole scattering (Sect. 4.7) can be applied. Accordingly, the absence of the 8.5 eV loss in the adsorbate spectrum is attributed to the particular orientation of the corresponding dynamic electronic dipole moment with respect to the surface. N_2O is a linear molecule with an atomic structure $N \equiv N = 0$; the excitations at 8.5 and 9.6 eV are interpreted on the basis of molecular orbital calculations in terms of $\sigma \rightarrow \pi^*$ and $\pi \rightarrow \pi^*$ transitions. The $\sigma \rightarrow \pi^*$ transition has a dipole moment perpendicular to the molecular axis, whereas the dipole moment of the $\pi \rightarrow \pi^*$ transition is oriented parallel to the axis as is easily seen from a qualitative consideration of the dipole transition matrix element (z is the molecular axis)

$$e \int \psi^*_{\pi^*} z \psi_\pi \, d\boldsymbol{r}. \tag{4.99}$$

Since the $\pi \rightarrow \pi^*$ transition is clearly seen in the spectrum, an orientation of the adsorbed molecules with their axis parallel to the surface can be ruled out. On the other hand, the lack of the $\sigma \rightarrow \pi^*$ loss with a dipole moment normal to the molecular axis is consistent with an orientation of the N_2O molecules normal to the substrate surface.

This example of inelastic electron scattering from a molecular adsorbate overlayer shows how the orientation selection rule for dipoles can yield useful information about the orientation of adsorbed molecules. This selection rule is equally interesting when High-Resolution Electron Energy Loss Spectroscopy (HREELS) is used to study vibrations of adsorbed molecules [4.10]. Figure 4.25 shows the example of HREELS spectra for Ni(111) and Pt(111) surfaces [4.21], each covered with half a monolayer of CO, which orders into a c(4×2) overlayer (as deduced from LEED). On the Ni surface the vibrational spectrum shows only two characteristic vibrational bands. The band at a wave number of 1900 cm^{-1} is due to the C–O stretch vibration, since the corresponding gas phase excitation has a wave number of 2140 cm^{-1}. The low-energy structure at 400 cm^{-1} must be interpreted in terms of a vibration of the whole molecule against the substrate surface. These substrate-molecule vibrations usually have energies below 1000 cm^{-1} or 100 meV. On Pt(111) the double structures with bands at 2100, 1850 cm^{-1} and 470, 380 cm^{-1} clearly indicate two types of adsorbed CO molecules, in contrast to the Ni case. Vibration frequencies due to C–O bending modes are not observed on either Ni or Pt. Applying the orientation selection rule one can infer that the CO has its molecular axis normal to the surface. In this orientation the stretching modes have a dynamic dipole

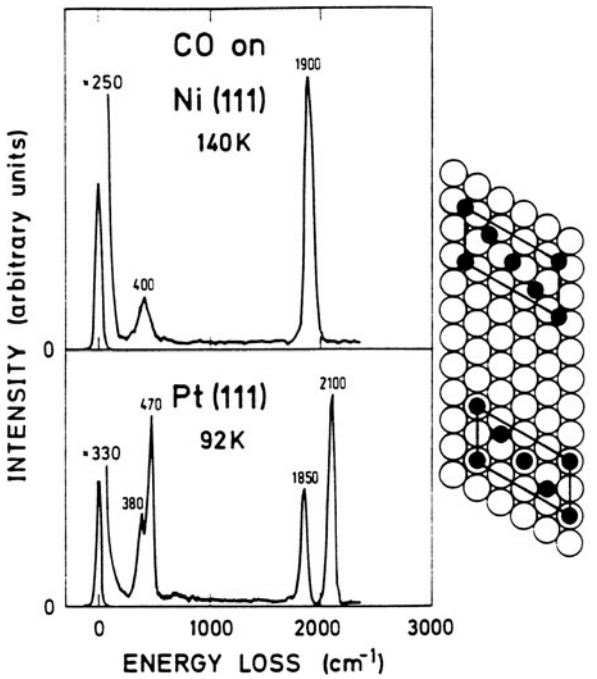

Fig. 4.25 Electron energy loss spectra (HREELS) of the Ni(111) and Pt(111) surfaces, each covered with half a monolayer of CO which orders into a c(4 × 2) overlayer. On the Ni surface the vibration spectrum indicates only a single CO species in a site of high symmetry. The only possibility for positioning the two-dimensional CO lattice on the surface consistent with the single type of adsorption site is to place all CO molecules into two-fold bridges. By similar reasoning, half the CO molecules must occupy on-top sites on the Pt(111) surface. The qualitative structure analysis (depicted on the right-hand side) is thus obtained by combining LEED and HREELS results [4.21]

moment normal to the surface, but for the bending modes the moment is parallel to the surface so that this vibration should not be observed if dipole scattering prevails, i.e. dielectric theory for a thin overlayer (Sect. 4.7).

A large number of adsorption systems on clean metal surfaces have now been studied by means of HREELS. Using the orientation selection rule within the framework of dielectric theory this technique has proven to be extremely powerful in determining the chemical nature, the orientation and sometimes the adsorption site of relatively complex adsorbed organic molecules on transition metals. It should be emphasized, however, that there are also adsorption systems, e.g. atomic hydrogen on W [4.22], where impact scattering rather than dipole scattering from adsorbate vibrations has been observed. In these cases, of course, the dipole selection rule cannot be applied.

HREELS on adsorbate vibrations can also give interesting information about adsorption sites on compound semiconductor surfaces. Figure 4.26 illustrates an example of a spectrum measured for a cleaved GaAs(110) surface which was exposed to atomic hydrogen (H) up to saturation [4.23]. The energetically

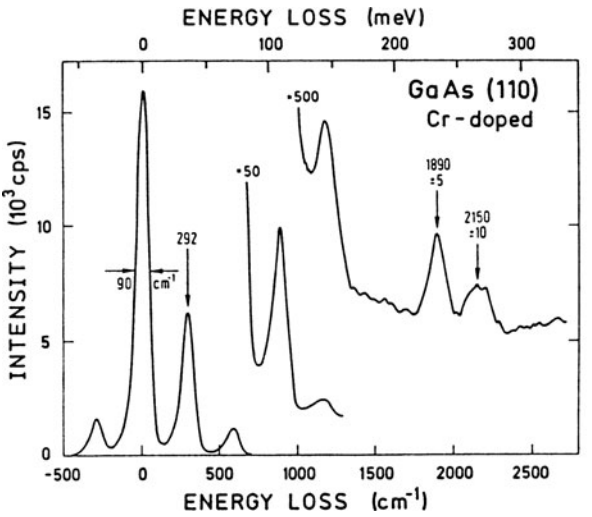

Fig. 4.26 Electron energy loss spectrum (HREELS) of a cleaved GaAs(110) surface covered with a saturated atomic hydrogen adsorbate layer. Beside multiple (energetically equidistant) loss and (one) gain peaks due to Fuchs-Kliewer surface phonons (polaritons), two characteristic adsorbate losses are observed arising from Ga–H and As–H vibrations at 1890 and 2150 cm^{-1}, respectively [4.23]

equidistant loss (and one gain) peaks below 1500 cm^{-1} are due to multiple excitations of the Fuchs-Kliewer surface phonon (polariton) of the GaAs substrate. This kind of loss process is always observed on surfaces of InfraRed (IR) active semiconductors (Sect. 5.5). The scattering process for these excitations must be described as dielectric scattering from a semi-infinite half space. On the other hand, the two losses at 1890 and 2150 cm^{-1} do not occur on the clean cleaved GaAs(110) surface. They are therefore due to scattering within the thin H adsorbate overlayer. Comparison with IR data (AsH_3 and Ga–H complexes) shows that the 1890 cm^{-1} loss arises from a Ga–H, and the 2150 cm^{-1} peak from a As–H stretch vibration. Atomic H therefore adsorbs both on Ga and on As surface atoms. On IR-active materials with strong phonon losses similar to those seen in Fig. 4.26, combined losses of these surface phonons and of adsorbate vibrations have also been observed [4.24]. One must therefore be careful when interpreting vibrational loss spectra of adsorbates on IR-active semiconductors.

4.9 The Classical Limit of Particle Scattering

So far, the scattering of particles, in particular of electrons, at surfaces has been described in terms of wave propagation. This picture takes into account the correct wave nature of matter, as expressed by de Broglie's relation. The underlying reason why particle scattering must be treated in this manner is that an electron of primary energy of about 150 eV has a de Broglie wave-length of 1 Å. This is just the order of magnitude of interatomic distances. If the scattering potentials vary over distances comparable with the wavelength of the scattered particles, the complete wave mechanical formalism has to be applied, as was done above.

Let us now consider the extreme case of high energy atom or ion scattering which is also frequently used in the investigation of surfaces, thin overlayers and material analysis in general [4.25]. According to de Broglie's relation ($v = h/m\lambda$, $E = (1/2)mv^2$), He atoms with a kinetic energy of 2 MeV have a wavelength of 10^{-4} Å. For these particles the scattering potential at a solid surface varies on a scale which is large compared to their wavelength.

Let us compare the wave-mechanical and the classical (Newtonian) treatment of the motion of such a high-energy particle (Fig. 4.27a,b). In wave mechanics, the wave function of a particle (mass m) moving in a potential $V(z)$ extended over a small region L is

$$\psi \approx \exp\left[\frac{-\mathrm{i}}{\hbar}\left(\frac{p^2}{2m} + V\right)t + \frac{\mathrm{i}}{\hbar}\boldsymbol{p}\cdot\boldsymbol{x}\right]. \tag{4.100}$$

In the regions where V vanishes (4.100) becomes the plane wave of a freely moving particle. In the region L, where $V \neq 0$ the lines of constant phase, and thus also the node lines are given by

$$p^2/2m + V = \text{const.} \tag{4.101}$$

To find the change in angle of a wave node line after crossing the region L (Fig. 4.27b) we have to consider paths (a) and (b). Corresponding to the difference $\Delta V = (\partial V/\partial z)A$ in potential there is a difference Δp in momentum according to (4.101) of

$$\Delta(p^2/2m) = p\Delta p/m = -\Delta V. \tag{4.102}$$

The wave number $p/\hbar$ is therefore different along the two paths, i.e. the phase is advancing at a different rate. The amount by which the phase φ on path (b) is "ahead" of that on path a follows as

$$\Delta\varphi = L\Delta k = \frac{L\Delta p}{\hbar} = -\frac{m}{p\hbar}L\Delta V. \tag{4.103}$$

A phase advance $\Delta\varphi$ corresponds to wave nodes advanced by a distance

$$\Delta x = \frac{\lambda}{2\pi}\Delta\varphi = \frac{\hbar}{p}\Delta\varphi, \tag{4.104}$$

or to an angle between incoming and outgoing wave of

$$\delta\theta = \frac{\Delta x}{A} = -\frac{m}{p^2}\frac{L}{A}\Delta V. \tag{4.105}$$

This derivation is valid under the condition that $V(z)$ and $\partial V/\partial z$ vary slowly in comparison with the wavelength $\lambda = h/p$ of the particle. Classically one can

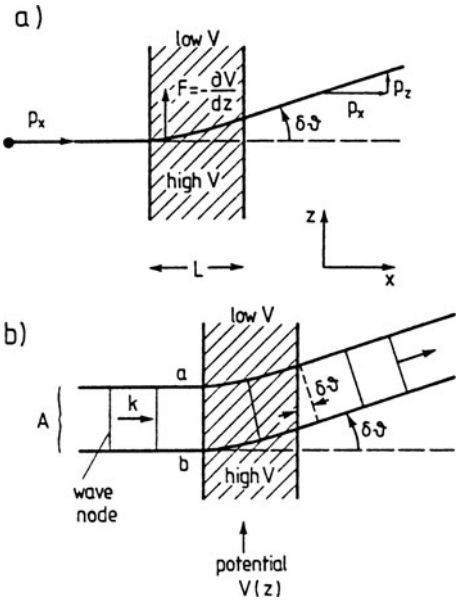

Fig. 4.27 Schematic representation of (**a**) the trajectory of a classical particle (momentum p_x) traversing a region (shaded) with changing potential $V(z)$. The force acting on the particle is $F = -\partial V/\partial z$. (**b**) A quantum mechanical plane wave (wave vector k) traversing a region with changing potential $V(z)$. When the potential $V(z)$ (and also $\partial V/\partial z$) varies slowly in comparison with the wavelength $\lambda = h/p$ of the particle, both descriptions yield the same angular deflection $\delta\theta$

calculate the angular deflection $\delta\theta$ produced by the potential region L as follows (with p as initial momentum):

$$\delta\theta = \frac{p_z}{p} = \frac{FL}{pv} \tag{4.106}$$

since L/v is the time during which the force $F = -\partial V/\partial z$ acts on the particle. One thus gets

$$\delta\theta = -\frac{L}{pv}\frac{\partial V}{\partial z} \approx -\frac{m}{p^2}L\frac{\Delta V}{A}. \tag{4.107}$$

For the case of a potential that varies slowly in comparison to the wavelength of the particle, classical dynamics thus gives the results of wave mechanics. Interference phenomena characteristic of wave propagation can be neglected. For photons this corresponds to the limit of geometrical optics. The scattering of high-energy atoms and ions on surfaces can therefore be treated according to the kinematics of classical particle collisions. A local picture emerges for the scattering process; this is in contrast to the wave-mechanical treatment in Sect. 4.1. In the kinematic theory of wave scattering a local interaction with a single surface atom is not sufficient; the whole neighbourhood, i.e. the 2D translational symmetry of the surface enters the description of the scattering process. On the other hand, in the classical limit, the interaction of the scattered particle with the surface reduces essentially to a two-body interaction of the particle with a surface target atom. This is even true

for cascade processes, which may be built up from a sequence of separate two-body collisions.

The essential measured quantity is again the differential cross section $\mathrm{d}S/\mathrm{d}\Omega$. For a beam of particles incident on a number N_s of surface target atoms this is defined as

$$\frac{\text{Number of particles scattered into } \mathrm{d}\Omega}{\text{Total number of incident particles}} = \frac{\mathrm{d}S(\theta)}{\mathrm{d}\Omega}\mathrm{d}\Omega N_\mathrm{s}. \tag{4.108}$$

The average differential cross section $S(\theta)$ for scattering into a solid angle Ω in the direction θ is given by (Fig. 4.28a)

$$S(\theta) = \frac{1}{\Omega}\int_\Omega \frac{\mathrm{d}S}{\mathrm{d}\Omega}\mathrm{d}\Omega. \tag{4.109}$$

For the geometry in Fig. 4.28a the total number of detected particles in the solid angle Ω, i.e. the yield Y is

$$Y = S(\theta)\Omega N_\mathrm{i} N_\mathrm{s} \tag{4.110}$$

where N_i is the number of incident particles (time integral over incident current).

The scattering cross section can be calculated from the force that acts during the collision between the projectile and the target atom (Fig. 4.28b). It is useful to introduce the so-called impact parameter b as the perpendicular distance between the incident particle trajectory and the parallel line through the target atom. Particles with impact parameters between b and $b+\mathrm{d}b$ are scattered into angles θ and $\theta+\mathrm{d}\theta$. For central forces there must be rotational symmetry around the beam axis. One therefore gets

$$2\pi b\mathrm{d}b = -\frac{\mathrm{d}S}{\mathrm{d}\Omega}2\pi\sin\theta\mathrm{d}\theta, \tag{4.111a}$$

or

$$\frac{\mathrm{d}S}{\mathrm{d}\Omega} = -\frac{b}{\sin\theta}\frac{\mathrm{d}b}{\mathrm{d}\theta} \tag{4.111b}$$

which relate the scattering cross section to the impact parameter. The minus sign indicates that an increase in the impact parameter results in less force on the particle, i.e. in a decrease in the scattering angle. A convenient way to calculate scattering cross sections is to determine from (4.111b) the so-called *deflection function* $\theta(b)$ using the interaction force between projectile and target.

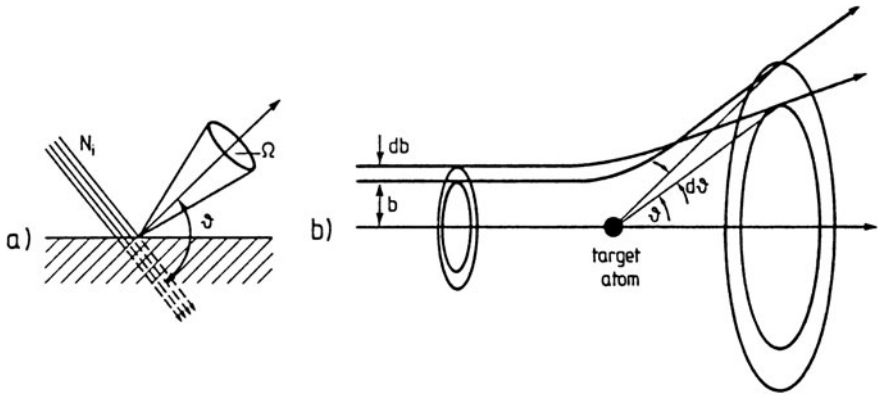

Fig. 4.28 a,b The scattering of classical particles: (**a**) Surface scattering of a primary beam of N_i particles. Some of the particles are scattered into a solid angle Ω around a direction θ counted from the direction of incidence. (**b**) Scattering of a classical particle by a heavy target particle (atom) at rest. The motion of the incoming projectile is described in terms of its impact parameter b. The scattering angle θ depends on the impact parameter b. The deflection function $\theta(b)$, which determines the scattering cross section, depends on details of the force acting between target and projectile. Projectiles arriving with impact parameters between b and $b + \mathrm{d}b$ are scattered into directions between θ and $\theta + \mathrm{d}b$

4.10 Conservation Laws for Atomic Collisions: Chemical Surface Analysis

In a collision of two classical particles, energy and momentum must be conserved. These conservation laws alone allow important conclusions concerning energy transfer from projectile to target atom without going into details of the interatomic interaction. For this purpose we assume a collision between an incident particle (mass m_1, velocity $\boldsymbol{v}_1$, kinetic energy E_1) and a second particle (mass m_2) initially at rest. After the collision the particles have velocities and energies v_1', v_2' and E_1', E_2', respectively (Fig. 4.29a).

With the scattering and recoil angles θ and φ energy and momentum conservation requires

$$\frac{1}{2}m_1 v_1^2 = \frac{1}{2}m_1 v_1'^2 + \frac{1}{2}m_2 v_2'^2, \tag{4.112}$$

$$m_1 v_1 = m_1 v_1' \cos\theta + m_2 v_2' \cos\varphi, \tag{4.113a}$$

$$0 = m_1 v_1' \sin\theta + m_2 v_2' \sin\varphi. \tag{4.113b}$$

Equations (4.113a,b) describe momentum conservation along the directions parallel and normal to the direction of incidence ($\| \boldsymbol{v}_1$), respectively. After eliminating first

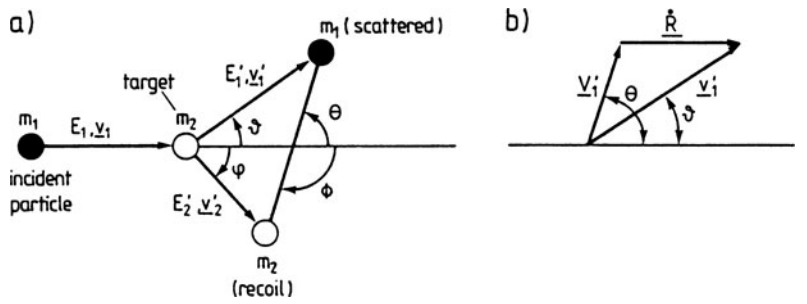

Fig. 4.29 a,b Explanation of the mathematical symbols describing a classical two particle scattering event. (**a**) A particle with mass m_1 is scattered on a target with mass m_2 at rest, which receives a kinetic energy E_2' and a velocity $\boldsymbol{v}_2'$ after the collision. θ and φ are the scattering and recoil angles in the laboratory system respectively. Θ and Φ are scattering and recoil angles in the center of mass (CM) frame, respectively. (**b**) description of the same two particle collision in the center of mass frame: $\dot{\boldsymbol{R}}$ is the velocity of the center of mass (CM); $\boldsymbol{v}_1'$ and $\boldsymbol{V}_1'$ the velocities of the scattered projectile after the collision in the laboratory and in the CM frame, respectively; θ and Θ are the scattering angles in the laboratory and in the CM frame

φ and then v_2' one finds the ratio of the particle velocities of the projectile after and before collision:

$$\frac{v_1'}{v_1} = \pm\frac{(m_2^2 - m_1^2\sin^2\theta)^{1/2} + m_1\cos\theta}{m_1 + m_2} \tag{4.114}$$

The plus sign holds for $m_1 < m_2$. For this condition $m_1 < m_2$ the ratio of the projectile energies after and before the collision (kinematic factor) follows as

$$\frac{E_1'}{E_1} = \left(\frac{(m_2^2 - m_1^2\sin\theta)^{1/2} + m_1\cos\theta}{m_1 + m_2}\right)^2. \tag{4.115}$$

The recoil energy, i.e. the energy transfer ΔE to the target (m_2) appears as an energy loss of the scattered projectile:

$$\Delta E = \Delta E_1' - E_1 = \frac{1}{2}m_2 v_2'^2 = 4\frac{\mu}{M}E_1\cos^2\varphi, \tag{4.116}$$

where

$$M = m_1 + m_2, \tag{4.117a}$$

and

$$\mu = m_1 m_2/(m_1 + m_2) \tag{4.117b}$$

are the total and the reduced masses of the two particles, respectively. For the two simple cases of direct backscattering ($\theta = 0$) and right-angle scattering ($\theta = 90°$) (4.115) simplifies to

$$\frac{E_1'}{E_1} = \left(\frac{m_2 - m_1}{m_2 + m_1}\right)^2, \tag{4.118}$$

and

$$\frac{E_1'}{E_1} = \frac{m_2 - m_1}{m_2 + m_1}, \tag{4.119}$$

respectively.

The dependence of the kinetic energy E_1' of the scattered particle on the mass of the target m_2 (4.115–4.119) clearly shows that scattering of ions from a surface can be used to identify atomic species near or at the surface. Low-energy ions (1–5 keV) are produced by simple ion guns forming a focused beam which is directed onto the surface under study. The kinetic energy of the backscattered ions is analysed with a 127° deflector-type analyser (as used for electrons, Panel II: Chap. 1). For detection one might employ, for example, a channel electron multiplier. For high-energy scattering (50 keV–5 MeV), accelerators are required as ion sources. Energy analysis and detection are performed with various electromagnetic energy filters and with nuclear particle detectors (e.g., solid-state Schottky-barrier-type devices), respectively.

The low-energy regime (Low-Energy Ion Scattering, LEIS) is experimentally quite accessible and offers the additional advantage of very high surface sensitivity. The ions scatter predominantly from the first atomic layer and thus a *first monolayer* analysis is possible. As an example, Fig. 4.30 shows an energy spectrum for ^{20}Ne ions scattered from the surface of an Fe-Mo-Re alloy. The observed peaks at different kinematic factors E_1'/E_1 clearly reveal the presence of the different atomic species in the surface atomic layer [4.26].

A disadvantage of low-energy ion scattering is the high probability of the ions being neutralized at the surface and thus becoming invisible to any energy analyser using charge properties. At higher energies (above 50 keV), however, this neutralisation effect is less important, but ions with such high energies may penetrate hundreds and thousands of Ångstroms into the solid depending on their direction of incidence with respect to the lattice planes. Surface sensitivity can then be arranged only by utilising the concepts of *channeling, blocking*, and *shadowing* (Sect. 4.11). These techniques rely on the fact that high-energy ions penetrating into a crystal are forced to move along *channels* between atomic rows and planes. The penetration depth and thus also the probing depth depend strongly on the geometrical factors of the single scattering event, in particular on the direction of incidence and the angular distribution of the scattering cross section $\mathrm{d}S/\mathrm{d}\Omega$, (4.111), for a single collision.

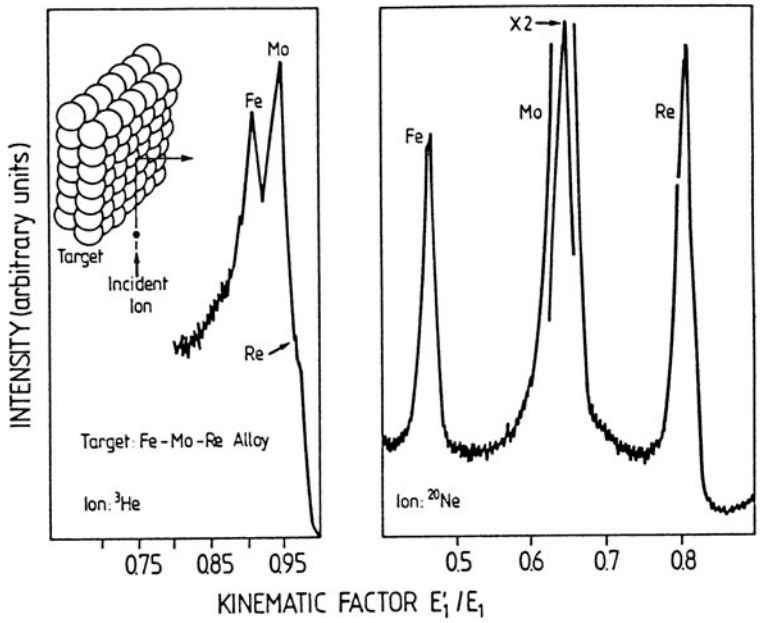

Fig. 4.30 RBS energy spectra for ^{3}He scattering and ^{20}Ne scattering from the surface of an Fe-Mo-Re alloy. The energy of the incident particles was 1.5 keV [4.26]

4.11 Rutherford BackScattering (RBS): Channeling and Blocking

In order to derive formulae for the scattering cross section, (4.111), for a twobody collision, details of the interatomic forces must be known. The most important case is that of Rutherford scattering, where a charged projectile (mass m_1, charge $Z_1 e$) is scattered in a Coulomb field

$$\mathcal{E} = \frac{Z_2 e}{4\pi\epsilon_0 r^2} = \frac{A}{r^2} \tag{4.120}$$

centered at a point C (Fig. 4.31). The Coulomb field might be that of an ion (charge $Z_2 e$) assumed to be much heavier than the particle m_1 and thus approximately at rest. Scattering into an angle θ, i.e. a change of momentum $\Delta \boldsymbol{p}$ from $\boldsymbol{p}_1$ to $\boldsymbol{p}_1'$ means, according to Fig. 4.31b,

$$\frac{1}{2}\frac{\Delta p}{m_1 v_1} = \sin(\theta/2), \quad \Delta p = 2m_1 v_1 \sin(\theta/2). \tag{4.121}$$

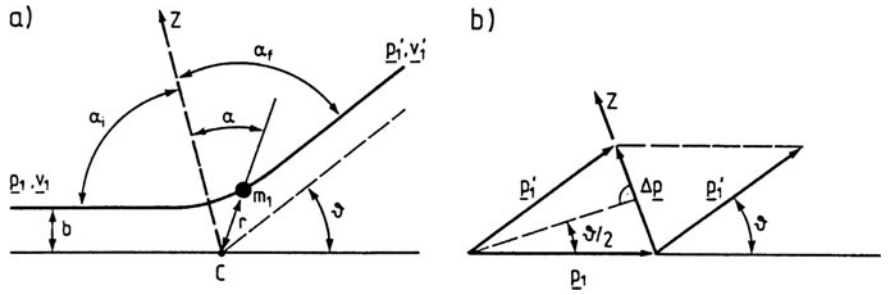

Fig. 4.31 Explanation of the symbols used for the description of a Rutherford scattering event of a particle with mass m_1 from a scattering center C at rest; (**a**) trajectory of the projectile described by impact parameter b, initial momentum and velocity $\boldsymbol{p}_1$, $\boldsymbol{p}_1$ and scattering angle θ. (**b**) Relation between initial momentum $\boldsymbol{p}_1$, final momentum $\boldsymbol{p}_1'$ after collision and momentum change $\Delta\boldsymbol{p}$

From Newtons law $\mathrm{d}\boldsymbol{p} = \mathcal{E}\mathrm{d}t$ we obtain the momentum change Δp in z direction (symmetry axis of scattering) according to Fig. 4.30a as

$$\Delta p = \int \mathrm{d}p_z = \int \mathcal{E}\cos\alpha \mathrm{d}t = \int \mathcal{E}\cos\alpha \frac{\mathrm{d}t}{\mathrm{d}\alpha}\mathrm{d}\alpha. \tag{4.122}$$

The derivative $\mathrm{d}t/\mathrm{d}\alpha$ can be related to the angular momentum of the particle about the origin. Since the force is central (it acts along the line joining the particle to the origin C, Fig. 4.31), there is no torque about the origin and the angular momentum is conserved. Its initial magnitude is $m_1 v_1 b$, and at a later time it can be expressed as $m_1 r^2 \mathrm{d}\alpha/\mathrm{d}t$. The conservation condition thus gives

$$m_1 r^2 \frac{\mathrm{d}\alpha}{\mathrm{d}t} = m_1 v_1 b, \quad \text{or} \quad \frac{\mathrm{d}t}{\mathrm{d}\alpha} = \frac{r_2}{v_1 b}. \tag{4.123}$$

With (4.122) we obtain the total momentum change during scattering

$$\Delta p = \frac{A}{r^2}\int \cos\alpha \frac{r^2}{v_1 b}\mathrm{d}\alpha = \frac{A}{v_1 b}\int \cos\alpha \mathrm{d}\alpha,$$
$$\Delta p = \frac{A}{v_1 b}(\sin\alpha_\mathrm{f} - \sin\alpha_\mathrm{i}). \tag{4.124}$$

The initial and final angles α_i and α_f can be expressed in terms of the scattering angle θ by

$$\sin\alpha_\mathrm{f} - \sin\alpha_\mathrm{i} = 2\sin(90° - \theta/2), \tag{4.125}$$

and the momentum change follows as

$$\Delta p = 2m_1 v_1 \sin(\theta/2) = \frac{A}{v_1 b} 2\cos(\theta/2). \tag{4.126}$$

The deflection function $\theta(b)$ is thus obtained as

$$b = \frac{A}{m_1 v_1^2} \cot(\theta/2) = \frac{Z_1 Z_2 e^2}{8\pi\epsilon_0 E_1} \cos(\theta/2) \tag{4.127}$$

with E_1 being the kinetic energy of the incident ion. According to (4.111b) one integration yields the Rutherford scattering cross section

$$\frac{\mathrm{d}S}{\mathrm{d}\Omega} = -\frac{b}{\sin\theta}\frac{\mathrm{d}b}{\mathrm{d}\theta} = \left(\frac{Z_1 Z_2 e^2}{8\pi\epsilon_0 E_1}\right)^2 \frac{1}{\sin^4(\theta/2)}. \tag{4.128}$$

It must be emphasized that in the above derivation the scattering center C is assumed to be at rest. Equation (4.128) can therefore be used only for collisions between a light particle m_1 and a much heavier target m_2 for which the recoil velocity v_2' can be neglected. As a numerical example we consider 180° scattering, i.e. backscattering of 2 MeV He ions ($Z_1 = 2$) from Ag atoms ($Z_2 = 47$). The distance of closest approach $r_{\min}$ of the projectile to the target may be estimated by equating the incident kinetic energy E_1 to the potential energy at $r_{\min}$:

$$r_{\min} = \frac{Z_1 Z_2 e^2}{4\pi\epsilon_0 E_1}. \tag{4.129}$$

For the present example (4.129) yields a minimum-approach distance of about $7 \cdot 10^{-4}$ Å, i.e. a distance much smaller than the Bohr radius of about 0.5 Å. This result shows that, for high-energy scattering of light ions, the assumption of an unscreened Coulomb potential for the calculation of scattering cross sections is justified. The backscattering cross section follows from (4.128) as $\mathrm{d}S(180°)/\mathrm{d}\Omega \approx 3 \cdot 10^{-8}$ Å^2.

From Sect. 4.10 it is evident that for general, two-body collisions, without the assumption of a heavy target at rest, the target will recoil from its initial position thus implying an energy loss of the projectile (4.116). An exact calculation of the Rutherford scattering cross section thus involves the treatment of a real two-body central-force problem. However, by introducing the concept of the reduced mass μ (4.117b) a reduction to a one-body problem is possible. For the two colliding particles in Fig. 4.29 Newton's law is

$$m_1 \ddot{\boldsymbol{r}}_1 = \boldsymbol{F} \quad \text{and} \quad m_2 \ddot{\boldsymbol{r}}_2 = -\boldsymbol{F}. \tag{4.130}$$

Defining the Center of Mass (CM) coordinate $\boldsymbol{R}$ by

$$\begin{aligned} (m_1 + m_2)\boldsymbol{R} &= m_1 \boldsymbol{r}_1 + m_2 \boldsymbol{r}_2 \\ \boldsymbol{R} &= \frac{m_1}{M}\boldsymbol{r}_1 + \frac{m_2}{M}\boldsymbol{r}_2, \end{aligned} \tag{4.131}$$

one obtains from (4.130) by subtraction and elimination of $\boldsymbol{r}_1$ and $\boldsymbol{r}_2$, and with the relative position vector $\boldsymbol{r} = \boldsymbol{r}_2 - \boldsymbol{r}_1$

$$M\ddot{\boldsymbol{R}} = \boldsymbol{0}, \text{ and } \mu\ddot{\boldsymbol{r}} = \boldsymbol{F}. \tag{4.132}$$

The two-body problem can thus be described as a force-free motion of the CM (4.132a) and a force F acting between the two particles within the moving CM inertial system. Within this CM system the kinematics of the collision thus reduces to the above problem of scattering of a particle with mass μ (4.117b) on a spatially fixed center. Within the CM system the particle coordinates are

$$\boldsymbol{R}_1 = \boldsymbol{r}_1 - \boldsymbol{R} = \frac{m_2}{M}\boldsymbol{r}, \quad \boldsymbol{R}_2 = \boldsymbol{r}_2 - \boldsymbol{R} = -\frac{m_1}{M}\boldsymbol{r}. \tag{4.133}$$

In analogy with the symbols for the laboratory system ($\boldsymbol{v}_1$, $\boldsymbol{v}_1'$, $\boldsymbol{v}_2'$, θ, φ, see Fig. 4.29a) we call the corresponding velocities and angles in the CM frame $\boldsymbol{V}_1$, $\boldsymbol{V}_1'$, $\boldsymbol{V}_2'$, Θ, Φ). From the vector diagrams in Fig. 4.29 one thus obtains

$$\tan\theta = \frac{V_1 \sin\Theta}{(\dot{R} + V_1 \cos\Theta)} = \frac{m_2 \sin\Theta}{m_1 + m_2 \cos\Theta} \tag{4.134}$$

for the transformation of the scattering angles between laboratory and CM frame. In the CM system the Rutherford scattering cross section is the same as (4.128), but only now expressed in terms of the CM scattering angle Θ, the reduced mass μ, and the solid angle element $\mathrm{d}\tilde{\Omega}$ measured in the CM system

$$\frac{\mathrm{d}S}{\mathrm{d}\tilde{\Omega}} = \left(\frac{Z_1 Z_2 e^2}{4\pi\epsilon_0 \mu V_1^2}\right)^2 \frac{1}{\sin^4(\theta/2)}. \tag{4.135}$$

The transformation back into the laboratory frame by means of (4.134) yields a general expression which takes into account the recoil of the target particle: This transformation involves essentially the solid-angle element $\mathrm{d}\tilde{\Omega} = \mathrm{d}(\cos\Theta)\mathrm{d}\phi'$ (ϕ' being the azimuthal angle in the CM frame). In the laboratory frame one has

$$\frac{\mathrm{d}S}{\mathrm{d}\Omega} = \frac{\mathrm{d}S\mathrm{d}\tilde{\Omega}}{\mathrm{d}\tilde{\Omega}\mathrm{d}\Omega} = \frac{\mathrm{d}S\mathrm{d}(\cos\Theta)}{\mathrm{d}\tilde{\Omega}\mathrm{d}(\cos\theta)} = \frac{\mathrm{d}S(\sin\Theta\mathrm{d}\Theta)}{\mathrm{d}\tilde{\Omega}\sin\theta\mathrm{d}\theta}, \tag{4.136}$$

i.e. the derivative $\mathrm{d}\Theta/\mathrm{d}\theta$ calculated from (4.134) allows direct transformation of the scattering cross sections

$$\frac{\mathrm{d}S}{\mathrm{d}\Omega} = \frac{\mathrm{d}S}{\mathrm{d}\tilde{\Omega}} \frac{(m_1^2 + m_2^2 + 2m_1 m_2 \cos\Theta)^{3/2}}{m_2^2(m_2 + m_1\cos\Theta)}. \tag{4.137}$$

With (4.134, 4.135) the Rutherford scattering cross section in the laboratory frame follows as

$$\frac{\mathrm{d}S}{\mathrm{d}\Omega} = \left(\frac{Z_1 Z_2 e^2}{8\pi\epsilon_0 E_1}\right)^2 \frac{4}{\sin^4\theta} \frac{\{[1 - (m_1/m_2)^2 \sin^2\theta]^{1/2} + \cos\theta\}^2}{[1 - (m_1/m_2)^2 \sin^2\theta]^{1/2}}. \tag{4.138}$$

For particle masses $m_1 \ll m_2$, this expression can be expanded in a power series

$$\frac{\mathrm{d}S}{\mathrm{d}\Omega} = \left(\frac{Z_1 Z_2 e^2}{8\pi\epsilon_0 E_1}\right)^2 \left[\frac{1}{\sin^4(\theta/2)} - 2\left(\frac{m_1}{m_2}\right)^2 + \ldots\right], \tag{4.139}$$

The next term is of the order of $(m_1/m_2)^4$. The leading term gives exactly (4.128), i.e. the Rutherford scattering cross section for a spatially fixed scattering center. In many realistic cases the correction $2(m_1/m_2)^2$ is small, e.g. about 4% for He ions ($m_1 = 4$) incident on Si ($m_2 = 28$). Nevertheless the energy loss of the projectile (4.116) might be appreciable.

For scattering of ions with lower energy the interaction potential between the two particles must include the effect of screening. The cross section is then slightly modified in comparison with (4.139). As an example, Fig. 4.32 shows a series of trajectories calculated for the scattering of He^+ ions (energy 1 keV) incident on an oxygen atom located at the origin of the diagram [4.27]. In this case an exponentially shielded Thomas-Fermi potential describes the interaction. Figure 4.32 demonstrates the existence of a *shadow cone* behind the scatterer. If another scatterer lies inside this cone, it is not "seen" by the incident ions and thus cannot contribute to the scattering. In this particular case of low-energy incident ions, a broad shadow cone of the order of half a typical interatomic distance, at about one interatomic spacing behind the scatterer, is observed. At high energies the screening becomes less important, a simple Coulomb potential can be used, and the shadow cone becomes much narrower. This is the situation in which *channeling* and *blocking* are very useful techniques for studying surfaces and interfaces as well as thin overlayers. Figure 4.33 displays high energy ions incident on a crystalline surface at two different angles for which channeling occurs. For these incidence angles only atoms in the top two atomic layers are "visible"; all deeper lying atoms lie in the shadow cones of the topmost layers. Ions on trajectories between these atoms are "channeled" down the gaps between the atoms and penetrate relatively deep into the solid. This channeling, occurring for an ion beam that is carefully aligned with a symmetry direction of a single crystal, is shown more in detail in Fig. 4.34.

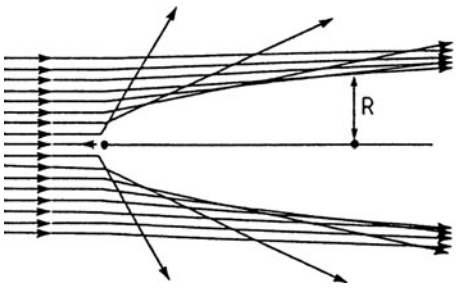

Fig. 4.32 Calculated shadow cone of 1-keV He^+ ions scattered from an oxygen atom at the coordinate origin. The trajectories describe ions travelling from left to right. The calculations are based on the assumption of a Thomas-Fermi-Moliere scattering potential [4.27]

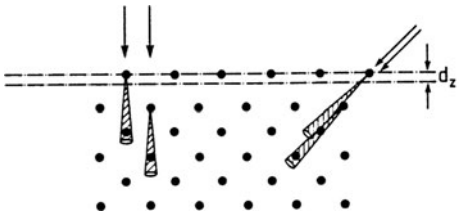

Fig. 4.33 Sectional view of a surface with relaxation d_z of the topmost atomic layer showing high-energy ion scattering shadow or blocking cones for incidence along two bulk channelling directions [4.27]

Ions not hitting a surface atom are steered through the channels formed by the rows of atoms. The ions cannot get close enough to the atomic nuclei to undergo large-angle Rutherford scattering. Small-angle scattering results with oscillatory trajectories of the projectile. The interaction can easily be described in a quasi-continuous model using a continuous rate $\mathrm{d}E/\mathrm{d}x$ of energy loss along the channel [4.25]. Because of the large penetration depth of hundreds of Ångstroms (Fig. 4.34), scattering from the substrate is drastically reduced, sometimes by a factor of 100, as compared with a non-channeling situation.

The experimental example [4.29] in Fig. 4.35 of 1.4-MeV He^+ ions scattered from a GaAs{100} surface along the surface normal [100] exhibits two sharp peaks due to scattering from the Ga and As surface atomic layer. The energy losses can be calculated using (4.116). For energies lower than that of the surface peak a low-intensity plateau of backscattered ions occurs. These ions result from the few scattering events deeper in the bulk. On their channeling path the incident primary ions continuously lose small amounts of energy, mainly by electronic excitations such as the creation of plasmons, etc. The penetrating ions undergo some rare backscattering events and thus give rise to scattered energies which are reduced in proportion to their channeling depth.

The situation is different, however, when the angle of incidence does not coincide with a low index direction and channeling does not occur (Fig. 4.33). Under this *random* incidence condition many subsurface atomic layers are hit and backscattering occurs from many deeper lying atoms. The backscattering spectrum exhibits

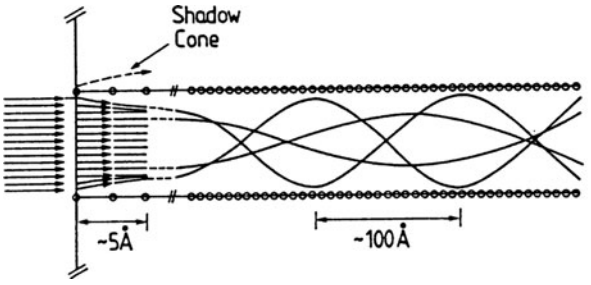

Fig. 4.34 Schematic representation of particle trajectories undergoing scattering at the surface and channeling within the crystal. The depth scale is compressed relative to the width of the channel in order to display the shape of the trajectories [4.25]

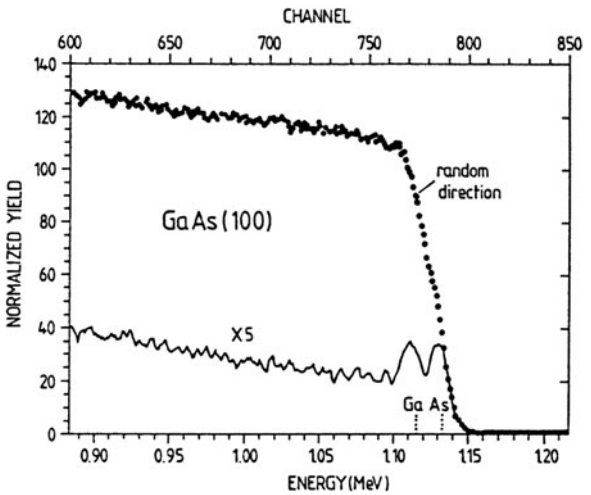

Fig. 4.35 Ion backscattering yield spectra of 1.4-MeV He^+ from a GaAs(100) surface along a "random" non-channeling direction and along the surface normal ⟨100⟩, amplified by a factor of 5 [4.29]

a high-intensity continuum of scattered energies up to a maximum defined by the *surface peak* due to scattering on the topmost atomic layer (Fig. 4.35). Slight variations of the angle of incidence with respect to the lattice orientation can thus significantly change the backscattering yield, in particular for energies lower than the surface peak. Because of the continuous energy loss of the primary ions on their path through the crystal there is also a simple relation between scattering depth and energy loss. These properties can be applied in a number of ways to obtain interesting information about the incorporation of impurities, relaxation effects, quality of interfaces and overlayers, etc. [4.25]. In Fig. 4.36a qualitative overview of some examples of backscattering spectra is presented. The dashed spectra represent the scattering yield from a crystal with an ideal surface under channeling conditions. The surface peak is due essentially to scattering from only the topmost atomic layer (a). If a reconstruction is present for which the surface atoms are displaced in the plane of the surface (b), then the second atomic plane is no longer completely shadowed and therefore contributes to the backscattering yield. For a major reconstruction, the surface peak might reach an intensity of twice that of the ideal crystal. In the case of a relaxation (c), where the topmost atomic layer is displaced normal to the surface, non-normal incidence is necessary for the investigation. A geometry is used in which the shadow cones arising from the surface atoms are not aligned with the atomic rows in the bulk. In this situation both the surface and the second atomic layer contribute to the surface peak and increase its intensity. A measurement at normal incidence would yield a surface peak intensity equivalent to scattering on one atomic layer. An adsorbate layer on top of an ideal surface (d) gives rise to a new surface peak shifted in energy with respect to that of the clean surface. The sensitivity of ion scattering to atomic mass (Sect. 4.10) allows discrimination between substrate and adsorbate. If the adsorbate atoms lie directly

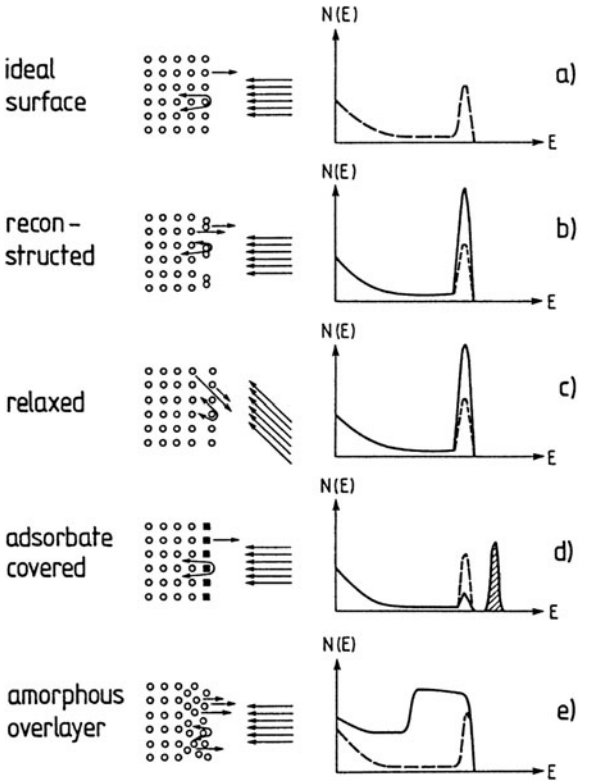

Fig. 4.36a–e Qualitative overview of some applications of ion backscattering and the corresponding spectra $N(E)$: (**a**) Scattering from an ideal clean crystal surface under channeling conditions. The backscattering spectrum (dashed curve) consists of a *surface peak* due to scattering on the topmost atomic layer and a low intensity plateau at lower kinetic energies which arises from scattering events deep in the bulk. (**b**) Scattering on a reconstructed surface causes a considerable increase of the surface peak (up to double intensity) in comparison with the ideal surface spectrum (dashed curve). The second atomic plane contributes to the scattering events due to incomplete shadowing. (**c**) For a relaxed surface, non-normal incidence under channeling conditions causes a similar intensity increase of the surface peak due to incomplete shadowing (dashed curve: spectrum of unrelaxed ideal surface). (**d**) Scattering on an ideal surface covered with an adsorbate overlayer under channeling conditions. The adsorbate layer gives rise to a second surface peak (shaded) due to scattering on atoms with different mass. Due to shadowing, the original surface peak (dashed curve) is reduced in intensity. (**e**) Scattering on a crystal covered with an amorphous overlayer gives rise to a broad plateau instead of a sharp surface peak. Many atoms out of registry contribute to the scattering in deeper layers. For comparison, the dashed line shows the spectrum for scattering on an ideal crystal surface [4.25]

above the substrate atoms, the substrate surface peak is strongly reduced in intensity. The case of an amorphous overlayer on top of a crystalline substrate (produced, e.g., by ion bombardement or laser irradiation) is illustrated in Fig. 4.36e. Since the atoms within the amorphous overlayer are out of registry, channeling is no longer possible. A broad plateau with high intensity is obtained in the backscattering yield,

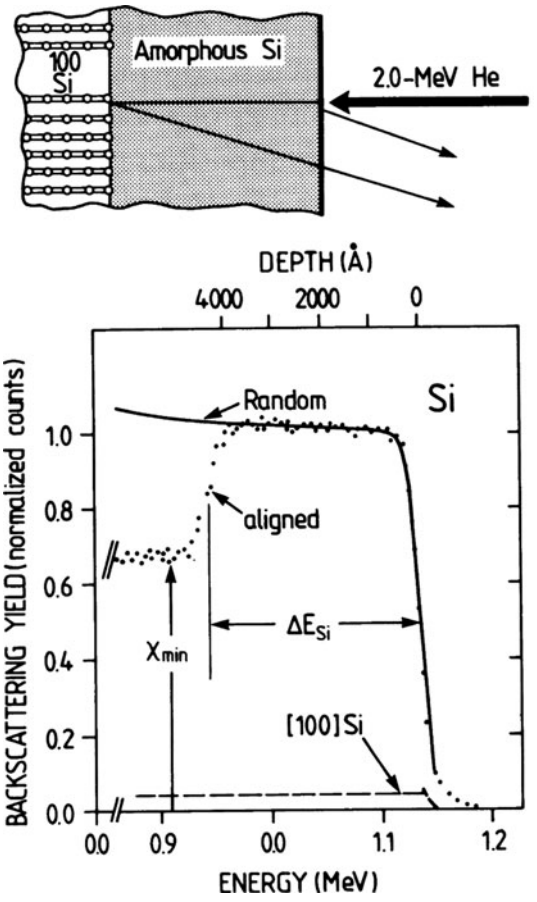

Fig. 4.37 Backscattering channeling spectrum (ion yield versus kinetic energy) of a 4000-Å thick amorphous Si-layer on top of a Si(100) surface. The spectrum was obtained under channeling conditions with 2-MeV ^{4}He ions (inset). Using a mathematical model for the Rutherford backscattering processes, the energy scale is converted into a depth scale (upper abscissa). For comparison, the spectra of the Si surface before amorphization are also given, for channeling conditions by the dashed line, and for "random" conditions by the full line [4.28]

since numerous atoms contribute to scattering as in the case of *random* incidence on a crystalline material. The energetic width of the plateau is directly related to the thickness of the amorphous layer and the presence of the amorphous-crystalline interface is seen from the decrease of the backscattered intensity at lower energies. The intensity does not drop to the values for the completely crystalline material (a-d), since a high number of ions are deflected from their channeling direction within the amorphous overlayer. As an experimental example of such a system Fig. 4.37 exhibits the channeling spectrum of an approximately 4000 Å thick amorphous Si layer on Si(100) [4.28]. 2-MeV ^{4}He ions were used in this investigation. The energy spectrum of the backscattered ions is transformed into a thickness scale (upper abscissa). For comparison, the spectrum of the clean Si(100) surface before amorphization is also shown.

Further information can be obtained from RBS experiments by studying the angular dependence of the backscattering yield. In Fig. 4.38 a Si film with $1.5 \cdot 10^{21}\,\mathrm{cm}^{-3}$ As atoms incorporated has been investigated [4.30]. The Si and the As backscattering yields show a very similar angular dependence. The minimum

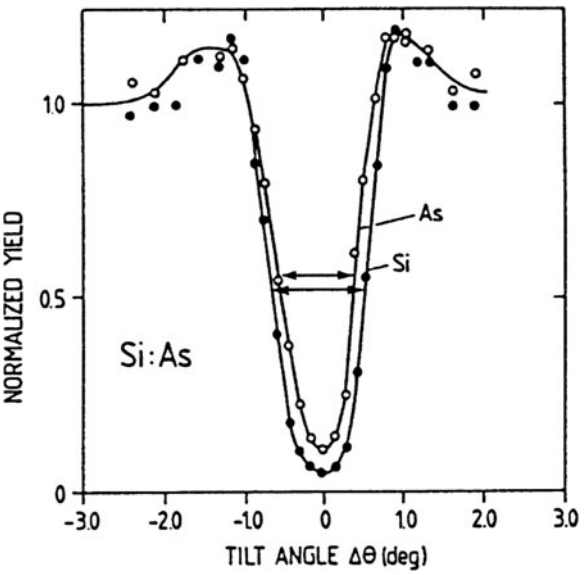

Fig. 4.38 Angular dependence of the backscattering yield around the channeling direction (tilt angle $\Delta\theta = 0$) for 1.8 MeV He ions on a Si-film, which is doped with $1.5 \cdot 10^{21}$ As atoms/cm^3. The angular dependence of the Si and of the As backscattering peak are compared [4.30]

yield corresponds, of course, to the channeling direction. The similarity of the two curves clearly indicates that the perturbation of the lattice due to As incorporation is negligible. As is built in as a substitutional impurity. In complete contrast are the angle-resolved spectra (Fig. 4.39) for Yb implanted into a Si film (concentration $5 \cdot 10^{14}$ cm^2). Exactly in the Si channeling direction (minimum of Si signal) a strong

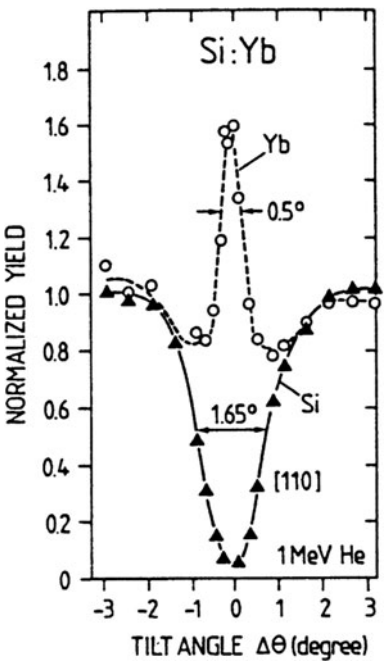

Fig. 4.39 Angular dependence of the backscattering yield (normalized) around the [110] channeling direction (tilt angle $\Delta\theta = 0$) for 1 MeV He ions on a Si film, into which $5 \cdot 10^{14}$ Yb atoms/cm^2 are implanted (60 keV, 450°C). The Si signal (▲) is compared with the Yb signal (○) [4.31]

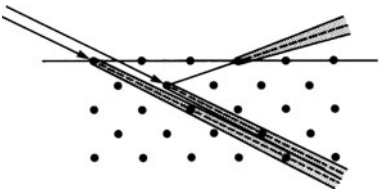

Fig. 4.40 Double-alignment scattering geometry, schematic view of a (010) scattering plane perpendicular to the (100) surface for the example of silicon

peaking of the Yb signal is observed thus demonstrating that Yb is not incorporated on Si sites but rather as an interstitial.

A further RBS technique used in surface crystallography is the so-called double alignment (Fig. 4.40). The primary ion beam is aligned with a low-index crystal direction for channeling, such that only atoms in the first two atomic layers are hit. All deeper lying atoms are shadowed. An ion immediately below the surface can leave the crystal in any direction except that in which its outgoing trajectory is blocked by an atom in the topmost atomic layer. In this direction there will be a minimum in the yield of ions backscattered from the surface, the surface blocking minimum. Deviations of the observed minimum position from that calculated for an ideal surface give information about surface reconstructions and relaxations. The Si(100) surface with adsorbed atomic hydrogen [hydrogen-stabilized Si(100)-(1×1)2H] has been studied in this way (Fig. 4.41). The observed shift of the surface blocking minimum from its calculated position (arrows and dashed curves) leads to the conclusion that the surface is relaxed inward by (-0.08 ± 0.03) Å, or (-6 ± 3)% of the interplanar distance [4.32].

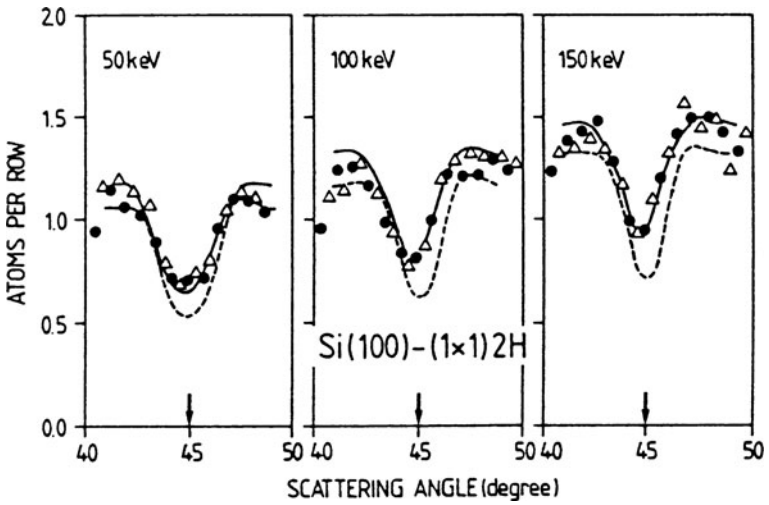

Fig. 4.41 Experimental surface blocking profiles obtained in a scattering geometry as in Fig. 4.40 for H^+ (protons) with energies of 50, 100 and 150 keV scattered on a hydrogen stabilized Si(100)-(1×1)2H surface. Circles and triangles represent results from different experimental runs. The arrows indicate the position of the blocking minimum; the dashed curves are calculated for a truncated bulk without any relaxation [4.32]

Panel VIII
Low-Energy Electron Diffraction (LEED) and Reflection High-Energy Electron Diffraction (RHEED)

Elastic scattering or diffraction of electrons is the standard technique in surface science for obtaining structural information about surfaces. The method is applied both to check the crystallographic quality of a freshly prepared surface and as a means of obtaining new information about atomic surface structure. As in all diffraction experiments, the determination of an atomic structure falls naturally into two parts: the determination of the periodicity of the system and thus the basic unit of repetition or the surface unit mesh, and the location of the atoms within this unit. The first part, the evaluation of the surface unit mesh is straightforward and involves simple measurements of symmetry and spot separation in the diffraction pattern. Since the diffraction pattern corresponds essentially to the surface reciprocal lattice (Sect. 4.2), the reverse transformation yields the periodicity in real space. The second part, the determination of atomic coordinates, requires a detailed measurement of diffracted intensities. The LEED technique is frequently used for this purpose, even though the theoretical problem of deriving an atomic structure from the measured intensities is far from simple, due to the "strong" interaction of slow electrons with a solid. The analysis of the geometry and intensity of a LEED diffraction pattern is discussed in Sects. 4.2–4.4.

The standard experimental set up for LEED consists of an electron gun to produce an electron beam with primary energies in the range of 20–500 eV and a display system for observing the Bragg diffraction spots. The energy range below 300 eV is particularly suited to surface studies since the mean-free path of these slow electrons in the solid is short enough to give good surface sensitivity (Chap. 4). Furthermore, according to the de Broglie relation

$$\lambda = (150.4/E)^{1/2} \qquad \text{(VIII.1)}$$

(λ in Å and E in eV), typical LEED wavelengths are in the Ångstrom range, comparable with wavelengths used in X-ray crystallography, and of the same magnitude as the interatomic distances in a solid.

A typical three-grid LEED system is exhibited in Fig. VIII.1a. The electron gun unit consists of a directly or indirectly heated filament with a Wehnelt cylinder W followed by an electrostatic lens with apertures A, B, C, D. The acceleration energy

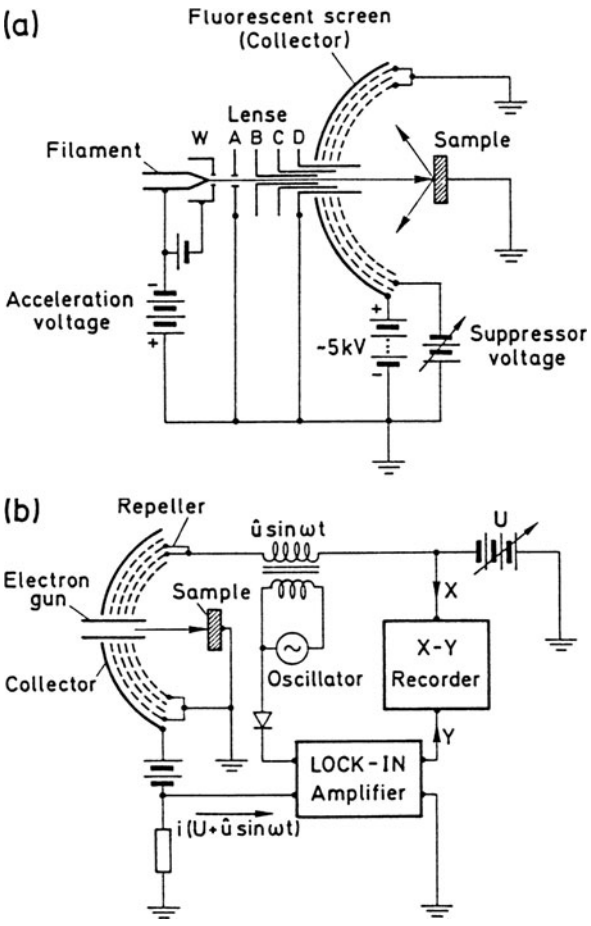

Fig. VIII.1 (**a**) Schematic of a three-grid LEED optics for electron diffraction experiments. The integrated electron gun consists of a heated filament, a Wehnelt cylinder (W) and the electron optics containing the apertures A–D. B and C are usually held at potentials between those of A and D. (**b**) Circuit for using a four-grid LEED optics as a retarding field (RF) electron energy analyser. The retarding voltage U determines what fraction of the inelastically scattered electrons reaches the collector. Differentiation of the measured electron current $i(U+u\sin\omega t)$ with respect to U is done by means of the superimposed AC voltage $u\sin\omega t$ ($u \approx 1$ V) and subsequent Lock-in detection of i. For $u \ll U$ one has $i(U+u\sin\omega t) = i(U) + i'(U)u\sin\omega t + (1/2)i''(U)u^2\sin^2\omega t + \ldots$, and phase-sensitive detection at the first harmonic ω yields an output signal which is proportional to the derivative $i'(U)$

(20–500 eV) is determined by the potential between the cathode and apertures A and D. Apertures B and C have potentials intermediate between A and D and are used to focus the electron beam. Initial collimation is achieved by the Wehnelt cylinder which has a somewhat negative bias with respect to the cathode filament. The last aperture D, also called the *drift tube*, is usually at the same (earth) potential

as aperture A and the sample; the same is true for the first and last grids in front of the fluorescent screen. Thus a field-free space is established between the sample and the display system through which the electrons travel to the surface and back after scattering. The fluorescent screen (collector) has to be biased positively ($\approx 5\,\mathrm{kV}$) in order to achieve a final acceleration of the slow electrons; only high-energy electrons can be made visible on the screen. Besides elastic scattering, inelastic scattering also occurs at the sample surface, thus giving rise to electrons of lower energy. These electrons are scattered through wide angles and produce a relatively homogeneous background illumination of the phosphor screen. This background illumination is suppressed by giving the middle grid a somewhat negative bias. The inelastically scattered electrons are thus prevented from reaching the collector.

The emission current of standard equipment is on the order of $1\,\mu\mathrm{A}$; it varies with primary energy but electronic stabilization may be used to fix its value. The energy spread is about 0.5 eV, attributable mainly to the thermal energy distribution. The diameter of the primary beam is on the order of 1 mm.

As is shown in Fig. VIII.1b, standard LEED optics (four grids are preferred in this case) can also be used as an energy analyser. The electrons coming from the sample have to overcome a retarding field before they reach the collector. For a retarding voltage, U, the current reaching the collector is

$$i(U) \propto \int_{E=eU}^{\infty} N(E)\mathrm{d}E, \tag{VIII.2}$$

where $N(E)$ is the energy distribution of the incoming electrons. By superposing an AC voltage $u \sin \omega t\,(u \ll U)$ and using phase-sensitive detection $i(U)$ in (VIII.2) can be differentiated allowing $N(E)$ to be easily obtained (Fig. VIII.1b).

The standard LEED equipment displayed in Fig. VIII.1a is used mostly for characterizing the crystalline perfection etc., of a clean surface. For investigating adsorbate layers, semiconductor surfaces and for LEED intensity studies this setup has severe disadvantages. The current density of $\approx 1\,\mu\mathrm{A}$ in the primary beam is rather high. Thus organic adsorbates and clean semiconductor surfaces may suffer severe damage. Furthermore the measurement of intensity-voltage $i(V)$ curves for a number of diffraction beams and several surface orientations requires the collection of very many data. Recent experimental developments have thus aimed to decrease the primary current and enable much faster data acquisition. Figure VIII.2 shows an advanced display system, where the primary current is decreased by four orders of magnitude to $10^{-10}\,\mathrm{A}$. A bright LEED pattern is then obtained by two channel plates which amplify the backscattered electron currents by a factor of about 10^7. Since inspection of the fluorescent screen (fiber optics with phosphor coating) is possible from behind via a mirror, the whole unit is extremely versatile; it can be flanged to standard ports of a UHV chamber. By changing the potentials at the grids or the channel plates, etc, (Fig. VIII.2) the same unit can be used for measurements of the angular distribution of (ionic) Electron Stimulated Desorption products (ESDIAD, Panel XIV: Chap. 10). In these experiments an electron beam is incident on an adsorbate covered surface and the angular distribution of the desorbing ions

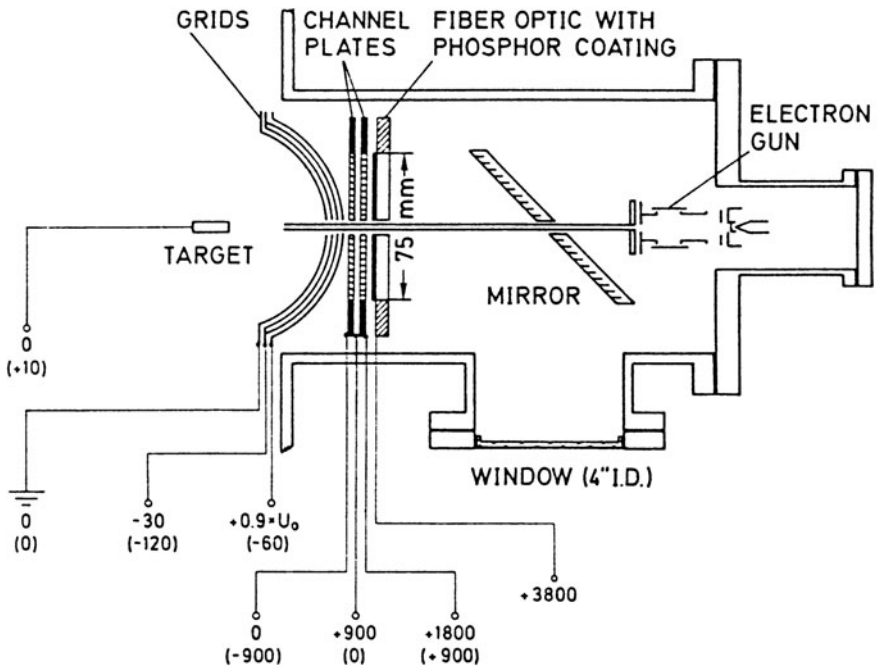

Fig. VIII.2 Schematic of a low-current optical display for LEED and ESDIAD (electron stimulated desorption ion angular distribution, Panel XIV: Chap. 10). In LEED primary beam currents in the 10^{-10} A range can be used, the channel plates enable amplification of the detected electron currents by factors in the 10^7 range. Typical bias potentials [eV] are also indicated. For ESDIAD the potentials are given in brackets; U_0 is the acceleration (primary) voltage [VIII.1]

yield information about the bonding geometry of the adsorbed species (Panel XIV: Chap. 10).

Another modern improvement to the LEED equipment is to be found in so-called DATALEED (Fig. VIII.3). Here, extremely fast data acquisition is achieved by the application of an electronic video (TV camera) unit to measure the LEED spot intensities accompanied by computer-controlled data handling. At present the time required to determine the integral intensity of a LEED beam at a particular energy is 20 ms including background subtraction. A whole LEED intensity spectrum is measured by this equipment in about 10 s depending on the energy steps and the energy range covered. Thus time-dependent LEED intensity analysis (Sect. 4.4), i.e. structure analysis during, e.g., surface phase transitions, becomes feasible.

Besides LEED, the second important electron diffraction technique in interface and thin film physics is RHEED (Reflection High-Energy Electron Diffraction). High energy electrons with primary energies between 10 and 100 keV are incident under grazing angles (3°–5°) onto the sample surface, and the diffracted beams are observed at similar angles on a fluorescent screen (Fig. VIII.4a). The electron guns used in RHEED are slightly more complex than those of LEED; in some cases a magnetic lens is used for focussing because of its greater efficiency at higher

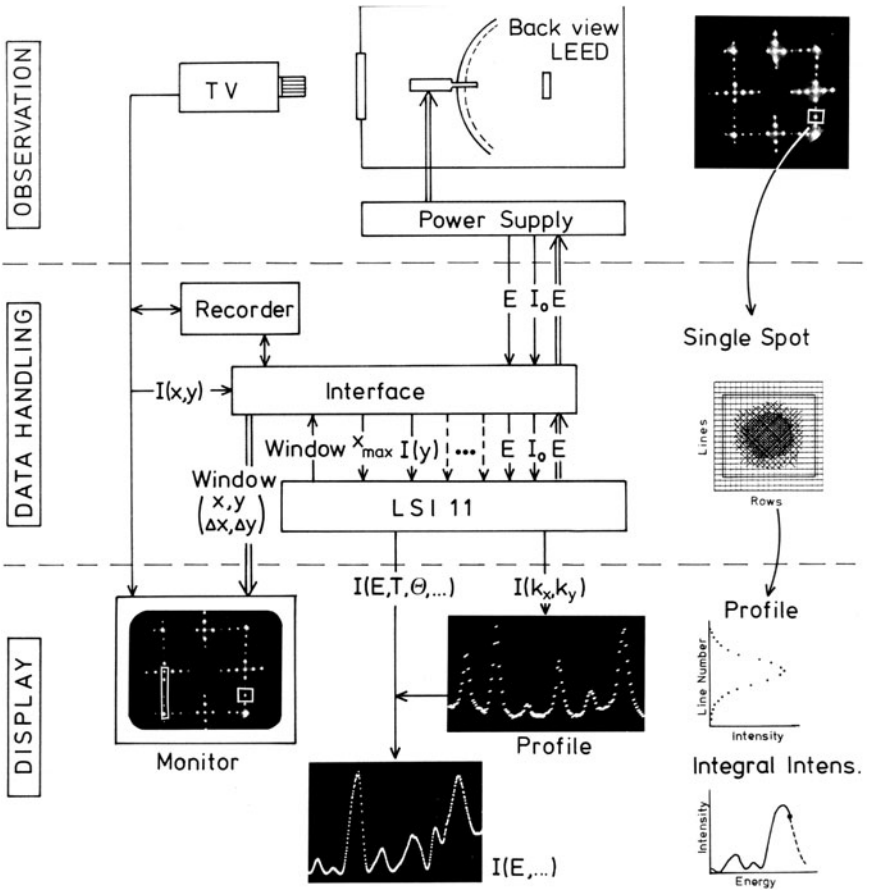

Fig. VIII.3 Information-flow diagram from observation through data handling to display of intensities by the computer controlled fast LEED system DATALEED. A video signal is generated by the TV camera viewing the LEED pattern from the back of a transparent fluorescent screen. The computer controlled system generates an electronic window of variable size and shape around a certain spot or group of spots and stores up to 10^3 pixels of digital information in a fast memory. The electronic window is made to follow the spot as it moves over the screen with varying beam energy E. The computer LSI 11 calculates intensity versus energy $I(E)$ spectra, integral intensities, FWHM of profiles, etc. Single lines carry information, double lines represent control channels [VIII.21]

electron velocities. The much higher voltages used in RHEED require special power supplies and vacuum feed-throughs. The fluorescent screen needs no high-voltage source; no acceleration of the electrons is necessary since the high primary energies are sufficient to produce fluorescence. The screen is usually planar and is sometimes coated onto the inside of a window of the UHV system along with a conducting film to prevent charging. No energy filtering of inelastic and secondary electrons is necessary since the diffracted beams are much more intense than the background. Since

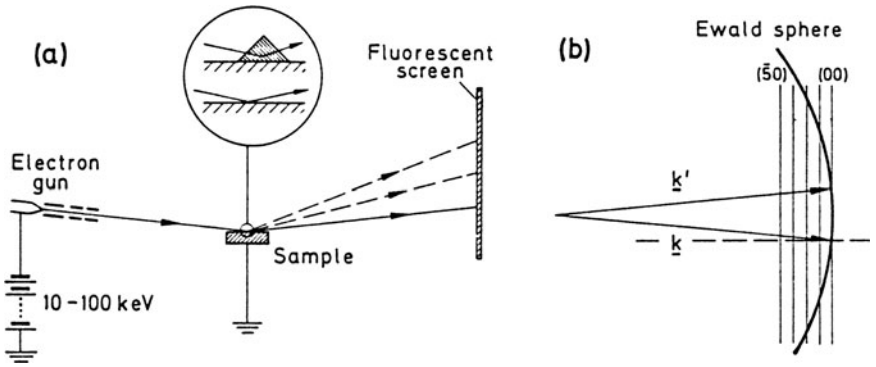

Fig. VIII.4 (**a**) Schematic of the experimental set-up for RHEED. The inset shows two different scattering situations on a highly enlarged surface area: surface scattering on a flat surface (below) and bulk scattering by a three-dimensional crystalline island on top of the surface (above). (**b**) The Ewald sphere construction for RHEED. $\boldsymbol{k}$ and $\boldsymbol{k}'$ are primary and scattered wavevectors, respectively. The sphere radius $k = k'$ is much larger than the distance between the reciprocal lattice rods (hk). For more details, see Sect. 4.2 and Figs. 4.2, 4.3

the spatial separation of the electron gun and sample, and of sample and screen can be of the order of 50 cm the method is very flexible in relation to sample conditions. For example, one can use RHEED to study in situ surfaces at elevated temperatures during molecular beam epitaxy (Sect. 2.4).

In spite of the high primary energies, RHEED has a similar surface sensitivity to LEED: the grazing incidence and detection angles mean that a long mean-free path through the sample is associated with penetration normal to the surface of only a few atomic layers. The diffraction pattern in RHEED is rather different from that of LEED. Figure VIII.4b illustrates the Ewald construction for the conditions of a RHEED experiment. Because of the extremely high primary energies the diameter of the Ewald sphere is now much larger than a reciprocal lattice vector. The reciprocal lattice rods (Sect. 4.2) are cut at grazing angles in the region corresponding to a diffracted beam emerging close to the surface. The Ewald sphere "touches" the rods of the reciprocal lattice. Both the Ewald sphere and reciprocal lattice rods are smeared out, to some extent, due to the angular and energy spread of the primary beam, respectively, and to deviations from ideal translational symmetry in the surface (phonons, defects, etc.). Thus the diffraction pattern will usually consist not of spots, but of streaks corresponding to the sections of reciprocal lattice rod intersected. It must be emphasized, however, that on extremely flat and ideal surfaces, and with very good instrumentation, one can occasionally observed very sharp diffraction spots.

An example of RHEED patterns is shown in Fig. VIII.5. Because of the grazing-angle electron beams, very flat sample surfaces are needed in RHEED. Asperities or stronger deformations shadow part of the surface. If there are crystalline islands or *droplets* on the surface, on the other hand, bulk scattering of the grazing beam can occur and the RHEED pattern may become dominated by spots rather than streaks

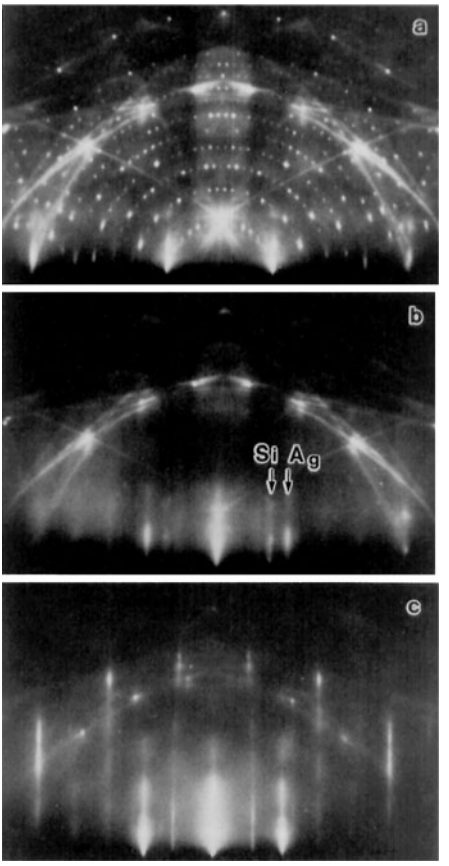

Fig. VIII.5a–c RHEED patterns taken with a primary energy of $E = 15\,\text{keV}$ and a direction of incidence of [112] on a Si(111) surface: (**a**) Clean Si(111) surface with a (7×7) superstructure. (**b**) After deposition of nominally 1.5 monolayers (ML) of Ag streaks due to the Ag layers are seen on the blurred (7×7) structure. (**c**) After deposition of 3 ML of Ag the texture structure due to the Ag layers develops in place of the (7×7) structure [VIII.3]

due to transmission electron diffraction (insert in Fig. VIII.4a). This particular property of RHEED, however, can be usefully exploited to study surface corrugation and growth modes of films during deposition and epitaxy. Stransky-Krastanov growth of islands (Chap. 3) can be readily identified through the spots in the RHEED pattern.

In both LEED and RHEED, the primary electron beam deviates from an ideal plane wave $A\exp(i\boldsymbol{k}\cdot\boldsymbol{r})$. It is actually a mixture of waves of slightly different energy and direction. These deviations from the ideal direction and energy are caused by the finite energetic width ΔE (thermal width $\approx 500\,\text{meV}$) and the angular spread 2β of the beam. The electrons impinging on the crystal surface exhibit therefore slight random variations in phase; if two spots on the surface have too large a separation, the incoming waves cannot be considered as coherent. The phases are not correlated and the outgoing waves cannot interfere to produce a diffraction pattern. There is a characteristic length called *coherence length* such that atoms in the surface within a coherence length (or radius) can be considered as illuminated by a simple plane wave. Waves scattered from points separated by more than a coherence radius add

in intensity rather than in amplitude. Thus no surface structure on a scale larger than the coherence length forms a diffraction pattern.

The two contributions responsible for limiting the coherence are the finite energy width ΔE and the angular spread 2β, giving rise to incoherence in time and space, respectively. Since $E = \hbar^2 k^2/2m$, the energy width

$$\Delta E = \frac{\hbar^2}{m} = k\Delta k \tag{VIII.3}$$

is related to an uncertainty in wave vector (due to time incoherence)

$$\Delta k^{\mathrm{t}} = k\frac{\Delta E}{2E}, \tag{VIII.4}$$

i.e. for the component parallel to the surface (at normal incidence)

$$\Delta k_{\parallel}^{\mathrm{t}} \simeq k\beta\frac{\Delta E}{E}. \tag{VIII.5}$$

The finite angular spread 2β causes an uncertainty in wave vector parallel to the surface (due to space incoherence) of

$$\Delta k_{\parallel}^{\mathrm{s}} \simeq 2k\beta. \tag{VIII.6}$$

Since the two contributions are independent, the total uncertainty in $k_{\parallel}$ is

$$\Delta k_{\parallel} = \sqrt{(\Delta k_{\parallel}^{t})^2 + (\Delta k_{\parallel}^{\mathrm{s}})^2} \tag{VIII.7}$$

and because of Heisenberg's uncertainty relation

$$\Delta r_{\mathrm{c}}\Delta k \simeq 2\pi, \tag{VIII.8}$$

the coherence radius Δr_{c} is obtained as

$$\Delta r_{\mathrm{c}} \simeq \frac{\lambda}{2\beta\sqrt{1 + (\Delta E/2E)^2}}, \tag{VIII.9}$$

where λ (VIII.1) is the wavelength of the electrons.

In a standard LEED experiment, the angular width of the primary beam is $\approx 10^{-2}$ rad with an energy spread of ≈ 0.5 eV. At a primary energy of ≈ 100 eV this leads to a coherence length of about 100 Å. In RHEED the primary energy is much higher ($\approx 5 \cdot 10^4$ eV) and the beam collimation is also better ($\beta \approx 10^{-4} - 10^{-5}$ rad), but because of the grazing incidence, $\Delta k_{\parallel} \simeq \Delta k$. Thus only a slightly larger coherence zone remains than in LEED. Because of the finite coherence in LEED and RHEED only limited information about the degree of long-range order on the surface can

be obtained. If the long-range order is restricted to areas smaller than the coherence zone (diameter ≈ 100 Å) the diffraction pattern is weaker with a higher incoherent background. Much experimental effort has been undertaken to increase the coherence length considerably by using better electron optics. Coherence radii of several thousand Ångstroms have meanwhile been achieved enabling small deviations from long-range order to be investigated by LEED [VIII.4, VIII.5].

References

VIII.1 C.D. Kohl, H. Jacobs: Private communication
VIII.2 K. Heinz, K. Müller: *Experimental Progress and New Possibilities of Surface Structure Determination*. Springer Tracts Mod. Phys. **91** (Springer, Berlin, Heidelberg 1982)
VIII.3 S. Hasegawa, H. Daimon, S. Ino: Surf. Sci. **186**, 138 (1987)
VIII.4 K.D. Gronwald, M. Henzler: Surf. Sci. **117**, 180 (1982)
VIII.5 M. Henzler: Appl. Phys. A **34**, 209 (1984)

Panel IX
Electron Energy Loss Spectroscopy (EELS)

Electron Energy Loss Spectroscopy (EELS) refers, in a broad sense, to every type of electron spectroscopy in which inelastic electron scattering is used to study excitations of surfaces or thin solid films [IX.1, IX.2]. The experiment thus involves the preparation of a more or less monoenergetic electron beam, scattering on a solid surface or within a thin solid film, and energy analysis of the electrons inelastically scattered at a certain angle by means of an electron analyser (Panel II: Chap. 1). The inelastic scattering process requires time-dependent scattering potentials (phonons, plasmons, adsorbate vibrations, electronic transitions etc.). The theory can be developed within a quite general formalism as in Sect. 4.1 or in a more restricted framework for scattering on long-range potentials (dielectric theory) as in Sect. 4.6 [IX.2, IX.3].

Since many different solid excitations can be studied (Fig. IX.1) over a wide energy range from some meV to more than 10^3 eV, different experimental equip-

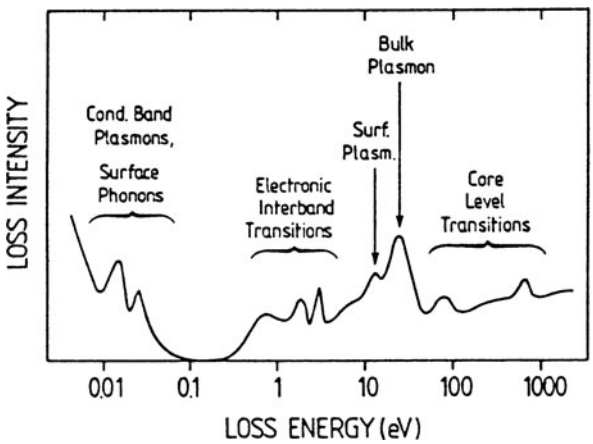

Fig. IX.1 Qualitative overview of the major excitation mechanisms which can contribute to an electron energy loss spectrum over a wide loss energy range. For investigating the different loss energy regimes, in particular below and above 1 eV different experimental set-ups are required

ment is necessary to provide the required energy resolution at very small and very high excitation energies.

Here we describe briefly the main applications of EELS and important features of the experimental set-ups but do not go into details of the scattering theory. Further details of the theory are given in Chap. 4. When EELS is performed with high energetic resolution at low primary energies, $E_0 < 20\,\text{eV}$, it is called *High Resolution Electron Energy Loss Spectroscopy* (HREELS). The primary electron beam then has to be monochromatized, usually by means of a hemispherical or cylindrical electron analyzer (Panel II: Chap. 1). Extremely good monochromaticity is now achieved with halfwidths (FWHM) of the primary beam around 1 meV [IX.4]. At these low primary energies only reflection scattering experiments under UHV conditions are possible. The backscattered beam is analysed by means of a similar electron analyser. For dielectric scattering (Sect. 4.6) with small wave-vector transfer, the scattered electrons are detected in specular direction, whereas detection at various angles is necessary when the dispersion relations of surface excitations (phonons, etc.) are measured. This technique has revealed much interesting information about surface-phonon dispersion branches on clean and adsorbate-covered metal surfaces (Chap. 5).

On semiconductor surfaces typical free-carrier (electrons in the conduction or holes in the valence band) concentrations in the $10^{17}\,\text{cm}^{-3}$ range give rise to bulk and surface plasmons with energies in the 20–100 meV range. The surface plasmons can be conveniently detected by HREELS, since for primary energies below 20 eV surface scattering prevails and major loss structures occur for $\text{Re}\{\epsilon(\omega)\} \simeq -1$, $\epsilon(\omega)$ being the dielectric function of the sample (Sect. 5.5). One can also study the coupling of these surface plasmons to surface phonons carrying a dynamic dipole moment (*Fuchs-Kliewer surface phonons*) (Sect. 5.5).

By far the widest application of HREELS is concerned with the study of vibrations of adsorbed atoms or molecules; here it is used to identify adsorbed species and to get information about adsorption sites and bonding geometry [IX.2]. The identification of an adsorbed species relies on the knowledge of its vibrational spectrum from the IR absorption or Raman measurements in the gas phase. Selection rules for IR dipole absorption and Raman scattering must be taken into account, as well as the dipole selection rule in HREELS for dipole scattering on surfaces: only dipole moments normal to the surface give rise to significant dielectric scattering. Dipole moments parallel to the surface can only be detected in off-specular geometry (Sect. 4.1). The application of these selection rules allows one to draw conclusions about the adsorption geometry of a molecule: for example, chemical bonds oriented parallel to a solid surface cannot give rise to strong dipole scattering from their stretching mode in the specular direction. The adsorption site of an atom or molecule can sometimes be deduced from the occurrence of particular adsorbate-substrate atom vibrations. The occurrence of an As–H stretch vibration, for example, clearly signifies that an As surface atom on GaAs the bonding site for a hydrogen containing adsorbate. As an example of an adsorbate vibrational spectrum Fig. IX.2 presents a loss spectrum measured on a Ni(110) surface exposed to 8 L of cyclohexane (C_6H_{12}) [IX.5]. Notice the extremely good energy resolu-

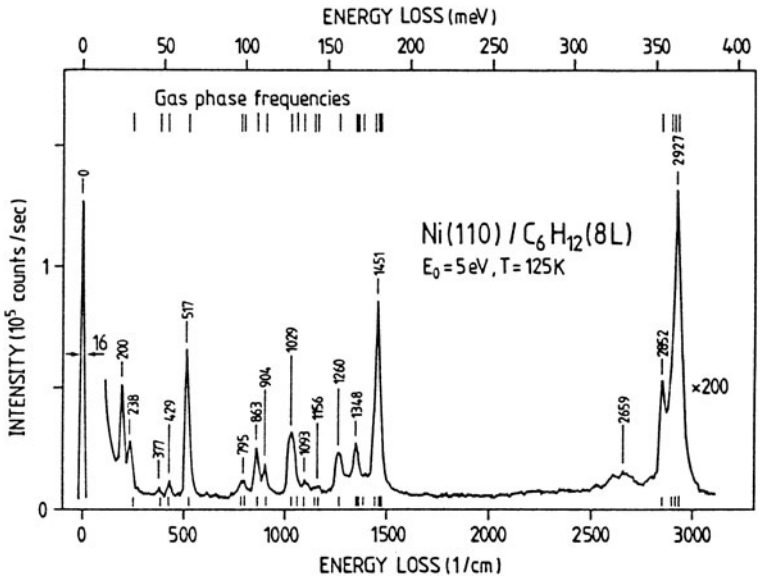

Fig. IX.2 High Resolution Electron Energy Loss Spectrum (HREELS) measured on a Ni(110) surface exposed to 8 L of C_6H_{12}. The measurement was performed with a primary energy of 5 eV under specular reflection geometry and with the sample held at a temperature of 125 K. The vibration frequencies of gas phase C_6H_{12} are given in the upper part of the figure [IX.5]

tion of the electron spectrometer, yielding a FWHM of the primary peak of about 2 meV ($\approx 16\,\mathrm{cm}^{-1}$). Nearly every observed loss peak can be explained in terms of a vibrational mode of the C_6H_{12} molecule. The frequencies of all possible modes of the gaseous C_6H_{12} species are given for comparison in the upper part of the figure. One can infer that the molecule is adsorbed non-dissociatively. There are essentially two loss features which cannot be attributed to intramolecular vibrations, the sharp peak at $200\,\mathrm{cm}^{-1}$ wave number and the broad loss structure near $2659\,\mathrm{cm}^{-1}$. The peak at $200\,\mathrm{cm}^{-1}$ is due to a well-known surface phonon of the Ni(110) surface; this phonon is related to the reconstruction of the Ni surface and carries a dynamic dipole moment normal to the surface, which gives rise to strong dipole scattering [IX.5]. The broad feature near $2659\,\mathrm{cm}^{-1}$ is found for many hydrogen-containing molecules adsorbed on metal surfaces. It is interpreted as due to hydrogen atoms that penetrate into the surface and thus give rise to hydrogen-bonding-type vibrations with respect to the substrate atoms. From the existence of this loss feature, a planar adsorption geometry of the ringtype molecule C_6H_{12}, can be concluded. The hydrogen projecting away from the ring skeleton of the molecule tend to "dig" into the Ni surface. In spite of the planar adsorption geometry, all C_6H_{12} vibrations are observed with relatively high intensity since the low symmetry of the folded ring skeleton of the C_6H_{12} molecule causes dynamic dipole moments with at least one component normal to the metal surface. Nevertheless non-dipolar scattering contributions cannot be excluded in the interpretation of the spectrum.

While HREELS with primary energies typically below 50 eV involves essentially surface scattering (Sect. 4.6), described in terms of the surface loss function $\mathrm{Im}\{-1/(1+\epsilon)\}$ for dielectric scattering, loss spectroscopy with higher primary energies of 100–500 eV (usually termed EELS) reveals loss structures due to both bulk and surface scattering. In dielectric theory both the bulk and the surface loss functions, $\mathrm{Im}\{-1/\epsilon\}$ and $\mathrm{Im}\{-1/(1+\epsilon)\}$, have to be considered for the interpretation of the spectra. The excitations typically observable in the energy loss range $1 \approx 100$ eV are the valence electron plasma excitations (both surface and bulk plasmons) and electronic interband transitions (Fig. IX.1). In this energy range one needs to consider bulk- and surface-state transitions of the clean surface as well as adsorbate characteristic transitions. Thus EELS with primary energies in the 100 eV range has mainly been used to study the electronic structure of clean surfaces (surface states), thin overlayers, and adsorbates. Since an energy resolution of about 0.3–0.5 eV is usually sufficient to reveal the relevant loss structures in the loss range 1–50 eV, the experiments are performed without prior monochromatization using the electron beam of an ordinary electron gun with a thermal width of about 0.3 eV. After scattering from the sample surface, energy analysis is carried out by a hemispherical analyser or a Cylindrical Mirror Analyser (CMA) as often used in AES (Panel II: Chap. 1). The advantage is that standard equipment employed for AES or UPS/XPS can also be used for additional EELS studies. When hemispherical analysers with a well-defined and limited angular acceptance angle are used, EEL spectra in the direct undifferentiated mode usually display enough spectral structure to provide the necessary information. The use of CMAs involves detection of electrons within a wider acceptance angle (cone around CMA axis; Panel II: Chap. 1) and thus leads to the observation of a larger variety of scattering events. The loss spectra are less well resolved, and the double differentiation technique is usually applied to discriminate the major loss structures from the background. As in AES (Panel III: Chap. 2) a small AC signal with frequency ω is superimposed on the voltage between sample and analyser, and lock-in detection is performed at a frequency of 2ω. The negatively recorded $-\mathrm{d}^2I/\mathrm{d}E^2$ spectra show positive peaks exactly where the undifferentiated spectra would show maxima. Minima in the spectra have to be treated with care since they might originate from the double differentiation process. The energy resolution in the double differentiation mode is determined, of course, not only by the thermal width of the primary beam, but also by the peak-to-peak value of the superimposed AC modulation (usually 1 V).

As an example of EELS measured in the undifferentiated mode by means of a hemispherical analyser (Panel II: Chap. 1) Fig. IX.3 exhibits loss spectra for a clean polycrystalline Cu surface and for the same surface after the adsorption of various amounts of CO [IX.6]. The primary peak is not shown for reasons of clarity; the loss features at 4.3 and 7.3 eV for the clean surface are most probably due to d-band transitions which are strongly coupled to surface plasmons [IX.6]. Upon adsorption of CO the spectrum gradually changes; in particular, the 7.3 eV loss is suppressed in intensity and shifts to slightly lower energies. Furthermore, new losses characteristic of the adsorbate occur at 9.4, 11.9 and 13.8 eV, which are fully developed at a CO exposure of 1 L. The losses at 11.9 and 13.8 eV are due to intramolecular

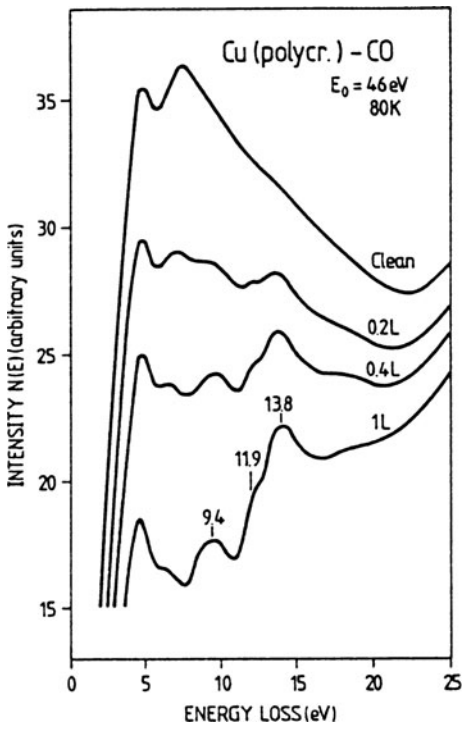

Fig. IX.3 Electron energy loss spectrum of a clean polycrystalline Cu surface and of the same surface after exposure to various amounts of CO at 80 K. The spectra were recorded at room temperature with a primary energy of 46 eV and a hemispherical analyser in the ΔE = const mode (Panel II: Chap. 1); primary peak not shown [IX.6]

Rydberg transitions of the CO molecule, already known from the literature on gaseous CO. Their occurrence thus indicates undissociated, molecular adsorption of the CO. The prominent loss at 9.4 eV could involve some contribution from intramolecular CO $5\sigma \rightarrow 2\pi^*$ transitions which are found in the free molecule at 8.5 eV; but an interpretation in terms of charge transfer transitions from occupied Cu(d) orbitals (substrate) into empty CO($2\pi^*$) adsorbate orbitals seems more likely. The latter interpretation would allow further interesting conclusions about the interaction of the adsorbed molecules with the substrate atoms, particularly since a coverage dependence and surface specifity of this loss has been found [IX.6].

Figure IX.4 presents an example in which double differentiation EELS with a CMA is used to study the electronic properties of a thin overlayer system [IX.7]. When Fe is deposited onto a Si surface, annealing causes a chemical reaction involving Fe–Si interdiffusion and the formation of new compounds, the so-called Fe-silicides. Below about 500°C a metallic silicide FeSi is formed, whereas for annealing temperatures between 550° and 700°C a semiconducting overlayer of β-$FeSi_2$ results [IX.7]. The double differentiated loss spectrum of the clean Si(111)(7 × 7) surface (the primary peak is not shown) exhibits peaks at 2.5, 8, 10.5, 15 and 17.8 eV. According to detailed studies of their origins [IX.8] the peak at 5 eV is due to the E_2 bulk interband transition, whereas the losses at 2, 8 and 15 eV correspond to surface state transitions of the (7 × 7)Si surface. The peaks near 17.8 and 10.5 eV originate from bulk and surface plasmon excitations, respectively. After deposition

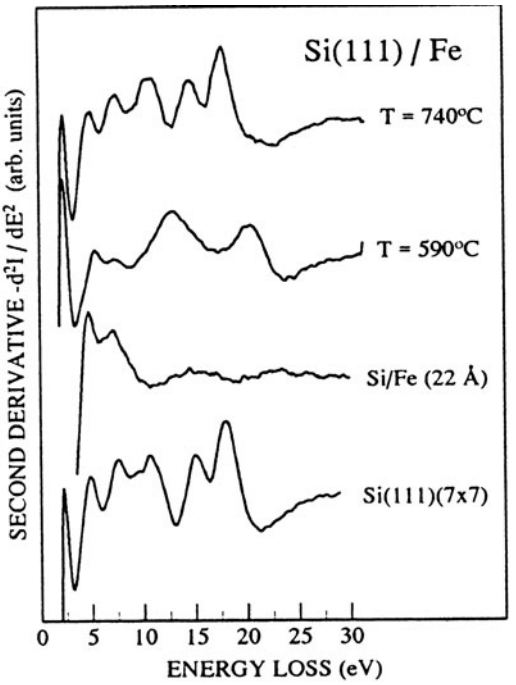

Fig. IX.4 Second-derivative electron-energy loss spectra measured by means of a CMA on a clean Si(111) (7 × 7) surface, after evaporating a 22 Å thick Fe film and annealing the sample to 590 and 740°C. The loss spectra were recorded with a primary energy of 100 eV and an AC peak-to-peak modulation voltage for differentiation of 1 eV; sample surface oriented normal to CMA axis; primary peak not shown [IX.7]

of 22 Å of iron the five new losses near 2.2, 5, 7, 15.5 and 23 eV are attributed to the Fe overlayer: the 23 eV feature arising from the Fe bulk plasmon and the remaining loss peaks from single-electron transitions between occupied and empty *d*-band states of the Fe [IX.9]. After annealing to 590°C a 70 Å thick semiconducting β-$FeSi_2$ layer forms giving rise to characteristic losses at 2.4, 5.5, 7.5, 13.8 and 20.5 eV. The structure at 20.5 eV is most probably due to the valence-band bulk plasmon of $FeSi_2$. The 13.8 eV loss might be a superposition of surface- and interface ($FeSi_2$/Si) plasmon excitations. The remaining peaks are probably due to electronic *d*-band transitions within the $FeSi_2$ overlayer. Their slight shift to higher energies with respect to the corresponding peaks of the Fe overlayer is explained by the bonding shift to higher binding energies of the occupied *d*-orbitals in the $FeSi_2$ compound with respect to free Fe atoms. The topmost spectrum, measured after the last annealing step at 740°C, shows a superposition of the silicide loss features with those typical for the clean Si surface. This demonstrates – in agreement with other experimental findings – that the β-$FeSi_2$ layer disintegrates thus exposing areas of free Si surface.

The two examples above of EELS with unmonochromatized electron beams and a hemispherical analyser or a CMA with double differentiation clearly show the usefulness of this technique for obtaining direct information about the chemical nature and the electronic structure of an adsorbate or a solid heterostructure.

An ever-growing area for the application of EELS is in connection with electron microscopy. The electron beam of a transmission or scanning electron microscope,

in addition to its function in imaging, also induces all the inelastic processes given in Fig. IX.1. An electron analyser incorporated into a transmission electron microscope or into a scanning electron microprobe (Panel V: Chap. 3) allows the analysis of these inelastically scattered electrons. Because of the high primary energies, 100 keV and above, used in both transmission and scanning electron microscopes, magnetic sector analysers are more effective for the energy analysis than the electrostatic analysers used in the low-energy regime (Panel II: Chap. 1). The combination of EELS and electron microscopy is particularly advantageous since it combines all the spectral information from EELS with detailed spatial information. Characteristic excitation spectra can be attributed to particular spots on the sample, typically a thin film. In modern microprobes local analysis can thus be performed on spot sizes down to 10–100 Å. Characteristic core-level excitations, valence-band transitions, and plasmon losses allow the chemical identification, for example, of small embedded clusters or precipitates. Changes in the spectra indicate changes of the electronic structure within these small areas.

Figure IX.5 shows as an example a loss spectrum measured by a scanning electron microscope in transmission on a spot size with a diameter of about 50 Å on a thin Si/Fe/Si sandwich [IX.10]. The high-energy resolution, i.e., the low-energy spread of the primary peak of about 0.3 eV is obtained by the use of a field-emission cathode. A magnetic sector analyser serves as dispersive element for the energy analysis of the transmitted electron beam. Besides the Si bulk plasmon excitations (Si–PL and 2Si–PL as the double excitation), one also sees the Fe $3p_{1/2,3/2)}$ transition and its combination with a plasmon excitation (+PL). At even higher amplification the Si $2p_{1/2,3/2)}$ excitation is also detected at a loss energy of about 100 eV. A clear identification of the material within spots of 10–100 Å diameter is thus possible. Scanning of the beam over different areas of the sample makes a

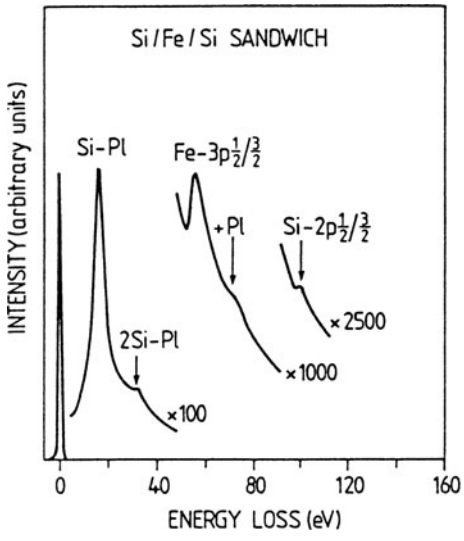

Fig. IX.5 Electron energy loss spectrum recorded by means of a scanning microprobe (VG company) in transmission on an unsupported Si/Fe/Si sandwich; primary energy 100 keV; energy width of primary peak about 0.3 eV [IX.10]

microanalysis possible. The technique is particularly useful when applied in an UHV scanning electron microscope where surface contamination of the sample can be monitored.

References

IX.1 H. Raether: *Excitation of Plasmon and Interband Transitions by Electrons*. Springer Tracts Mod. Phys. Vol. 88 (Springer, Berlin, Heidelberg 1980)
IX.2 H. Ibach, D.L. Mills: *Electron Energy Loss Spectroscopy and Surface Vibrations* (Academic, New York 1982)
IX.3 H. Lüth: Surf. Sci. **168**, 773 (1986)
IX.4 H. Ibach: *Electron Energy Loss Spectrometers*, Springer Ser. Opt. Sci. Vol. 63 (Springer, Berlin, Heidelberg 1991)
IX.5 H. Ibach, M. Balden, D. Bruchmann, S. Lehwald: Surf. Sci. **269/270**, 94 (1992) 1
IX.6 A. Spitzer, H. Lüth: Surface Sci. **102**, 29 (1981)
IX.7 A. Rizzi, H. Moritz, H. Lüth: J. Vac. Sci. Technol. A **9**, 912 (1991)
IX.8 J. E. Rowe, H. Ibach: Phys. Rev. Lett. **31**, 102 (1973)
IX.9 E. Colavita, M. De Creszenzi, L. Papagno, R. Scarmozzino, L.S. Caputi, R. Rosei, E. Tosatti: Phys. Rev. B **25**, 2490 (1982)
IX.10 G. Crecelius (ISI, Research Center Jülich): Priv. commun. (1992)

Problems

Problem 4.1 The N_2O molecule has a linear atomic structure N≡N=0 with σ, π and π^* molecular orbitals. Plot these orbitals qualitatively and discuss by means of symmetry considerations the orientation of the transition dipole moment

$$e \int \psi_f^* z \psi_i d\boldsymbol{r}$$

with respect to the molecular axis z for the $\pi \rightarrow \pi^*$ transitions. ψ_i and ψ_f are the initial- and final-state wave functions, respectively.

Problem 4.2 Benzene (C_6H_6) molecules are adsorbed flat on the Pt(111) surface. Discuss, by symmetry arguments, the orientation of the electronic dipole moment for $\pi \rightarrow \pi^*$ transitions with respect to the surface normal. Are these transitions seen in an EELS measurement (reflection of a 100 eV electron beam)?

Problem 4.3 The clean, annealed Ge(111) surface exhibits a $c(2 \times 8)$ reconstruction. Discuss the corresponding superstructure in real and reciprocal space and plot the expected LEED pattern.

Problem 4.4 The unreconstructed (100) surface of an fcc crystal is covered by irregularly distributed adsorbate islands with an average diameter of 10 Å. The total adsorbate coverage amounts to about 50% of the surface atoms. The islands are formed by atoms, which are bonded on top of the substrate atoms and which exhibit a strong scattering probability in comparison to the substrate.

(a) Discuss the LEED pattern of this surface.
(b) How can one estimate the mean diameter of the islands from experimental data?

Problem 4.5 A GaAs(100) surface is covered by one monolayer of Si atoms. A Rutherford Back Scattering (RBS) experiment is made with 1.4 MeV He^+ ions along the surface normal $\langle 100 \rangle$.

Calculate the energy of the back scattered ions for the Si adsorbate peak and for the Ga and As peaks of the clean GaAs surface.